High Precision sub-kHz Ramsey-Bordé Interferometry on Laser Manipulated Cold
Mg Atoms for an Optical Frequency Standard

1998

To The Memory of My Father

laser cooling, atom interferometer, frequency standard

Abstract

Atom interferometers have proven to have excellent perspectives for many high precision measurements. Especially the Ramsey-Bordé interferometer plays an important role in the study of high precision optical frequency standards and fundamental physics. In combination with the laser cooling and trapping techniques, Ramsey-Bordé interferometry in the time domain on cold trapped atoms offers higher sensitivity and accuracy for optical frequency standards. In this work the time domain Ramsey-Bordé interferometry on cold trapped Mg atoms based on the intercombination transition $^1S_0$-$^3P_1$ at 457 nm has been realized.

In a first step a new second harmonic generation (SHG) setup with BBO as nonlinear crystal was developed to produce the cooling and trapping laser light at 285 nm. The trap dynamics of the Mg magneto-optical trap (MOT) has been studied in detail. The photoionization cross section of the $^1P_1$ state has been measured to be σ_{PI}=(6.3$\pm$1.6)·10^{-17} cm^2 for λ=285 nm. Cold collision phenomena for cold trapped Mg atoms were studied for the first time. The collisional trap loss coefficient β has been determined to be to be smaller than 10^{-12} cm^3/s. The dynamics of a pulsed MOT, necessary for time domain Ramsey-Bordé interferometry, has been studied and an optimization procedure for the Ramsey-Bordé interferometry has been developed.

The theoretical approach for the four zone Ramsey-Bordé interferometry developed by Bordé is revisited to work out the importance of an additional phase term describing the atom-field interaction at the four interaction zones. This additional phase term could be demonstrated in a series of measurements. High resolution Ramsey fringes with line width down to 491 Hz and with a signal-to-noise ratio of 2.3 could be measured on cold, trapped Mg ensembles. This corresponds to a high line Q of 1.3 ·10^{-17}.

To exploit the potential of Mg intercombination line as optical frequency standard, the laser spectrometer for 457 nm is stabilized to a thermal beam Ramsey resonance. The stability of this stabilized spectrometer was measured relative to the atomic resonance achieved on the trapped atoms. The Allan standard deviation has been measured to be 2.7 ·$10^{-13}/\sqrt{\tau}$, which is two orders of magnitude smaller than previous measured values on Mg atoms and is very close to the stability (2.7 ·10^{-13} at 1 s measuring time) of the present best Cs fountain colock.

Laserkühlung, Atominterferometer, Frequenznormal

Zusammenfassung

Atominterferometer haben sich f_r hoch präzise Messungen als gut geeignet erwiesen. Insbesondere das Ramsey-Bordé-Interferometer spielt eine wichtige Rolle sowohl für die physikalischen Grundlagenforschung, als auch für die Realisierung eines präzisen optischen Frequenzstandards. In Kombination mit Techniken der Speichern und Kühlen von Atomen mit Laserlicht ermöglicht die Ramsey-Bordé-Interferometrie im Zeitraum eine hohe Empfindlichkeit und Genauigkeit für optische Frequenzstandards mit kalten Atomen.

In dieser Arbeit wurde die Ramsey-Bordé-Interferometrie im Zeitraum basierend auf dem $^1S_0$-$^3P_1$-Übergang von Mg bei 457 nm mit gefangenen kalten Mg Atomen realisiert. In ersten Untersuchungen wurde eine neue Frequenzverdopplung mit BBO-Kristall als nichtlinearem Kristall aufgebaut, um das Fallen- und Kühllaserlicht bei 285 nm zu erzeugen. Die Dynamik der magnetooptischen Falle wurde detailliert untersucht. Der Photoionisationsquerschnitt des $^1P_1$-Zustands wurde gemessen. Er beträgt $\sigma_{PI} = (6.3 \pm 1.6) \cdot 10^{-17} \, cm^2$. Kalte Stöße von Mg-Atomen wurden erstmals systematisch untersucht. Der Fallenverlustkoeffizient β wurde zu kleiner als $10^{-12} \, cm^3/s$ bestimmt. Die Dynamik der gepulsten Falle, die für die Ramsey-Bordé-Interferometrie im Zeitraum notwendig ist, wurde studiert. Ein Optimierungs-verfahren für die Ramsey-Bordé-Interferometrie konnte entwickelt werden.

Die von Bordé entwickelte Theorie für Vierzonen-Ramsey-Bordé-Interferometrie wurde unter Berücksichtigung einer zusätzlichen Phase, die durch die Wechselwirkung zwischen Atom und Lichtfeld verursacht wird, erweitert. Diese zusätzliche Phase konnte in einer Serie von Messungen nachgewiesen werden.

Höchstauflösenden Ramseyringe mit einer Linienbreite bis zu 491 Hz und mit einem Signal-zu-Rausch-Verhältnis von 2.3 wurden gemessen. Dies entspricht einer hohen Liniengüte Q von $1.3 \cdot 10^{12}$. Um das Potential der Mg-Interkombinationslinie als Frequenzstandard aufzuzeigen, wurde ein 457 nm Laserspektrometer auf das Ramsey-Signal eines thermischen Mg-Atomstrahl frequenzstabilisiert. Die Stabilität des frequenzstabilisierten Spektrometers wurde relative zu der mit Hilfe der Falle bestimmten atomaren Resonanz gemessen. Die Allan-Standardabweichung $\sigma_y(\tau)$ beträgt dabei $2.7 \cdot 10^{-13}/$. Dieser Wert ist um zwei Größenordnungen kleiner als die bisher erzielte Allan-Standardabweichung mit gefangenen kalten Mg-Atomen. Er reicht sehr nahe an die Stabilit□t der bisher besten Cs Atomuhr mit einem Wert von $2 \cdot 10^{-13}$ bei 1 s Messzeit heran.

Contents

Chapter 1

Introduction

Frequency and time are physical quantities which can be measured today with highest precision. An accuracy of about 10^{-13} has been achieved with the commercial Cs beam atomic clocks [Aud 80]. Many other physical quantities can be linked to frequency measurements and there is tremendous effort to connect as many fundamental constants as possible to frequency standards. The length has been defined in terms of time by defining the velocity of light propagation as a constant [Qui 92]. The voltage has been defined in terms of frequency by the Josephson effect [Jos 62]. The Global Positioning System (GPS) with its various applications, as e.g. guiding the movement of transporting vehicles in the next century, depends directly on the precision of atomic clocks. The demand for high precision frequency standards for navigation, radio astronomy, geophysical investigations and telecommunications motivates people to study more stable and accurate frequency standards [Mar 89]. Since the stability is inverse proportional to the line Q, optical frequency standards promise higher stability. The separated oscillatory field methods at microwave frequencies developed by Ramsey can significantly narrow the spectral linewidth [Ram 50]. Baklanov et al. [Bak 76] and Bordé et al. [Bor 82] extended the Ramsey separated oscillatory field towards the optical region for high precision spectroscopy. Bordé found later that the four zone Ramsey geometry with two pairs of counterpropagating traveling waves is actually a Mach-Zehnder type interferometer [Bor 89]. Atoms are coherently splitted by single photon absorption or emission events which leads to an entanglement between the internal states of the atoms and the separated external paths. After the four interaction zones the
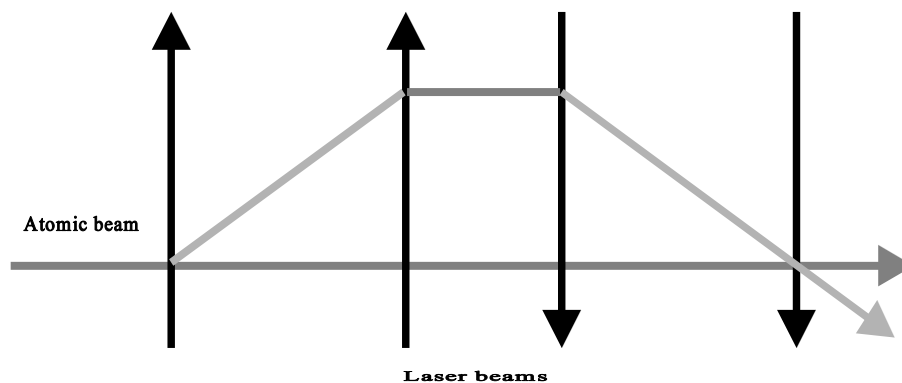

Fig. 1.1: Principle of the Ramsey-Bordé interferometer.

1

atomic waves are recombined to constitute an atom interferometer.

Interferometry has a long history for high precision measurements in physics. Since the 19th century Fizeau (1853), Michelson (1881) and others used optical interferometry to study the problem of light propagation. Today the Michelson interferometer is used for modern gravitational wave detection schemes [Dan 92]. The wave properties of matter were first proposed by de Broglie in 1924. The concept of matter waves was the key concept in the early days of quantum mechanics. It was approved by the diffraction of electrons [Dav 27] and atoms [Est 30]. Matter wave interferometer were first built with electrons [Mar 52] and later with neutrons [Mai 62]. Today many fundamental physical measurements have been studied by electron and neutron interferometers, as e.g. the phase shift caused by rotation and gravitation, the Berry phase, and the Aharonov-Casher effect... [Bad 88].

Atom interferometry opens up much more possibilities because of the internal degrees of freedom of atoms. In addition atom interferometers can be built at moderate cost and dimensions compared to neutron interferometer. The development of atom interferometers came comparatively late due to the lack of appropriate optical elements for a coherent splitting of atomic waves. Today the field of atom interferometry is well established by recent advances in atom optical elements [Ada 94]. These include the mechanical gratings and light fields used for beam splitting. Using micro-fabricated structures Carnal et al. [Car 91] and Keith et al. [Kei 91] have realized the wave-front dividing type of atom interferometer. Atomic and molecular properties such as the electric polarizability, the refractive index of matter waves, fundamental quantum-mechanical issues such as the Heisenberg-microscope and inertial sensing for rotation have been studied with these interferometers [Sch 97, Cla 94, Pfa 94].

Using light field for splitting of atomic matter waves was discussed very early. In 1933 Kapiza and Dirac first suggested to diffract electrons with a nearly resonant standing light wave [Kap 33]. The effect has never been observed due to the weak light-electron interaction. However the strong atom-light interaction allowed for the diffraction of atoms. Under certain conditions the spontaneous emission can be neglected. Atoms absorb and redistribute photons between the counterpropagating light waves, and thus obtain discrete momenta by multiples of $2\hbar k$ along the **k** vectors of the standing light waves. Thus the outgoing atoms appear at discrete angles. This diffraction effect was first demonstrated by the group of Pritchard [Mos 83, Gol 86]. Chebotayev et al. have suggested an interferometer based on such a configuration [Che 85].

Later interferometers with three gratings generated by standing light waves have been realized [Gil 95, Ras 95].

For some experiment such as the detection of Sagnac effect it is desirable to build an interferometer with large area to increase the sensitivity. A large momentum transfer from the beam splitter is essential. To achieve large angle splitting the idea of a blazed phase grating is used. A blazed grating imposes a periodic triangular phase modulation on an incoming atomic wave and results in a diffraction pattern dominated by one specific diffraction order or a narrow distribution of diffraction orders. A variety of proposals and experiments were demonstrated, such as a blazed-grating with a high momentum splitting of $42\hbar k$. [Pfa 93, Gri 94, Joh 95, 96]. By a sequence of multiple Raman π pulses high momentum transfer can also be reached [Wei 94a]. To achieve a large number of π pulses without relevant reduction of the transfer efficiency, population transfer by coherent adiabatic passage was used [Kuk 89]. Many groups have demonstrated this method and realized interferometers based on this mechanism [Gau 88, Mar 91, Wei 94b, Law 94, Gol 94].

Bordé discovered in 1989 that the optical 4 zone Ramsey setup (see Fig.1.1) constitutes an atom interferometer of Mach-Zehnder type. This interpretation led to a completely new view of many historical Ramsey spectroscopy-setup that were actually interferometers [Bak 76, Ber 77, Bar 79, Bab 81, Bor 82,84, Hel 82].

Today various extensions of this type of interferometer were developed. Morinaga realized an interferometer with four copropagating traveling waves [Mor 95]. Because of the symmetry between the two partial beams, the interference signal is independent of the laser frequency. Instead of two partial wave interferometer Morinaga has realized a multiple beam interferometer using up to ten counterpropagating traveling waves [Mor 92]. It was expected that the fringe width becomes narrower as the number of interaction zones increases which is similar to optical interference, but experimentally such effect did not appear. In a similar experiment, recently realized with cold, trapped Mg atoms narrower fringe widths have been observed as the number of zones increases [Rus 98]. Using multiple internal state systems also allowed for multiple beam interferometry [Wei 96, Hin 97].

With the fast development of atomic interferometers in recent years, many precision measurements like the ac and dc polarizability of atoms [Ste 92a, Rie 92, Rie 93, Mor 96], the inertial effect due to rotation and gravitation [Rie 91, Kas 92a], and quantum topological phases

such as the Aharonov-Bohm and -Casher effect [Mül 95, Zei 95] and many other fundamental measurements (see Atom Interferometry [Ber 97]) have been realized.

In this wok the application of four zone traveling wave Ramsey-Bordé interferometer will be used to explore the potential of Mg as optical frequency standard. Through the atom-light interaction the change of the laser frequency will directly reflect on the phase difference of the two partial waves. A high sensitivity of the interference signal on the laser frequency is the result. It is very suitable to act as a frequency discriminator for high precision optical frequency standard. To maintain the coherence of the atomic wave in the interferometer a forbidden transition to a long-living state is necessary. The triplet states of alkali earth elements are good candidates for this purpose. Except beryllium, where little data is available, Mg has the narrowest intercombination transition with a linewidth of 31 Hz [God 92] which corresponds to a line Q of $2 \cdot 10^{13}$. For alkali earth elements there is also a fast singlet transition coupled to the ground state. This fast transition is good for
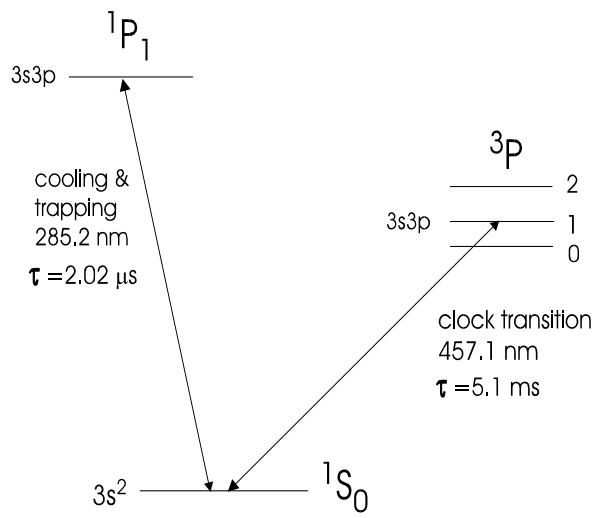

Fig.1.2 Cooling and clock transition of magnesium.

cooling and trapping. For magnesium the cooling transition is closed. All heavier alkali-earth elements have ^{1}D states, which limit the trap lifetime due to optical pumping. With the laser cooling and trapping techniques developed in recent years [JOSA 89, Ari 92] Mg atoms can be cooled to a few mK. At such low temperatures the 1st and 2nd order Doppler effects are significantly reduced. In addition long spectroscopy times can be reached. Using cold trapped atoms high precision spectroscopy with the time domain Ramsey-Bordé interferometry (RBI) is expected.

For high levels of precision the effect of cold collisions may lead to detuning dependent shifts of the transition frequency. Cold collisions have been extensively studied in recent years [Jul 93, Wal 94, Wei 95]. At low temperature the collision phenomenon is different from that at normal temperature since the atomic de Broglie wave length λ_{DB} can be much larger than the scale of the interatomic potential. The collision cross section can be as large as λ_{DB}^2/π. Inelastic collisions can result in trap loss and limit the trap life and the number of trapped atoms. It can

produce sizeable frequency shift in the Cs fountain frequency standard [Gib 93]. On the other hand cold collisions also open new fields for high precision molecular spectroscopy i.e. Photoassociation spectroscopy on cold atoms [Let 95]. This technique can offer useful information for both the excited and ground molecular states. It also plays an important role in the determination of the elastic s-wave scattering length of the ground state of alkali atoms which are the species used to realize the Bose-Einstein condensation [And 95, Dav 95, Bra 95].

In chapter 2 of this work the manipulation of cold Mg atoms will be described. In a magneto-optical trap operated at 285 nm a density as high as $5 \cdot 10^{11}$ atoms/cm^3 of Mg atoms could be reached. At such high densities the collisional trap loss was studied. In addition the possibility of doing photoassociation spectroscopy on cold trapped Mg atoms is discussed. There exists strong interest in achieving the quantum collective regime with alkali earth atoms. For this purpose the s-wave scattering length of the Mg atoms is of special interest. In this frame possibilities to determine the scattering length of ^{24}Mg will be discussed in section 2.4.

The main purpose of present work is to optimize the trap for the high precision RBI experiment. A long term stable trapping laser beam is essential for good signal-to-noise ratio of the spectroscopy. A new method for second harmonic generating the 285 nm cooling and trapping laser beam with a BBO crystal is introduced to improve the experimental conditions. Further optimization of the trap for the interferometry is presented.

The theory of the Ramsey-Bordé interferometry with four traveling wave has been studied by Bordé [Bor 84] in terms of spinors , by Sterr et al. [Ste 92a] with mechanical interpretation and by P. Storey et al. [Sto 94] with the Feynman path integral. The phase difference of the two partial waves introduced in the interaction zone has not been discussed in the literature so far. This phase leads to a different periodicity of the interference fringes compare to the "standard theory". The relevance and dependence of this phase will be discussed in chapter 3. The influence of this phase on the accuracy of frequency standards is discussed.

The experimental setup for RBI on the trap is described in chapter 4. A special detection mechanism with the effect of electron shelving, which was first used in the RBI experiment by K. Sengstock [Sen 94] is revised. Especially, the recapture of the excited $^3P_1$ state is considered here. High resolution Ramsey fringes with line widths of down to 491 Hz is reached. The limit of the present resolution is discussed and further improvements are suggested.

High stability of optical frequency standard is in the center of developments of many laboratories worldwide. Among the many suggested candidates [Hal 89] we show that a high stability for a Mg frequency standard in the order of 10^{-13} for integration times of a few seconds is possible. In chapter 5 the stability of a spectrometer stabilized on the Ramsey fringes of a thermal Mg atomic beam is measured and compared with the Ramsey resonance on the trap. A detailed comparison with other frequency standards will be given. An outlook of future work is described at the end of this work.

Chapter 2

Laser manipulation of cold atoms

Laser cooling of atoms has improved many physical research areas. So far various different, effective cooling methods were developed [Dal 90, Ari 92]. The method of polarization gradient cooling has reached sub-Doppler temperatures [Dal 89, Wei 89, Let89], whereas velocity coherent population trapping (VSCPT) and Raman cooling could even beat the photon recoil limit [Asp 88, Kas 92b]. Due to the $^1S_0$ ground state these schemes are not accessible to the alkali earth elements so far these elements were cooled to Doppler limit temperature. For applications in frequency standard measurements Doppler temperature are sufficient to reduce the second order Doppler effect to values of $\Delta\nu/\nu=10^{-17}$ [Sen 93]. In addition, e.g. quantum topological phases such as the Aharanov-Bohm effect [Mül 95] were measured on laser cooled and trapped atoms. In this chapter the method of manipulation of cold Mg and the optimization of the cold trap for RBI experiment will be described.

2.1 Methods of laser cooling and trapping

The spontaneous force:

The light forces acting on atoms are based on the momentum transfer during the absorption and emission of photons. For stimulated emission in the case of a plane laser wave the emitted photon has the same direction as the absorbed one so there is no momentum transfer and no force acting on the atom. But for the spontaneous emission the emitted and absorbed photon can have a different direction and there is a net momentum transfer to the atom. For a two-level atom the average force due to spontaneous emission can be described by the product of photon momentum $\hbar \cdot k$ and the photon scattering rate [Let 89]:

$$F(v) = \hbar k \frac{\Gamma}{2} \frac{\dfrac{I}{I_{sat}}}{1 + \dfrac{I}{I_{sat}} + (\dfrac{2\Delta - kv}{\Gamma})^2} \qquad (2.1)$$

, where I is the laser intensity, $I_{sat}=\pi hc/3\lambda^3\tau$ is the saturation intensity, Γ is the line width of

the cooling transition, Δ is the laser detuning and v is the velocity of the atom.

This force saturates to $\hbar k\Gamma/2$ for high laser intensity. At such an intensity the spontaneous force corresponds to an acceleration of $a=1.4\cdot10^7$ m/s^2 for a Mg atom. The spontaneous force can decelerate or accelerate the atoms depending on the laser detuning from the atomic resonance frequency. For a red detuned laser, counterpropagating to an atomic beam the atoms are decelerated. But after some photon scattering the atom will be decelerated out of resonance and further deceleration stops. Two method are used to solve this problem. One method is the so called chirp cooling where the frequency of the cooling laser is varied in time such that it is always resonant with the cooled atoms [Ert 85]. This method is suitable for preparing pulsed cold ensembles. In the other method, called Zeeman cooling, the atomic transition energy is modified to guarantee the resonance condition by the Zeeman effect [Pro 85]. In the experiments described in this work the Zeeman detunig method is used to decelerate Mg atoms. For atoms always resonant with the cooling laser beam the condition $\Delta=-kv(z)+\mu B(z)$ must be fulfilled. This requires specific magnetic field gradient to efficiently cool the atomic beam. The details of the magnetic field design for the deceleration of the atoms is described in [Hen 92].

Cooling in optical molasses:

Within a setup of three pairs of counter-propagating red detuned laser beams the velocity of atoms is reduced in all three dimensions, the atoms are cooled [Hän 75] . S. Chu first demonstrated this method and called the cooled cloud optical molasses [Chu 85]. When the intensity is small the multiphoton scattering effect can be neglected and the total force of each pair of laser beams can be described as the sum of the spontaneous forces from each laser beam. This cooling force can be written as $f(v)=-\alpha_v\cdot v$ for small velocity, where α_v is the friction coefficient and is given by
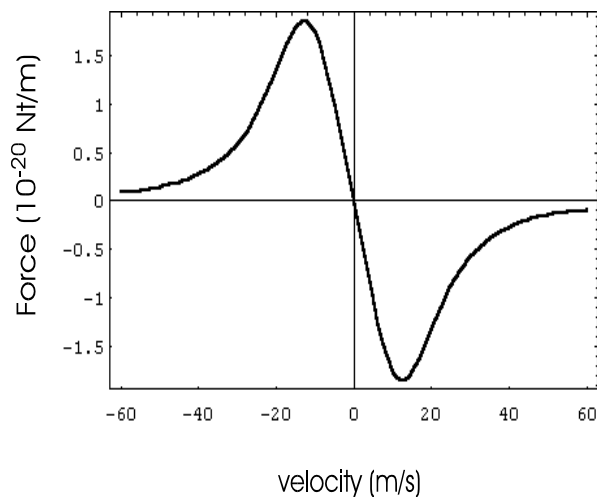

Fig. 2.1: Average force acting on a Mg atom with two counterpropagating $-\Gamma/2$ detuned laser beams.

$$\alpha_v = 4\hbar k^2 \frac{I_s}{I_{sat}} \frac{\frac{2\Delta}{\Gamma}}{[1 + 2N\frac{I_s}{I_{sat}} + (\frac{2\Delta}{\Gamma})^2]^2} \tag{2.2}$$

Here I_s is the intensity of each laser beam and N is the dimension. This averaged force is shown in Fig. 2.1 for Mg atoms with $\Delta = -\Gamma/2$ and for $I_s = 0.25$ mW/mm^2.

Besides the cooling effect additional heating effect appears, which is resulted from the random processes of spontaneous emission. According to the random walk theory the momentum diffusion rate is described by [Let 89]

$$\frac{d\langle p^2 \rangle}{dt} = \hbar^2 k^2 \frac{\Gamma}{2} \frac{2N\frac{I_s}{I_{sat}}}{1 + 2N\frac{I_s}{I_{sat}} + (\frac{2\Delta}{\Gamma})^2} \tag{2.3}$$

The heating rate $\langle \dot{p}^2 \rangle / 2m$ equilibrate the cooling rate $\alpha_v v^2$ and results in an equilibrium temperature:

$$k_B T = \frac{\hbar \Gamma}{4} \frac{1 + 2N\frac{I}{I_s} + (2\Delta/\Gamma)^2}{2|\Delta|/\Gamma} \tag{2.4}$$

This temperature has a minimum value when $\Delta = -\Gamma/2$ and satisfies $k_B T_D = \hbar \cdot \Gamma/2$. This temperature limit T_D is the so called Doppler-cooling limit.

.

Trapping in a MOT

The optical Earnshaw theory [Ask 83] prevents a stable trapping of two level atoms only using the spontaneous force. A method to overcome the optical Earnshaw theory was first demonstrated by Raab et al. and is called magneto-optical trap (MOT) [Raa 87]. The setup is based on the spatial dependent Zeeman effect to produce a spatial dependent scattering force. In

9

the MOT, three pairs of counter-propagating σ⁺σ⁻ laser beams are red detuned and crossed at the center of two coils in anti-Helmholtz configuration. These anti-Helmholtz coils produce a magnet field $B_z(z)=bz$, where b is a constant. The corresponding Zeeman shift for a $^1S_0$-$^1P_1$ transition is shown in Fig. 2.2. If the atom is at a position with z>0 it will scatter more photons from the σ⁻ beam since it is shifted more on resonance with the σ⁻ beam and experiences a negative force. For z<0 the situation is reversed and the force is reversed.
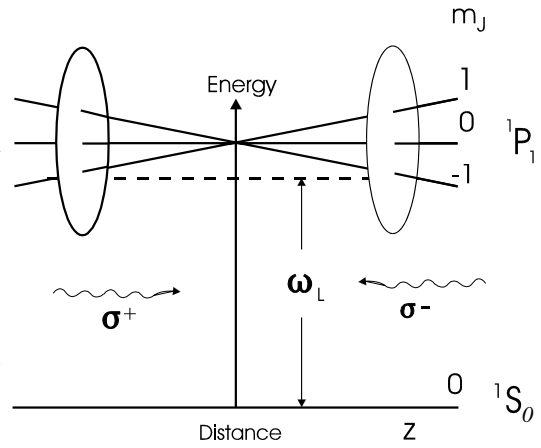

Fig. 2.2: Energy-level of Mg atom immersed in a magnetic field $B_z(z)=bz$.

So the atoms always experience an averaged restoring force. This position dependent restoring force can be described by $F_{sp}(x)=-\kappa x$, with

$$\kappa = 4\hbar k \frac{I_s}{I_{sat}} \frac{\frac{2\Delta}{\Gamma}}{[1+\frac{2NI_s}{I_{sat}}+(\frac{2\Delta}{\Gamma})^2]^2} \frac{\mu_B}{\hbar} \frac{dB}{dx}$$ (2.5)

where μ_B is the Bohr magneton.

The total force acting on the atom is given by $F(x)=-\alpha_v v - \kappa x$ which leads to the equation of motion given by

$$\ddot{x}+\gamma\dot{x}+\omega^2 x=0$$ (2.6)

with $\gamma=\alpha_v/M$, $\omega^2=\kappa/M$, and M the mass of the atom.

This is just the motion of a damped harmonic oscillator with a oscillation frequency ω. The ratio $\gamma^2/4\omega^2$ determines the character of the motion of the trapped atom. If this ratio is larger than one, the motion is overdamped. At a typical magnetic field gradient of 65 G/cm in the radial direction and $\Delta=-\Gamma/2$ we have $\alpha_v>4.8\ 10^{-22}$ Nt·s/m and $\omega>5.3\cdot10^3\ s^{-1}$ for typical trap intensity $I_s/I_{sat}>0.01$. The ratio $\gamma^2/4\omega^2$ is larger than 1.2 so the motion is overdamped. The relaxation to the origin is governed by the time constant $\gamma/\omega^2=385$ µs which depends only on the magnetic

field gradient and not on intensity and detuning.

When the random scattering process of photons is considered the motion is modified and can be described by a Fokker-Plank equation [Ste 86]

$$\frac{\partial P}{\partial t} + v \frac{\partial P}{\partial z} = \frac{\partial}{\partial v} [\frac{\gamma v}{M} P + D \frac{\partial P}{\partial v}] \tag{2.7}$$

The function P(z,v,t) describes the probability distribution of atoms in the phase space of position and velocity. This leads to a Gaussian distribution of phase space density.

$$\rho(x,v) = \frac{N_0}{2\pi\sigma_x\sigma_v} \; e^{-(\frac{v^2}{2\sigma_v^2} + \frac{x^2}{2\sigma_x^2})} \tag{2.8}$$

where $\sigma_v^2 = k_B \cdot T/m$ and $\sigma_x^2 = k_B \cdot T/m\omega^2$.

Today the MOT is the standard method of creating large atomic ensembles of cold atoms. In the following the experimental setup of a MOT for the Mg atoms will be described.

2.2 Experimental setup

2.2.1 The laser systems and frequency stabilization

The laser systems for the cooling and trapping contain two similar home built ring dye lasers , in combination with two external cavities for second harmonic generation (SHG) with BBO crystals. The ring dye lasers are first frequency stabilized to respective reference resonators with the side-fringe locking technique. The laser frequency can be varied by rotating the Brewster plate inside the resonator. Due to a residual frequency drift further stabilization techniques [Loc 92, Zel 93] are used to improve the long term stability. The trapping laser is further stabilized at the u-line of the R115(20-1) transition of $^{127}I_2$ molecule by the polarization spectroscopy method. The schematic setup is shown in Fig. 2.3. The frequency offset between the Mg $^1S_0$- $^1P_1$ transition and the u-line ca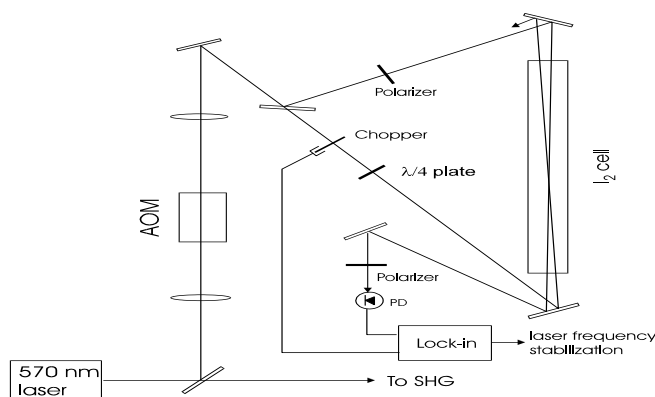n be compensated by a frequency variable AOM. For the trapping of ^{24}Mg atoms the modulation frequency of the AOM is usually operated in the region of 96 MHZ.

Fig. 2.3: Schematic Diagram of the frequency stabilization of the trapping laser with Polarization spectroscopy.

The second laser is frequency stabilized to a transfer resonator whose length is locked to a He-Ne laser with lock-in method as shown in Fig. 2.4. The He-Ne laser is frequency stabilized with polarization technique [Ste 87]. Instead of a direct locking of the dye laser to the resonator its frequency is first modulated with an EOM. The side band of the modulated laser beam is then stabilized to the transfer resonator. The frequency of the dye laser can be varied by varying the modulation frequency of the EOM. A HF-generator with a frequency tuning range between 0.3 GHz and 2.7 GHz produces the modulation frequency for
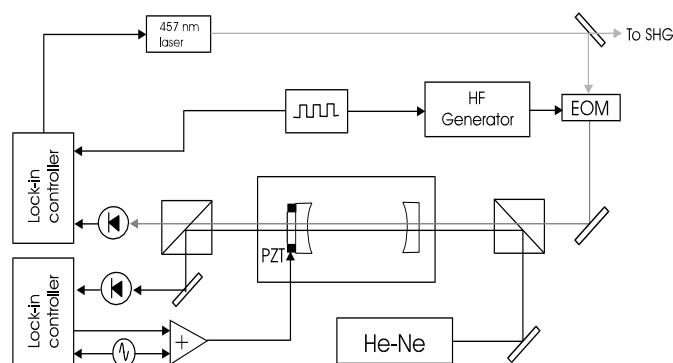

Fig. 2.4: Frequency stabilization of the cooling laser with lock-in technique.

the EOM. This frequency range is larger than the FSR (1.5 GHz) of the transfer resonator. Therefore, the laser can then be stabilized to any desired frequency.

The beat signal of the two frequency stabilized laser is about 2 MHZ. The linewidth of each laser is smaller than this value. The output power of the dye lasers is usually 1 ~1.4 W. Both lasers are frequency doubled with a nonlinear BBO crystal as described in the next section.

2.2.2 Second harmonic generation (SHG)

The principle of SHG is based on the nonlinear dependence of the dielectric polarization **p** on the electric field **E**. It is related to the field **E** by the equation:

$$P(E) = \chi \cdot E + \chi^{(2)} \cdot E^2 + \chi^{(3)} \cdot E^3 + ... \qquad (2.9)$$

where $\chi^{(n)}$ is the nonlinear susceptibility coefficient and is a tensor of rank n. The relevant term for SHG is the term $\chi^{(2)}$. A propagating monochromatic wave of frequency ω leads to a new light wave of doubled frequency. Besides energy the momentum is also conserved i.e. $2k^\omega = k^{2\omega}$, where we have assumed all photons have the same direction. From the relation $k = 2\pi/(\lambda/n)$ it also means that the refraction index must satisfy $n^\omega = n^{2\omega}$. This condition is called phase matching. Since for normal material $n^\omega < n^{2\omega}$. This condition can be fulfilled only in nonlinear crystal in which the phase velocity of an optical beam depends on the direction of polarization of its **E** vector.

The phase matching can be more easily understood in view of the index surface in which the distance of a given point from the origin is equal to the index refraction of a wave propagating along this direction. The refraction index n_o of the fundamental (ordinary) wave is independent of the propagation direction and it is represented by a ball with radius of n_o. On the other hand the refraction index of the second harmonic
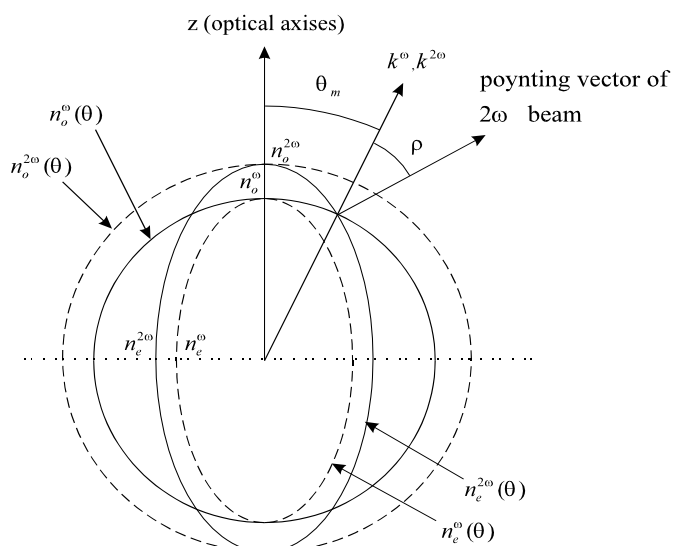

Fig. 2.5: Intersection of k-z plane with index surfaces of a negative uniaxial crystal.

13

(extraordinary) wave depends on the propagation and it is represented by an ellipsoid with major axis n_o (n_e) and minor axis n_e (n_o) for a negative (positive) uniaxial crystal. The cross section of such index surfaces for a negative ($n_e < n_o$) uniaxial crystal is shown in Fig. 2.5. The cross point at $n_e^{2\omega}(\theta) = n_o^{\omega}$ satisfies the phase matching condition, where θ is the angle between the optical axis **z** of the crystal and the propagation wave vector **k** .

There are two methods to realize the phase matching for SHG which are critical phase matching and noncritical phase matching. The phase matching angle θ is 90^0 for critical phase matching. This is usually achieved by changing the crystal temperature such that $n_e^{2\omega}(90°) = n_o^{\omega}$. This is also the method which was used for the experiments with Mg atoms before this work. An ADA crystal was cooled to $-33°C$ to get the 285 nm radiation. To get enough power this was realized in an external cavity to enhance the conversion efficiency and usually 10~20 mW of the 285 nm light were available. The drawback was that maximum enhancement could be achieved for about half an hour and then dropped down to nearly half the value due to damage in the crystal. Another inconvenience was that the temperature must often be readjusted to meet the optimum value.

In the work described here a beta-barium borate (BBO) crystal was used to improve the experimental conditions. Part of the setup is also described in the diploma thesis of D. Scheller [Sch 96b]. BBO is a negative uniaxial nonlinear crystal. The refraction index is not very sensitive to temperature (dn/dT≈-1·10⁻⁵ 1/K) . It can't be temperature tuned to get the required wavelength so the noncritical phase matching is used. Phase matching can be achieved by adjusting the phase matching angle θ_m (see Fig.2.5) such that it satisfies the following equation

$$\sin^2\theta_m = \frac{(n_o^{\omega})^{-2} - (n_o^{2\omega})^{-2}}{(n_e^{2\omega})^{-2} - (n_o^{2\omega})^{-2}} \qquad (2.10)$$

The formula for refraction index of BBO can be found in [Dmi 91]. This phase matching angle for the 285 nm SHG is 43.2^0 according the above equation.

When a plane wave propagates in an uniaxial crystal, the direction of the propagation wave vector **k** generally does not coincide with that of the poynting vector. The direction of the poynting vector can be defined as the normal to the tangent drown at the point of the intersection of the vector **k** with the n(θ) curve. It is seen from Fig. 2.5. that for the ordinary beam the poynting vector has the same direction as the **k** vector but they are different for the extra-ordinary beam.

The angle between the poynting vector and the **k** vector is called walk-off angle and is given by [She 84]

$$\rho = \arctan\left(\frac{(n_o^\omega)^2}{2}\left(\frac{1}{(n_e^{2\omega})^2} - \frac{1}{(n_o^{2\omega})^2}\right)\sin(2\theta_m)\right)$$

(2.11)

This angle is $4.8°$ for the second harmonic wave at 285 nm. This walk-off reduces the efficiency of SHG as will be seen below.

For a focused Gaussian beam Boyd & Kleinmann has shown that the power of the extraordinary wave can be described by [Boy 68]

$$P_2 = \frac{2\omega^2 d_{eff}^2}{\pi\epsilon_0 c^3 n_e^{2\omega}(n_o^\omega)^2}P_1^2 l k_1 e^{-(\alpha_1 + \frac{1}{2}\alpha_2)l}h(\sigma,B,\kappa,\xi,\mu)$$

$$= \eta\, P_1^2$$

(2.12)

where d_{eff} is the effective non-linear coefficient that is (1.73 ± 0.07) pm/V in our case, l is the length of the crystal, α_1, α_2 the absorption coefficient of the ordinary and extraordinary wave, η the conversion coefficient. The focusing factor h depends on the following parameters

$$\sigma = \frac{1}{2}b\Delta k \qquad phase\ matching$$

$$B = \frac{\rho\sqrt{lk_1}}{2} \qquad walk\text{-}off$$

$$\kappa = \frac{1}{2}(\alpha_1 - \frac{1}{2}\alpha_2)b \quad absorption$$

$$\xi = \frac{l}{b} \qquad focus\ parameter$$

$$\mu = \frac{l-2f}{l} \qquad position\ of\ focus$$

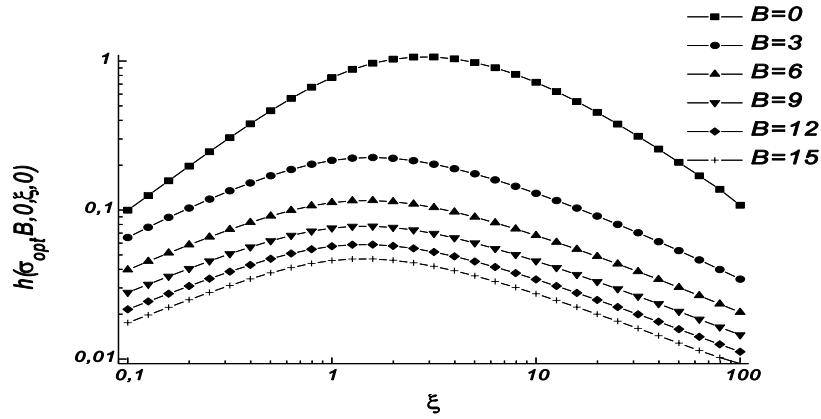$$b = w_0^2 k_1 \qquad confocal\ parameter$$

$$w_0 \qquad laser\ beam\ waist$$

(2.13)

Fig.2.6: The focusing factor $h(\sigma_{opt},B,0,\xi,0)$ as a function of the focus parameter ξ for various walk-off parameters B.

Fig. 2.6 shows $h(\sigma_{opt},B,0,\xi,0)$ as a function of the focus parameter ξ for various walk-off parameter B, where the absorption is neglected ($\kappa=0$) and the focus is assumed at the middle of the crystal ($\mu=0$). The value of σ has been optimized for each $h(\sigma_{opt},B,0,\xi,0)$. For a 7mm long BBO crystal B=15 and the optimum parameter for optimum h value is

$\sigma_{opt}=0.75$

$\xi_{opt}=1.43$

$h(\sigma_{opt},B=15,\kappa=0,\xi_{opt},\mu=0)=4.7\cdot 10^{-2}$

In the experiment the optimum value of σ_{opt} is reached by tunning the phase matching angle to match the optimum SHG power. From the value ξ_{opt} the optimum laser waist is calculated to be 16 µm. For the above parameters the theoretically predicted conversion coefficient η is $1.1\cdot10^{-4}$ W^{-1}. We have measured P_2 as a function of P_1 for single pass conditions to determine the value η. The experimentally measured value for η is $(5.5\pm1)\cdot10^{-5}$ W^{-1}. This value is only half of that theoretically predicted. A reason for this is probably that the actual crystal has a smaller non-linear coefficient.

Equation 2.12 shows that the extra-ordinary wave power is proportional to P_1^2. To enhance the ordinary wave power the SHG is realized in an external cavity. When the cavity is in resonance with the input wave the enhancement A of the input power in the cavity is given by [Bor 69]

$$A = \frac{P_c}{p_1} = \frac{T_1}{(1-\sqrt{(1-T_1)(1-V)})^2} \tag{2.14}$$

where P_c is the power of ordinary wave in the cavity, T_1 is the transmission of the input coupler and V is the loss in the cavity. There is an optimum enhancement for T_1=V, i.e. A_{max}=1/T_1 . In this experiment the transmission of the input coupler is 2.1%. To reach the optimum focus as mentioned before two focused mirrors M2 and M3 with radius 30 mm are used as shown in Fig. 2.7. The cavity has a total length of 24cm . Such a small cavity has a large cavity linewidth of 12.5MHz which is much larger than the linewidth of the laser (2<MHz). This also means that the
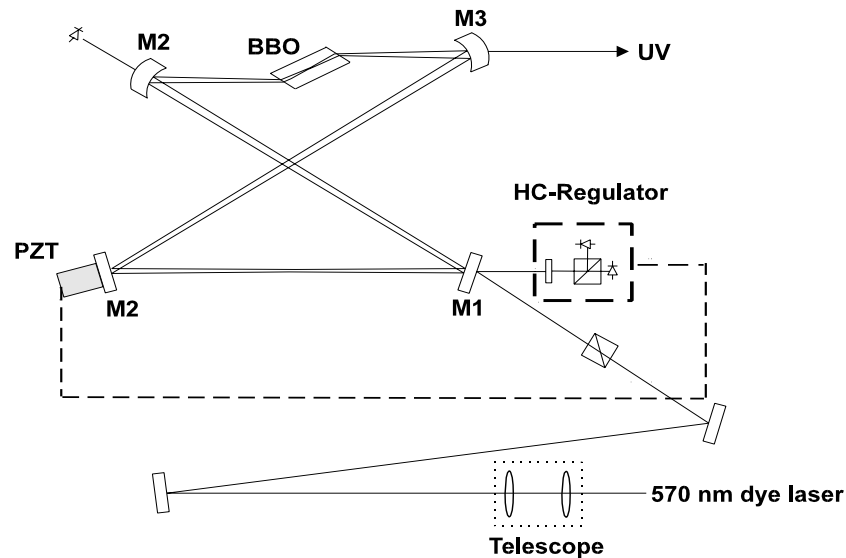
Fig. 2.7: SHG with an external cavity. The cavity is locked in resonance with the input laser through Hänsch-Couillaud method.

cavity lock loop will be more stable since the trap range is larger when compared to a long cavity with short cavity linewidth. The lock of the cavity mode to the incoming beam is realized by a Hänsch-Couillaud method [Hän 80].

The generated extra-ordinary wave power with cavity enhancement is given by P_2=$A^2\eta P_1^2$. Fig. 2.8. shows the generated second harmonic power as a function of the power of the ordinary wave. Here P_2

Fig. 2.8: The generated UV-power as a function of the input power of the fundamental wave. The solid line is a quadratic fit to the measured data.

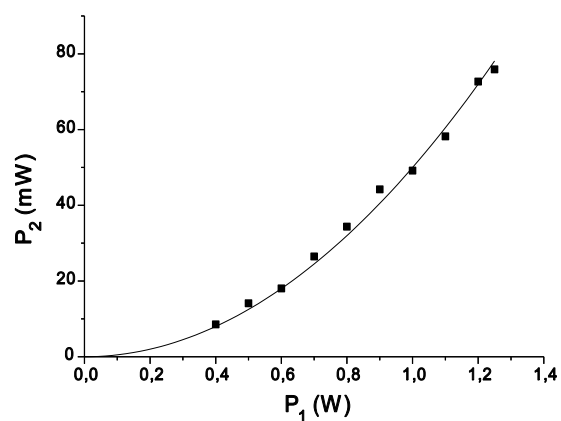describes the second harmonic power generated inside the crystal. The outcoupled power is 77% of that value since the Fresnel-reflection at the crystal surface has to be considered. The cavity enhancement is about 30 and can endure some hours without remarkable degradation. Comparing to ADA-crystal a large improvement has been reached.

The generated extraordinary UV-wave is extremely elliptical. Because the walk-off effect the size of the extra-ordinary beam will be larger in the near field. Similar to diode laser this results in a smaller far field beam size in the phase matching angle direction. The ellipticity can be compensated with cylindrical lenses as shown in Fig. 2.9. To achieve a symmetric beam profile the ratio of the focal length of the two lenses should be approximately the same ratio of the beam divergence. The lenses are placed at a distance equal to their respective focal length from the crystal. The lenses have a focal length of f_1=10.5 cm and f_2=100 cm respectively which matches the ratio of the beam divergence. The compensated beam can then be manipulated with spherical lenses to get the desired beam size. The right picture in Fig. 2.9 shows such a compensated symmetric beam profile measured by a UV-CCD-camera.
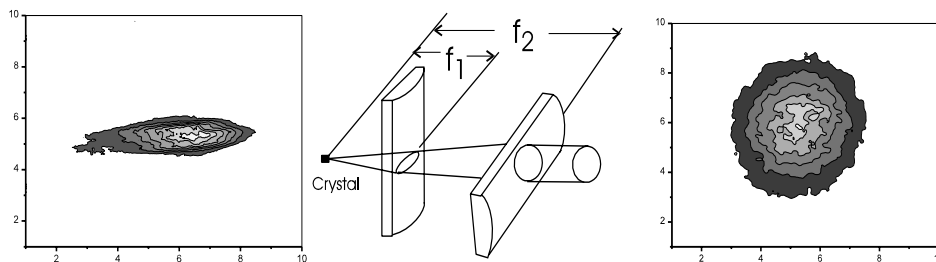
Fig. 2.9: Compensation of the ellipticity of the generated extraordinary UV-wave.

2.2.3 The stabilization and the optical setup

In our system the 570 nm laser and the SHG are at a different table as the trap. The laser beam is position stabilized to reduce position fluctuation due to the different tables. A four-quadrant photodiode (QP) together with a mirror mounted on bending PZTs (PM) composites a stabilization unit (see Fig. 2.10). The error signal detected from the 4-quadrant photodiode is amplified by a PI-regulator and used to control the PZT-mounted mirror to actively stabilize the beam position. Two units are needed to stabilize a laser beam [Str 94]. In order to isolate the coupling between the two stabilization units the position of the first 4-quadrant photodiode QP1 is imaged on to the surface of the second PZT-mirror through a lense.

Fig.2.10: Laser beam position stabilization and intensity stabilization.
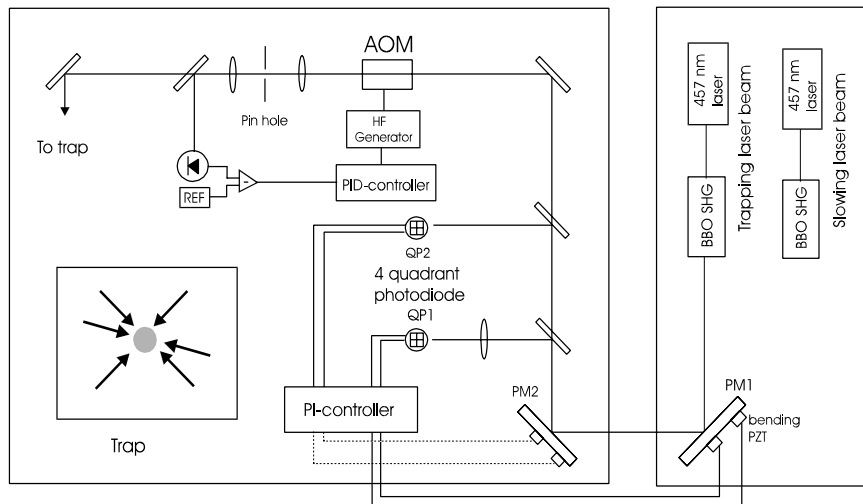
The laser beam profile is measured with a shaver knife scanning across the laser beam (see Fig.2.11). The power of the laser beam behind the knife is measured with a photodiode. The

measured power as function of the position of the knife is shown in Fig.2.12. From the curve the beam size can also be derived. The trapping laser beam has a $1/e^2$ radius of 2.9 mm.

Fig.2.11: Setup for the measurement of the beam position stability.

To measure the beam position fluctuation half of the laser beam is covered by the knife. As shown in Fig 2.12.a the slope at this position is maximum which also means the position sensitivity is maximum. The measured power fluctuation behind the knife

corresponds to the fluctuations of the beam position. In order to get rid of the power fluctuation from the source, the measured power is devided by a reference power which is independently measured with another photodiode. The devided signal is recorded by a computer. The measured power fluctuation is shown in Fig. 2.12.b. According to the slope in Fig. 2.12.a the power fluctuation corresponds to a beam position fluctuation of ±3.4 µm (one standard deviation σ).

19

Fig. 2.12: a.) Measured intensity as a function of the position of the scanning knife. b.)Measured intensity fluctuation when the knife is placed at middle of the laser beam

To get a stable trap fluorescence the intensity stability is also important. The laser beam intensity is controlled by an AOM (see Fig. 2.10). A pinhole after the AOM leads to a high quality Gaussian beam, where 80% of the power can be transmitted. A high sensitive photodiode (0.133A/W) detects the intensity behind the pinhole such that the intensity fluctuation due to residual position fluctuatio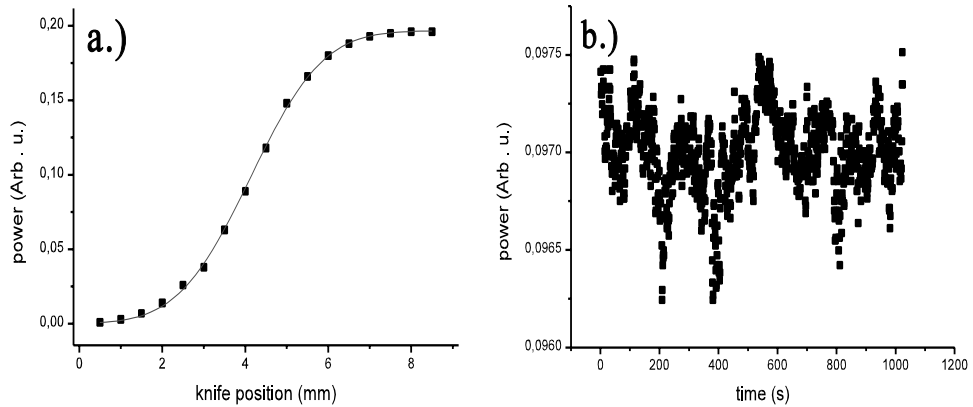ns behind the pinhole can also be compensated. The error signal is obtained from the difference of the detected signal voltage and a reference voltage from a LM399 (temperature coefficient 5 ppm/^{0}C). A PID-controller controls the HF-generator which regulates the laser intensity from the AOM in the -1st order. Fig. 2.13 shows the residual intensity fluctuations measured with a photodiode. The intensity fluctuation is ±3.3% (one σ). This intensity fluctuation is directly reflected on the fluorescence of the trap. With longer integration time in detecting the fluorescence this noise can be reduced. Section 2.5 shows that the noise of the fluorescence can be smaller than 1% after 1 s integration time. The slowing laser beam is similar to the trapping laser beam except that no beam position stabilization and pinhole is used. The residual intensity fluctuation of the slowing laser is ±2.8%.
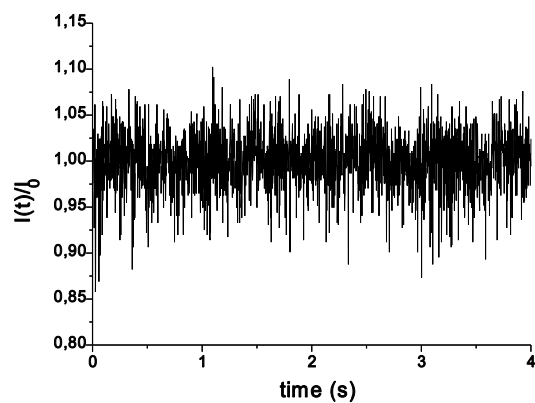

Fig.2.13: Residue intensity fluctuation after the intensity stabilization.

20

The trap and imaging optics

After the stabilization mentioned above the laser beam is splitted into three independent trapping beams. Each trapping laser beam is retroreflected and a λ/4 plate is inserted in each laser beam to produce the standard MOT configuration. A condenser-lense above the trap can collect 4% of the fluorescence from the trap. To determine the spatial distribution of the trapped atoms about 50 % of the fluorescence is detected by a multi-channel plate enhanced CCD-camera. The other 50% of fluorescence is reflected towards a sensitive photodiode (EG&G UV-100BG) through a HR-mirror (see Fig. 2.14). From the photodiode signal the number of trapped atoms can be easily determined. The residual fluorescence transmitted through the HR-mirror is then detected by a photomultiplier tube (PMT). The transmitted fluorescence is sufficient for the PMT so that an iris
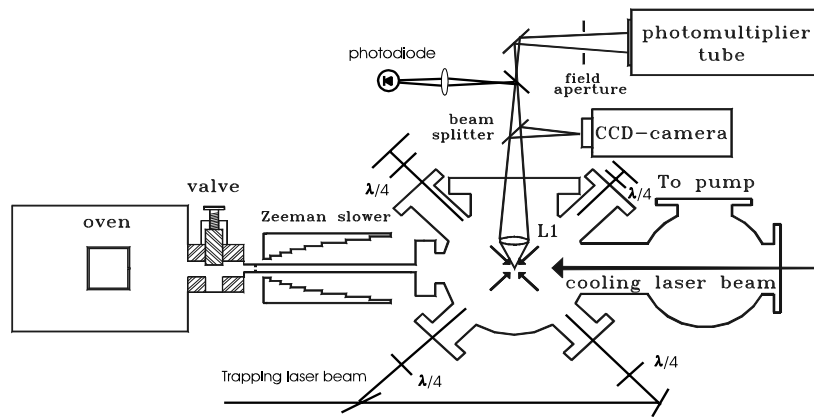
Fig. 2.14: Experimental setup for the cooling and trapping. The horizontal trapping laser beam is not shown.

diaphragm is used to control the height of the overall signal. An anti-Helmholtz coil produces a magnetic-field gradient of 2.6 G/cmA in the axial direction. Three pairs of Helmholtz coils are used to compensate the stray magnetic field of the slowing-Zeeman-magnet. The atomic source has an aperture with diameter of 1mm and is collimated by a circular collimator (with the same diameter) 15 cm downstream. This produces an atomic beam with intensity given by I_b $=(1/f)\cdot(v_p A_s A_c n_0/2\pi\sqrt{\pi}\, l^2)$, where $v_p = \sqrt{2k_B T/m}$ is the most probable velocity of the atoms in the oven (695 m/s at 700K), A_s and A_c is the area of the oven aperture and the collimator, respectively, n_o is the atomic density in the oven ($8.0\cdot10^{13}$ cm^{-3} at 700 K [Smi 54]), l is the distance between oven aperture and collimator, and 1/f is a factor which takes into account the

21

effect of aperture thickness and is about 0.7 in our case [Ram 56]. At an oven temperature of 700 K the atomic beam can provide an atomic intensity of $9.5 \cdot 10^{10}$ atom/s. This atomic beam expands to a radius of 2.6 mm at the trap center. The total setup is shown in Fig. 2.14.

2.3 Results of the cooling and trapping experiments

2.3.1 Characteristics of the trap

For a careful alignment of the optics and the stabilization described before the Mg trap runs stable and continuously. The quadruple magnetic field has a typical field gradient of 130 G/cm in the axial direction. During this work the magnetic field gradient was fixed at that value for most of the experiment. Atoms can be directly trapped from the thermal atomic beam or from the laser decelerated atomic beam. The number of trapped atoms is determined by the photodiode signal. This photodiode has been calibrated with the help of a power meter calibrated by NIST. The measured sensitivity of the photodiode is the same as that delivered by the manufacturer i.e. 0.133 A/W. Fig. 2.15 shows the number of trapped atoms captured from the laser decelerated atomic beam for different trap laser intensity. In the maximum $5.2 \cdot 10^6$ atoms can be trapped from the slow atomic beam. This is an order of magnitude larger than in previous experiments [Bet 95]

Fig. 2.15: The number of trapped atoms as function of the trap intensity of each beam.
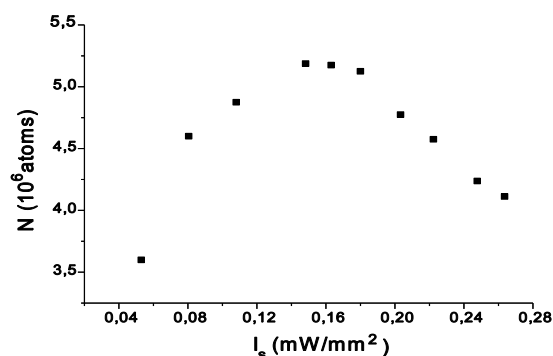
since we have a larger atomic beam flux and a larger trapping laser beam. The number of atoms trapped from the slow tail of the thermal atomic beam is a factor of about 200 smaller than that trapped from slow atomic beam. For an intensity larger than about 0.16 mW/mm^2 the number of trapped atoms deceases. This is due to the intensity dependent trap loss mechanism coming from photoionization which will be discussed in the next section. The spatial distribution of the trapped atoms is detected by the CCD-camera. The radius of the trap is generally different in the axial and radial direction of the quadruple magnetic field. They are sensitive to the alignment of the trapping laser beams. In the usual condition the ratio of radius in the axial (w_A) and radial direction (w_R) is measured to be $w_R \approx 1.2 w_A$. The calibration of the diameter with a CCD-camera leads to a great uncertainty. Thus we have measured the temperature and the spring constant of the trap to derive the absolute trap radius.

Measuring the spring constant

The spring constant is related to the trap position damping time by $\tau_{pos} = \alpha / \kappa$ as described in section 2.1. This trap position damping time is determined by measuring the recapture time

constant when the trap is driven away from its equilibrium position by another laser pulse. To measure this time half of the fluorescence signal is covered. Then, another laser pulse which is frequency detuned about 4Γ to the red side of the resonance is used to push the trap some diameter distance away from its original position such that the fluorescence is reduced to zero. Fig. 2.16 shows the reappearance of the fluorescence after the additional laser pulse. The large background
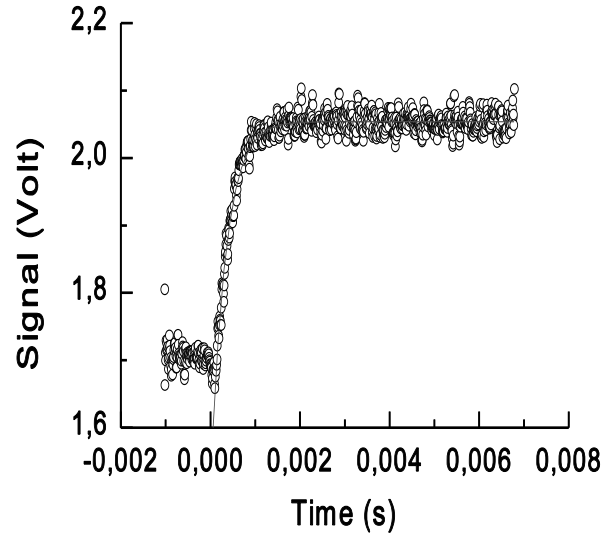

Fig. 2.16: The evolution of the trap fluorescence after it is shifted away from its original position.

signal is mainly due to the offset of the operational amplifier of the photodiode. The time constant determined by the exponential fit is 340 µs. For a trapping intensity of $I_s=(0.17\pm.02)$ mW/mm^2 and a laser detuning of -(47±2) MHz the theoretically calculated α is $\alpha= (1.34\cdot10^{-21}\pm0.34)$ Nt·s/m. The spring constant is determined to be $(3.9\pm1.0)\cdot10^{-18}$ Nt/m. This is consistent with the theoretically calculated value $(3.5 \pm 0.9)\cdot10^{-18}$ Nt/m according to eq. 2.5. From the equipartition theorem

$$\frac{1}{2}k_B T = \frac{1}{2}\kappa r^2 \qquad (2.15)$$

where T is the temperature of the trap and r is $1/\sqrt{e}$ radius of the trap.

With the velocity (0.94±0.08 m/s) derived in section 2.5 and the measured spring constant mentioned before the trap radius in the radial direction is determined to be (96±19) µm. From the measured ratio of the trap radius in the radial and axial direction the volume of the trap is given by $V=(\sqrt{2\pi}\,w_R)^3/1.2$. Since the measured spring constant is consistent with the theoretical value, we will use the above method to determine the trap volume with the theoretical spring constant. Together with the number of trapped atoms in Fig. 2.15 a maximum density of $5.0\cdot10^{11}$ atoms/cm^3 has been reached.

For a small number of trapped atoms the density is proportional to the number of trapped atoms. As the number of trapped atoms increases the reabsorption of scattered photons will create a

24

repulsive force between the trapped atoms. Using Gauss's theorem, it is shown [Ses 91, Tow 95] that such a multiple scattering of photons leads to a limit to the attainable trapped density which is independent of the number of trapped atoms given by

$$n_{max} = \frac{3\kappa c}{I_{tot}\sigma_L^2(\frac{\sigma_R}{\sigma_L}-1)}$$

(2.16)

where κ is the spring constant of the trap, σ_L is the absorption cross section for the trapping laser, and σ_R is the absorption cross section for reradiated photons from the trapped atoms. The value of σ_L is given by eq. 2.28. The calculation of σ_R is more subtle. The spectral distribution of the reradiated light consists elastic and inelastic contributions. The elastically scattered light has the same spectral distribution as the trapping laser, while the inelastic scattering has a Lorentzian form at low light intensity and appear to the form of Mollow triplet at high intensity [Lou 83]. A. Steane et al. have analyzed this problem and got an approximation relation between σ_L and σ_R [Ste 92b]:

$$\frac{\sigma_R}{\sigma_L}-1 = \frac{s}{s+1}\frac{\Delta^2}{s(\Delta^2+\frac{\Gamma^2}{4})+\frac{\Gamma^2}{4}}$$

$$with \quad s = \frac{\Omega^2/2}{\Delta^2+\Gamma^2/4}$$

(2.17)

where Ω is the Rabi frequency.

According to eq. 2.16 the maximum achievable density for our trap is $2\cdot10^{12}$ atoms/cm^3. This value is larger than that for alkali atom traps ($10^{10}\sim10^{11}$ atoms/cm^3) [Wal 90, Rit 94, Tow 95] since we have larger κ and shorter wavelength. The present trap density is still below this multiphoton scattering regime. This means the size of trap is independent of the number of trapped atoms and eq. 2.15 is valid. This is also confirmed by a comparison of the trap size for a trap filled by the thermal beam and a trap filled by a laser decelerated atomic beam.

2.3.2 Dynamics of the trap

The rate equation which determines the number of trapped atoms is given by

$$\frac{dN}{dt} = R - \alpha N - \beta \int n^2(r)\, d^3r \qquad (2.18)$$

where R is the loading rate, α and β describe generally the loss due to collisions with background atoms and the collision between the trapped atoms.

When the trap density is low the second order term can be neglected and eq. 2.18 has the solution:

$$N(t) = N_s - (N_s - N(0))\, e^{-\alpha t} \qquad (2.19)$$

where $N_s = R/\alpha$ is the number of trapped atoms in steady state. The linear loss coefficient α determines the loading time constant and also the lifetime of the trap (=$1/\alpha$). For a Mg MOT both background gas collisions and photoionization of the trapped atom will contribute to α.

The loss rate due to background gas collision is proportional to the vacuum pressure. By stopping the atomic beam and measuring the decay curve of the fluorescence for different vacuum pressure, D. Bettermann has measured this rate to $\alpha_P = (3.31 \pm 0.06) \cdot 10^7 \cdot p$ mbar^{-1}s^{-1}, where p is the vacuum pressure. During this experiment the vacuum is better than $6 \cdot 10^{-9}$ mbar and the loss rate due to background gas collisions is smaller than 0.2 s^{-1}.

The second contribution to α is photoionization. Since the photoionization energy of Mg is only 7.64 eV, two UV photons are sufficient to ionize Mg atoms. The loss rate due to this process is proportional to the population of the excited state N_{ex}, the ionization cross section σ_{PI} of the excited state $^1P_1$ and the photon flux [Din 92]

$$\left(\frac{dN}{dt}\right)_{PI} = \frac{I_{tot}}{\hbar\omega_L} \cdot \sigma_{PI} \cdot N_{ex}$$

$$and \quad N_{ex} = N \cdot \frac{1}{2} \frac{\dfrac{I_{tot}}{I_{sat}}}{1 + \dfrac{I_{tot}}{I_{sat}} + \left(\dfrac{2\Delta}{\Gamma}\right)^2} \qquad (2.20)$$
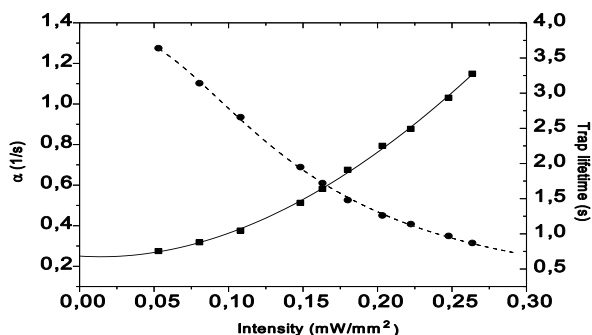
where $I_{tot}=6I_s$ is the total trapping laser intensity.

This leads to an additional linear lost term α_{PI} given by

$$\alpha_{PI} \ = \ \frac{I_{tot}}{\hbar\omega_L}\cdot\sigma_{PI}\cdot\frac{1}{2}\frac{\dfrac{I_{tot}}{I_{sat}}}{1+\dfrac{I_{tot}}{I_{sat}}+(\dfrac{2\Delta}{\Gamma})^2} \tag{2.21}$$

From the decay curve of the trap fluorescence by stopping the atomic beam the value of α and the trap lifetime $\tau=1/\alpha$ can be derived. Fig. 2.17 shows the measured α and τ as a function of the intensity of each trapping beam. Extrapolating the curve to zero intensity the trap loss due to background gas collisions is determined to be 0.21 which corresponds to the trap loss of a

Fig. 2.17: The linear trap lost α and the trap lifetime vs. the trap intensity of each laser beam. The trap loss at zero intensity is due to background gas collision. Square: α, Circle: τ.

background pressure of $6\cdot10^{-9}$ mbar. The trap lifetime can reach 3s for total trapping light intensity of 0.5 mW/mm². From the curve for α the photoionization cross section is determined by fitting eq. 2.21 to the curve. This leads to a value of $\sigma_{PI}=(6.3\pm1.6)\cdot10^{-17}$ cm². This value is consistent with the theoretically calculated value $6.2\cdot10^{-17}$ cm² by Mendoza [Men 87]. This cross section has also been measured before [Bet 95, Sch 96, Ral 96] but the values determined in their measurements are about a factor of two larger than the present value. This is mainly due to the difference in the
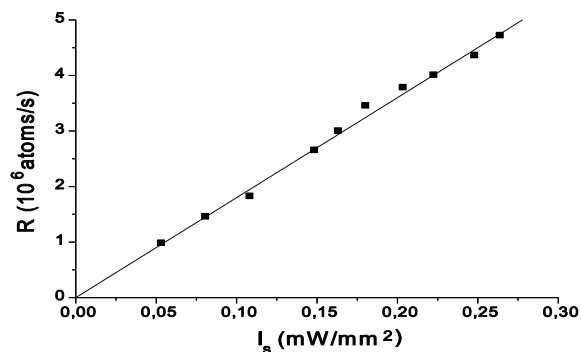

Fig. 2.18: The loading rate R from the slow atomic beam as a function of the single trapping intensity I_s.

measurement of the trapping intensity. In this work the power meter was calibrated with the help of another power meter calibrated by NIST. So the measured value is reliable.

27

From the measured number of trapped atoms and α the loading rate can be determined ($N=R/\alpha$). Fig. 2.18 shows the loading rate from the slowed atomic beam. It is linear to the trapping intensity

$$R = 1.8 \cdot 10^7 \cdot I_s \ atoms/s \qquad (2.22)$$

where I_s is in unit of mW/mm^2.

The loading rate from the thermal atomic beam is about a factor of 200 smaller than that from the slowed. This loading rate is related to the capture velocity v_c, under which the atom is captured. The velocity distribution in an effusive atomic beam is described by [Ram 56]

$$f(v) = 2 \frac{v^3}{v_b^4} e^{-\frac{v^2}{v_b^2}} \qquad (2.23)$$

where $v_b = 1.22 v_p$, with v_b and v_p is the most probable velocity in the atomic beam and oven, respectively. Since the trapping laser beam has a larger radius than that of the atomic beam in the trap center, we assume that atoms with a velocity smaller than v_c will be trapped. With an atomic beam intensity of I_b the capture rate from the thermal beam is given by

$$\begin{aligned} R &= I_b \int_0^{v_c} f(v)\,dv \\ &\approx \frac{I_b}{2} \frac{v_c^4}{v_p^4} \qquad for \ v_c \ll v_p \end{aligned} \qquad (2.24)$$

This capture rate is similar to that from a vapor cell [Wal 90] and is proportional to v_c^4. From eq.2.22/200 and eq. 2.24 the dependence of capture velocity on the trapping intensity can be derived:

$$v_c = 25.8 \cdot I_s^{1/4} \ m/s \qquad (2.25)$$

where I_s is in unit of mW/mm². For typical trapping intensity I_s varies from .05 to .3 mw/mm² v_c is between 12~20 m/s. This capture velocity is important for the determination of the trap loss due to collisions between trapped atoms. In general it depends on the direction of motion of the atoms, so what we derived here is actually an effective capture

Fig. 2.19: The dependence of the velocity capture range v_c on the trapping intensity I_s.

velocity. This parameter is not easy to access experimentally. It has been measured for a Rb trap using cold collisions [Hof 96].

Suppressing the Photoionization Loss by means of a Dark MOT

Since the photoionization effect is strongly dependent on the trapping intensity it can be minimized by reducing the intensity in the trap center. A trapping geometry to do this is the dark-spontaneous-force trap (SPOT) which has been realized in alkali element to increase the trapping density [Ket 93]. For alkali atoms the dark SPOT is done by eliminating the repumping laser in the trap center. Since Mg $^1S_0$ state has no Zeeman sublevel the dark SPOT can only be directly realized on the trapping laser beam which means that the center of the trapping laser beam has no intensity. This can be realized by covering the center of the laser beam with a dark spot. In order to avoid the refraction from the spot it should be imaged at the center of the trap through lenses. Of course, when the center of the trapping beam is dark there is also no trapping force in the center. This results in a leakage tunnel for the trapped atoms. If the dark zone is much smaller than the dimension of the trapping
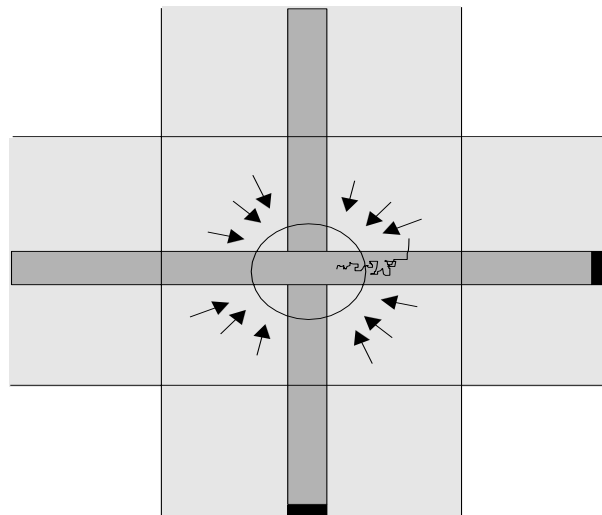
Fig. 2.20: A schematic dark SPOT for Mg to suppress the photoionization effect.

beam atoms leak to the dark tunnel still have more probability to diffuse to one of the four

29

quadrants where the average central force pushes the atoms back to the trap again as shown in Fig. 2.20. From a Monte-Carlo simulation for a trapping beam radius of 3 mm and intensity I_s of 0.06 mW/mm^2 it is calculated that atoms can still be trapped for a dark hole of radius up to 150 µm. The effect of photoionization can be suppressed in this case by more than 80% [Deg 96].

The photoionization effect not only influence the linear trap loss term α but also the β parameter. Since for high trap density the absorption of photons from the trapped atoms can reduce the trapping intensity. This will therefore reduce the effect of photoionization and results in a negative quadratic loss rate coefficient. The attenuation of the trapping intensity by the atom cloud to first order can be written as

$$I(r) \approx I_0 (1 - \sigma_L \int_{-\infty}^{z} n(x,y,z') \, dz')$$

(2.26)

where σ_L is the photon absorption cross section. The summation of the six trapping beams leads to an intensity distribution in the trap given by

$$I_{tot}(r) = 6 I_0 (1 - \frac{1}{3} \sigma_L n_0 \sqrt{2\pi} \sigma_t [e^{-\frac{x^2+y^2}{2\sigma_t^2}} + e^{-\frac{x^2+z^2}{2\sigma_t^2}} + e^{-\frac{y^2+z^2}{2\sigma_t^2}}]$$

(2.27)

where the trap density distribution n(r)=n_0 exp[-r^2/2σ$_t$] with a width of σ$_t$ is used. Substituting the above equation into eq. 2.20 and integrating over the volume leads to

$$(\frac{dn_0}{dt})_{PI} = \alpha_{PI} n_0 + \beta_{PI} n_0^2$$

(2.28)

where α_{PI} is just the term in eq. 2.21 and $\beta_{PI} = -\sqrt{2\pi} \sigma_L \sigma_t \alpha_{PI}$. The mean absorption cross section σ_L in a standing light field is given by [Ses 91, Sie 71]

$$\sigma_L = \frac{\lambda^2}{2\pi} \frac{1}{\sqrt{(1 + \frac{4\Delta^2}{\Gamma^2})(1 + \frac{I_{tot}}{I_{sat}} + \frac{4\Delta^2}{\Gamma^2})}}$$

(2.29)
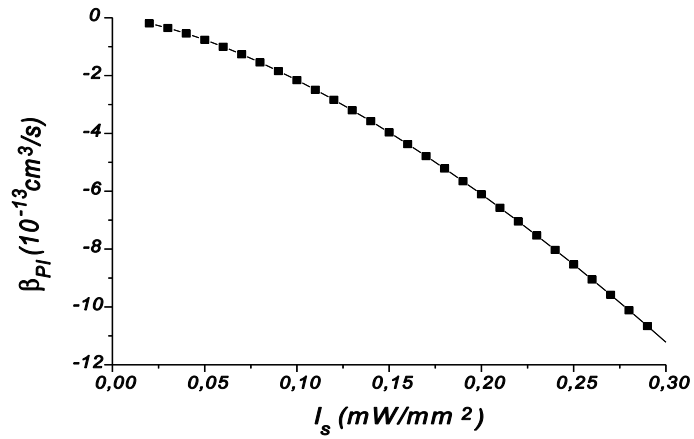
Fig. 2.21: Calculated photoionization induced negative β_{PI}.

For a trap radius of 100μm the value of β_{PI} varies from $-7.6 \cdot 10^{-14}$ to $-8.5 \cdot 10^{-13}$ cm^3/s for a trapping intensity of 0.05 ~0.25 mW/mm^2 as shown in Fig. 2.21. This negative β_{PI} together with the positive β_{col} caused by the collisions between the trapped atom will change and determine the total β. The trap loss due to collisions will be discussed in the next section.

2.4 Cold collisions

When the density of the trap is high enough the trap loss due to inelastic collisions between trapped atoms must be considered. In general inelastic cold collisions can be distinguished into two types.

First type of collision occurs in the absence of an light field and only atoms in the ground states contribute. Usually only binary collisions are considered. For alkali atoms collision effects are e.g. the hyperfine structure (HFS) changing collisions or dipolar decay. For noble gas penning ionization is an additional process. In the BEC regime three body recombination is important and it is the dominate trap loss for the Rb and Na BEC in the F=1, m_F=-1 state [Boe 96, Bur 97].

The second type collisions happens in the presence of a light field. Such collisions are one of the main trap losses in a MOT and will be discussed in more detail in this chapter.

The basic principle of cold collisions between trapped atoms introducing a loss in a MOT is the fact that in normal trap the laser is red detuned to the atomic resonance. This red detuned laser can excite the colliding atoms to an excited molecular state as indicated in Fig. 2.22. The atoms then interact via an attractive long range dipole-dipole potential, $V(r)=-C_3/r^3$. This potential is much larger than that between two atoms in ground state $(1/r^6)$.
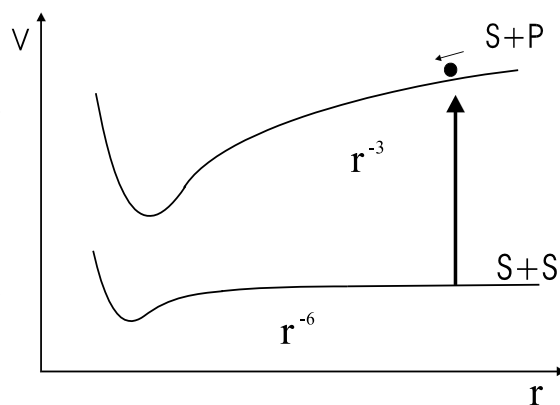
At room temperature the radiative lifetimes (~10^{-8} s) are much longer than the collision times (~10^{-12} s) so that spontaneous emission can be neglected.

Fig. 2.22: Long range potentials for two atoms both in the ground states and that for an atom in the ground state and the other in the excited state.

This is not the case for atoms cooled to milikelvin temperature and below. Spontaneous emission can happen during the collisions, a novel and interesting effect in cold collisions. If spontaneous emission happens the quasi-stable excited molecule will decay to the ground state under emission a red detuned photon. The excess energy will be distributed to the two atoms. When the energy is large enough the atom will leave the trap and cause trap loss which is called radiative escape. Atoms not energetic enough to leave the trap will also heat the trapped atoms which results in additional radiative heating. Without spontaneous decay the atoms follow the diatomic potential to small interatomic distances where HFS or fine structure (FS) changing processes can happen.

32

For alkali atoms spontaneous emission will eventually happen and the atom gains energy equal to the HFS or FS splitting which is usually larger than the trap depth. For alkali earth atoms the only possible collisional trap loss is the radiative escape.

In the past few years cold collisions have been intensively studied for alkali atoms and noble gases [Wal 94, Wei 95]. The collisional trap loss which is characterized by the β parameter is derived by observing the decay of the trap fluorescence when the trap process is interrupted or by direct measuring the additional trap loss induced by an additional catalysis laser injected onto the trap. Since the spontaneous emission must be considered in studying the collisional trap loss, only two level systems have been treated theoretically [Jul 93]. Hyperfine structure and multilevel system are still difficult to handle. For alkali earth elements there are four excited levels to be considered, which are the $^1\Sigma_g^+$, $^1\Sigma_u^+$, $^1\Pi_g$ and $^1\Pi_u$ states. Both $^1\Sigma_g^+$ and $^1\Pi_g$ are not optically coupled to the ground state and only the $^1\Sigma_u^+$ state with attractive potential can lead to a trap loss. It can be treated as a pure two-level system. This makes it possible to quantitatively compare the measurement and theoretical prediction. In section 2.4.1 the simplest collision model, the Gallagher-Pritchard model (GP model) [Gal 89], will be used to calculate the collisional trap loss for a Mg MOT.

The absorption of light by colliding atoms is the phenomenon that characterizes the photoassociative process. Extending such a process to large detunings allows for high resolution photoassociative spectroscopy with cold trapped atoms [Let 95]. This spectroscopy can provide information about the potential curves for both the excited and ground state molecules. These information are important for the cold collision physics. In section 2.3.2 more details about this technique will be discussed.

2.4.1 Collisional trap loss in a Mg MOT

The GP model assumes a stationary ground-state atom pair and assume that the excitation rate of this pair to the excited attractive state is given by

$$R_{ex}(r,\omega_L,I_L) \;=\; \frac{(\Gamma_M/2)^2}{[\omega_L-\omega(r)]^2+(\Gamma_M/2)^2]}\frac{I_L}{\hbar\omega_L}\frac{\lambda^2}{2\pi} \qquad (2.30)$$

where ω_L, I_L is the frequency and intensity of the laser, $\omega(r)=\omega_0-C_3/r^3\hbar$ is the molecular transition

33

frequency, ω_0 is the atomic resonance frequency and λ is the wavelength of the transition. The rate Γ_M is the decay rate of the molecular excited state. It generally depends on the separation of the atoms and to first order approximation it can be taken as a constant $\Gamma_M = 2\Gamma_A$ where Γ_A is the decay rate of the excited atomic state. Fig. 2.23 shows the excitation rate as a function of the separation of the atoms for various laser detunings $\Delta = \omega_L - \omega_0$.
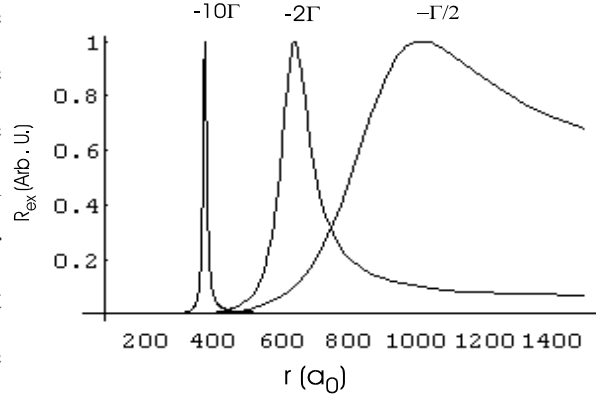
Fig. 2.23: Excitation rate of the ground state atom pairs as a function of interatomic separation (in atomic units).

The excited atom pair then moves along the attractive potential curve until spontaneous decay happens at a distance r_0.

The radiative decay of the atoms during their collision can be distinguished into two regions. When they decay at large separation $r_0 > r_{RE}$, they gain kinetic energy $\Delta E = C_3/r^3 - C_3/r_0^3$ which is smaller than the trap depth and will stay in the trap. For a decay at a short separation $r_0 < r_{RE}$ the atoms will escape from the trap. The distance r_{RE}, where the radiative escape dominates depends on the trap depth. Atoms will be lost only, when they can survive i.e. stay in the excited state till r_{RE} and then decay during $r_0 < r_{RE}$. So the probability of radiative escape for a single collision is then given by $\eta\gamma$, where η and γ are the survival probability at r_{RE} and the decay probability for $r_0 < r_{RE}$ respectively. The time for atoms to travel from r to r_{RE} is equal to $\int_{r_{RE}}^{r} dr'/v(r')$, where $v(r')$ is the velocity at r'. The survival probability follows the usual exponential decay and can be written as

$$\eta = e^{-\Gamma_M \int_{r_{RE}}^{r} \frac{dr'}{v(r')}} \qquad (2.31)$$

where $v(r') = \sqrt{(2/\mu)(C_3/r'^3 - C_3/r^3)}$ and μ is the reduced mass.

The time duration which atoms travel from r_{RE} to 0 and back to r_{RE} is equal to $2(\int_0^{r} dr'/v(r') - \int_{r_{RE}}^{r} dr'/v(r'))$, so the decay probability for $r_0 < r_{RE}$ is given by

$$\gamma = 1 - e^{-2\Gamma_M [\int_0^{r} \frac{dr'}{v(r')} - \int_{r_{RE}}^{r} \frac{dr'}{v(r')}]} \qquad (2.32)$$

34

If the spontaneous decay does not happen at the first approach, the atoms may again separate out to the outer turning point r where the pair was excited, approach towards each other again, and so on. Thus, the total radiative escape probability is given by

$$P_{RE}(r) = \eta\gamma + (1-\gamma)\eta^2\eta\gamma + \ldots = \frac{\eta\gamma}{1-(1-\gamma)\eta^2}$$

(2.33)

The density of Mg-Mg pairs with separation r→r+dr is $(n^2/2)\cdot4\pi r^2\cdot dr$, where n is the density of trapped atoms and the factor 1/2 accounts for double counting. Integrating the product of the number of pairs, excitation probability and loss probability over the volume we get the total collisional loss rate:

$$R_{col} = \beta_{col}n^2 = 2\int_0^\infty \frac{n^2}{2}4\pi r^2 R_{ex}(r,\omega_L,I_L)P_{RE}(r)dr$$

(2.34)

where the factor 2 accounts for the loss of two atoms for each event.

Substitute eq. 2.30 and eq. 2.33 into eq. 2.34 β_{col} can be calculated as long as r_{RE} is determined. The distance r_{RE} is related to the trap depth or in terms of capture velocity v_c by $C_3/r_{RE}^3 - C_3/r^3 = mv_c^2$,where the initial velocity of the atoms is neglected since it is much smaller than v_c. The relation between v_c and the trapping intensity is given by eq. 2.25. The dependence of β_{col} on laser detuning is usually measured with an additional catalysis laser send onto the trap to have a trap depth independent photoassociation lasser. We will first calculate the β_{col} induced by such a catalysis laser and then go back to the trapping laser induced trap loss. The calculated β_{col} as a
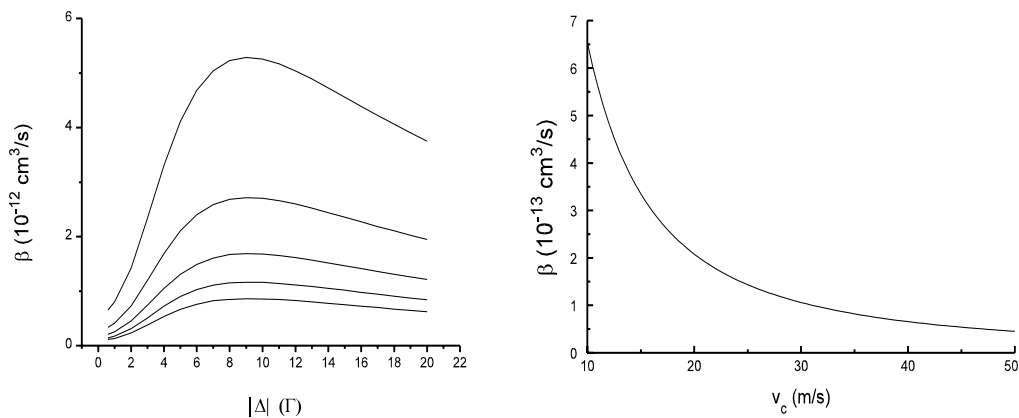

Fig. 2.24: Collisional trap loss induced by a catalysis laser as a function of its detuning and as a function of the capture velocity.

function of the catalysis laser detuning and the different capture velocities is shown in Fig. 2.24 for a catalysis laser intensity of 1 mW/mm². For small detuning the excitation probability is large but the survival probability is small and vice versa so there is an optimum detuning in between.

The calculation of trapping laser induced β_{col} must consider the simultaneous trapping intensity dependence of r_{RE} and $R_{ex.}$ The calculated β_{col} as a function of the single trapping laser intensity is shown in Fig. 2.25. β_{col} varies form $1 \cdot 10^{-13}$ to $4 \cdot 10^{-13}$ cm³/s for the usual trap intensity as shown. This value is much smaller than that for an alkali atom trap. This is because of the much shorter lifetime of the $^1P_1$ state of Mg and only radiative escape contributes. Most of the collisional atoms have not enough energy to escape from the trap after the optical collision. It should be note that the GP model does not consider the so the called population recycling [Hol 94] which is due to the re-excitation of decayed atoms. To take the population recycling into account the dispassive Liouille von Neumann equation for the density matrix must be solved. This lead to Monte Carlo wave function method [Møl 93].
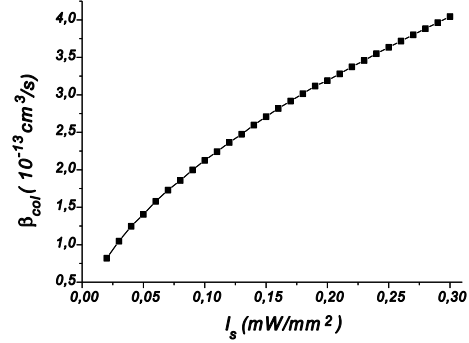
Fig. 2.25: Calculate β_{col} as function of the trapping laser intensity I_s.

Measuring the β parameter

The solution of eq. 2.18 for R=0 is

$$N(t) \;=\; \frac{N_0\alpha}{(\alpha+\beta N_0/V)\exp(\alpha t)-\beta N_0/V} \tag{2.35}$$

where V is the volume of the trap. The parameter β can be obtained by fitting the above equation to the decay curve of the fluorescence. This parameter has been measured with a photo multiplier tube (PMT) and a much larger negative value than theoretically expected has been obtained [Bet 95, Sch 96]. In this work the fluorescence was detected by a PMT and a photodiode. When the fluorescence is measured with a PMT the time resolution should be taken into account. In photon counting mode each pulse has a finite width, the overlapping of the pulse can not be neglected when the photon countrate is high. Since the photon scattering follow the Poission

distribution, the probability of counts by pulse overlaps can be described by the following formula [Ham 93].

$$P_o = 1 - e^{-R_r T} \qquad (2.36)$$

where R_r is the average countrate and T is the resolving time of the photo-counting system. In our case T is mainly determined by the photoelectron current pulsewidth of the PMT i.e. 25 ns. At a count rate of 10^6 atoms/s the overlap probability is 2.5%. This will affect the evaluation of the decay curve of the fluorescence and should be corrected. When $R_r T \ll 1$ The real countrate R_r can be approximated by $R_r = R_m/(1-R_m T)$, where R_m is the measured countrate. During the measurement of β parameter the fluorescence has been corrected to get the real countrate. The photodiode usually has
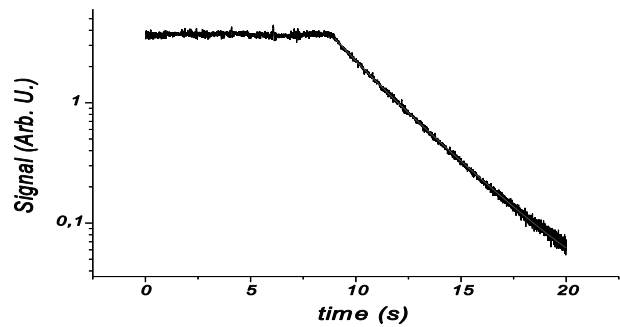
Fig. 2.26: Trap fluorescence measured by photodiode. The decay begins when the atomic beam is interrupted.

a large dynamic range where the linearity is still maintained. Nonlinearity can happen in the case of a strong focusing which has been carefully avoided in this measurement.

Fig. 2.26 shows an example of the decay of the trap fluorescence measured by the photodiode. The steeper slope at the beginning of the decay curve indicates a positive β value. The measured β with photodiode and PMT are shown in Fig. 2.27. The trap volume is determined with the trap temperature and spring constant described in section 2.3. For the measurements with the PMT some β measurements with and without corrected countrate for various incident light are checked for the same trap
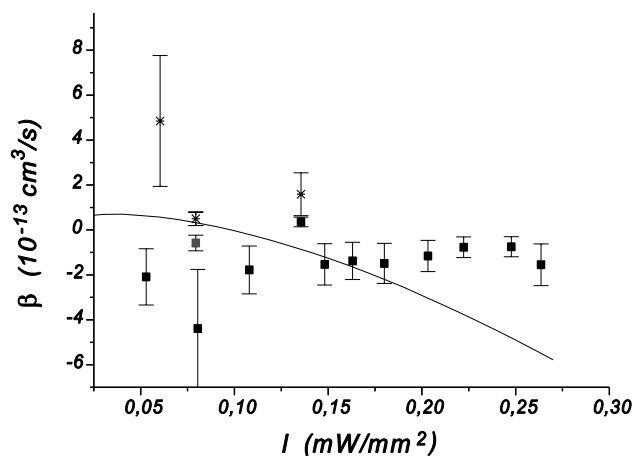
Fig. 2.27: Measured β v.s. the single trap intensity. The star is measured from the PMT. The solid line is the theoretically expected value .

intensity. We conclude that the large negative β value measured before is mainly due to the nonlinearity of the PMT. The solid line in Fig. 2.27 is the theoretically expected value with no consideration of population recycling i.e. the sum of Fig. 2.21 and Fig. 2.25. At low intensity both positive and negative β-values have been measured. Since at this regime the β value is very small the discrepancies is mainly due to the fluctuation of the fluorescence rate. The deviation from the theoretical expectation at larger intensity is assumed to be the effect of population recycling which increases the theoretically predicted β value shown in Fig. 2.27. At the present trap intensity this additional effect is expected to be smaller than $5 \cdot 10^{-13}$ cm^3/s.

2.4.2 Photoassociative spectroscopy

The above treatment of the trap loss the trapping laser is red detuned a few linewidth from the atomic resonance. In this regime the molecular state is usually very dense and not resolvable. When a further detuned catalysis laser is used the trap loss exhibits a discrete peak spectrum resulting from trap loss due to photoassociation excitation followed by spontaneous emission. Such a spectrum from cold atoms shows high resolution comparable to bound-bound spectroscopy as first pointed out by Thorsheim et al. [Tho 87]. In a quantum picture the transition is from a free-particle-scattering state to a discrete bound state with a transition probability proportional to the Franck-Condon factor. For free atoms the Franck-Condon factor is the largest for the high lying levels. Therefore, the typical photoassociation spectroscopy of cold atoms shows an unresolvable spectrum near dissociation and resolved high lying levels when the catalysis laser is scanned from atomic resonance toward red detuning [Mil 93, Let 93]. These high lying levels are difficult to access from the bound molecular ground state. Therefore, photoassociative spectroscopy is a powerful method which complements conventional bound-bound spectroscopy. When combining the two regimes precise molecular potential constants can be determined [Jon 96, Lin 96].

Starting from the semicalssical quantization condition [Lan 77]

$$v + \frac{1}{2} = \frac{1}{\hbar} \int_{R_1(v)}^{R_2(v)} \sqrt{2\mu \left[E_v - V(R) \right]} \, dR \qquad (2.37)$$

where E_v is the energy of level v and $R_1(v)$ and $R_2(v)$ are the classical inner and outer turning point respectively, LeRoy and Bernstein show that the binding energy of high lying levels depends only upon the long-range potential C_3/R^3 and satisfies the relation [LeR.70]

$$D - E_v = (\frac{\pi}{2a})^6 (\frac{\hbar^2}{2\mu})^3 \frac{1}{C_3^2} (v_D - v)^6 \qquad (2.38)$$

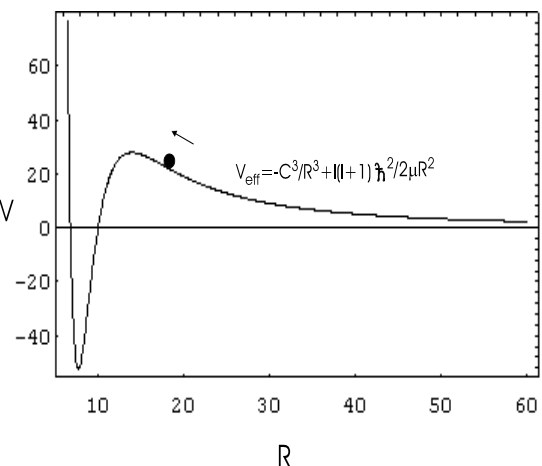where a=1.120251, v_D is the effective quantum number at the dissociation limit and D is the dissociation energy. The binding energy $D-E_v$ can be measured from the photoassociation spectroscopy, i.e. $D-E_v = \hbar\omega_0 - E_b(v)$, where ω_0 is the atomic resonance frequency and $E_b(v)$ is the measured energy of level v. Fit of the measured binding energy to eq.2.38 the long range

39

potential coefficient C_3 can be obtained. Since C3 is proportional to the square of the dipole matrix element, which in turn is inversely proportional to the excited state lifetime τ [Kin 39] and satisfies the relation

$$C_3 = \frac{3\hbar}{2\tau}\left(\frac{\lambda}{2\pi}\right)^3 \ , \tag{2.39}$$

the life time of the excited state can then be precisely determined by the measurement of C_3 [Abr 95].

The photoassociative spectroscopy for the transition $A^1\Sigma_u^+ \leftarrow X^1\Sigma_g^+$ in the Mg MOT is difficult to detect through trap loss because photoionization rate is much larger than the collisional trap loss rate. In the scope of a current DFG project in this group, a far-off resonant optical trap (FORT) is planed. In a FORT the atomic density is usually larger than 10^{12} atoms/cm^3. When a catalysis laser is far detuned from atomic resonance the population of the $^1P_1$ excited state is small and the trap loss due to photoionization can be neglected. Also the trap depth of the FORT is some mK. The corresponding capture velocity is only about 3 m/s and the β_{col} can be larger than 10^{-11} cm^3/s. As a consequence the collisional trap loss induced by the catalysis laser should easily be detected.

Fig. 2.27: The centrifugal barrier of the effective potential V_{eff}

For alkali earth elements there is another photoassociative spectroscopy can be done with the triplet transition $A^3\Sigma_u^+ \leftarrow X^1\Sigma_g^+$ in the MOT. A rough estimate of the collisional trap loss coefficient β is given by [Jul 93]:

$$\beta = \frac{\pi v}{k^2}(l_{max}+1)^2\bar{P}_{PA} \tag{2.40}$$

where the center-of-mass collision energy is $\epsilon = \hbar^2k^2/2\mu$, v is the velocity of the colliding particles and $\bar{P}_{PA}$ represents the mean probability of photoassociative trap loss over partial waves whose maximum angular momentum is l_{max}. The maximum angular momentum is

40

determined by setting the collision kinetic energy 3kT/2 equal to the centrifugal barrier of the effective potential $V_{eff} = -C_3/R^3 + l(l+1)\hbar^2/2\mu R^2$. For a Mg trap at Doppler temperature it can be shown that only s-wave scattering contributes. Due to the long lifetime of the triplet excited state atom pairs excited to this state have a loss probability of 1 and $\bar{P}_{PA}$ then only depends on the effect of excitation. Taking l_{max}=0 eq. 2.40 can then be written as

$$\beta = 1.8 \cdot 10^{-11} \cdot P_{ex} \quad cm^3/s \tag{2.41}$$

where P_{ex} is the excitation probability.

For a typical power of 50 mW @ 457nm focused down to a radius of 0.5 mm the intensity is 12 W/cm^2. This is much larger than the saturation intensity (40 nW/cm^2) of the triplet transition of the atom. Thus a loss rate coefficient as high as 10^{-11} cm^3/cm is possible. For a trap density of 10^{11} atoms/cm^3 a loss rate coefficient down to 10^{-13} can still be detected.

Through photoassociative spectroscopy of cold atoms information on ground state potentials can also be obtained. A precise knowledge of the ground state potential is important for the determination of the s-wave scattering length which is relevant for the stability of BEC [Sto 94b]. By analyzing the line shape of the spectra a precise ground state potentials can be determined [Nap 94]. From the intensity distribution of the spectra the sign of the s-wave scattering length can be obtained [Abr 95]. The intensity distribution has a minimum for positive scattering length and the location of the minimum precisely determines the scattering length [Côt 95, Abr 96].

In the FORT project a new cooling method based on the triplet transition will be developed [Rus 98]. High phase space density towards the quantum degenerate seems possible. In such a regime the s-wave scattering length determines the collisional properties. In next section the s-wave scattering length of Mg ground-state atoms is theoretically studied with semiclassical methods using the available Mg$_2$ ground-state potential.

2.4.3 The s-wave scattering length of ^{24}Mg

The scattering from a central potential V(R) is usually treated by partial-wave expansion of the scattering wave function [Coh 77]. The Schrödinger equation is then reduced to the determination of the radial wavefunction $u_l(R)$ of the lth partial-wave i.e.

$$[\frac{d^2}{dR^2}+k^2-\frac{l(l+1)}{R^2}-U(R)]u_l(R)=0 \qquad (2.42)$$

where $k=\sqrt{2\mu E}/\hbar$ is the wave number, E is the total energy, $U(R)=2\,\mu V(R)/\hbar$ and V(R) is the interatomic potential. Since we are only interested in the result after the scattering, only the asymptotic solution for R→∞ is important. The asymptotic solution of eq. 2.42 can be written as [Joa 75]

$$u_l(R)\approx A_l\sin(kR-l\pi/2+\delta_l) \;, \quad R\rightarrow\infty \qquad (2.43)$$

where δ_l is the scattering phase.
The scattering from V(r) is then characterized by a total cross section

$$\sigma_{el} \;=\; \frac{4\pi^2}{k^2}\sum_{l=0}^{\infty}(2l+1)\sin^2\delta_l \qquad (2.44)$$

At low energy only s-wave (l=0) scattering contributes. This process can be characterized by a scattering length:

$$a \;=\; -\lim_{k\rightarrow 0}\frac{\sin\delta_0(k)}{k} \qquad (2.45)$$

The s-wave scattering cross section in this low energy limit is then $\sigma_{el}=4\pi a^2$ and the wave function near zero energy is reduced to

$$u_0(R) \underset{R\rightarrow\infty}{\rightarrow} A(R-a) \qquad (2.46)$$

42

The scattering length has a simple geometrical meaning: it is the intersection of the asymptote to $u_0(R)$ with the R axis.

The scattering length for a long range potential of the form $V(R)=-C_n/R^n$ is found by Gribakin and Flambaum [Gri 93] in a semiclassical approach.

$$a = \bar{a}\left[1-\tan(\frac{\pi}{n-2})\ \tan\left(\Phi-\frac{\pi}{2(n-2)}\right)\right] \tag{2.47}$$

where

$$\bar{a}=\cos(\frac{\pi}{n-2})\left(\frac{\sqrt{2\mu C_n}}{\hbar(n-2)}\right)^{\frac{2}{n-2}}\frac{\Gamma(\frac{n-3}{n-2})}{\Gamma(\frac{n-1}{n-2})} \tag{2.48}$$

is the mean scattering length and

$$\Phi=\frac{1}{\hbar}\int_{R_0}^{\infty}\sqrt{2\mu[-V(R)]}\ dR \tag{2.49}$$

Here Φ is just the semiclassical phase calculated at zero energy from the classical turning point R_0 to infinity and $V(R_0)=0$. The mean scattering length is solely determined by the long range potential. To calculate Φ the actual potential curve must be known.

The Mg$_2$ potential

The absorption spectrum of Mg$_2$ has been observed and analyzed by Balfour and Douglas [Bal 69,72]. An empirical Rydberg-Klein-Rees (RKR) potential curve for the ground state $X\,^1\Sigma_g^+$ is constructed at the internuclear distances between 6.18 a_0 and 13.63 a_0, where a_0 is the Bohr radius ($a_0=0.529177$Å). It is almost identical in shape with a Morse potential

$$U(R-R_e) = D_e[1-e^{-\beta(R-R_e)}]^2 \tag{2.50}$$

with $\beta=1.0543$, $D_e=424$ cm^{-1}, $R_e=3.890$Å.

At large distance the dispersion potential is described by

$$V(R) = D_e - \frac{C_6}{R^6} - \frac{C_8}{R^8} - \frac{C_{10}}{R^{10}} - \dots \tag{2.51}$$

The theoretical value $C_6 = 3.29(\pm 0.17) \cdot 10^6$ cm^{-1}Å^6 has been calculated by Stwally [Stw 71]. By plotting $V(R) + C_6/R^6$ vs. R^{-8} for Balfour's data he has reported $C_8 = 0.51(\pm 0.09) \cdot 10^8$ cm^{-1}Å^8 and $D_e = 429.26(\pm 0.5)$ cm^{-1}. No appreciable C_{10}/R^{10} correction is needed [Li 73]. Vidal and Scheingraber use the "inverted perturbation approach" (IPA) method analyzing the data of Balfour and get $C_6 = 3.88(9) \cdot 10^6$ cm^{-1}Å^6, $C_8 = 3.26(38) \cdot 10^7$ cm^{-1}Å^8 and $D_e = 430.97(0.15)$ cm^{-1} [Vid 77].

Similar to the treatment of Gribakin we adopt the following expression for the Mg$_2$ $X^1\Sigma_g^+$ potential curve:

$$U(R) = -D_e + D_e(1 - e^{-\beta(R - R_e)})^2 - (\frac{C_6}{R^6} + \frac{C_8}{R^8}) f_c(R) \tag{2.52}$$

where the zero potential has been defined at R=∞.

Here $f_c(R)$ is a cutoff function introduced to cancel the $1/R^n$ divergence at small distance and is given by

$$f_c(R) = \Theta(R - R_c) + \Theta(R_c - R)e^{-(R_c/R - 1)^2} \tag{2.53}$$

where $\Theta(x)$ is a unit step function: $\Theta(x) = 1$ (0) when x > (<) 0. We fit the eq. 2.53 to the RKR potential to get β and R_e instead of the value from Balfour for the parameters from Stwally and Vidal. The best cutoff radius R_c is also determined by the fit. Fig. 2.28 shows the RKR potential from Balfour and the fitted curve of eq. 2.52 using the
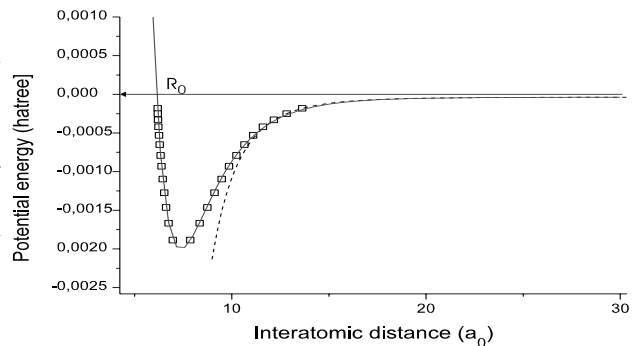
Fig. 2.28: RKR potential curve of Mg$_2$ ground state. The Solid line is the fit curve of eq. 2.52. The dashed line is the long range potential.

44

parameter of Vidal. Also shown is the dispersion potential. The scattering length is then calculated according to eq. 2.47 for both parameter sets from Stwally and Vidal. The calculated scattering length is shown in Table I.

	C_n, D_e Stwally	C_n, D_e Vidal	Balfour
β	0.5657	0.5658	0.5579
R_e	7.3638	7.3620	7.3510
R_c	28.03	27.61	
a	2802	58	

Table I: Calculated s-wave scattering length.
The above values are given in atomic units.

To see the effect of the position cutoff R_c we have also calculated the scattering length as a function of R_c with the other parameters fixed. The result is shown in Fig. 2.29. The infinite
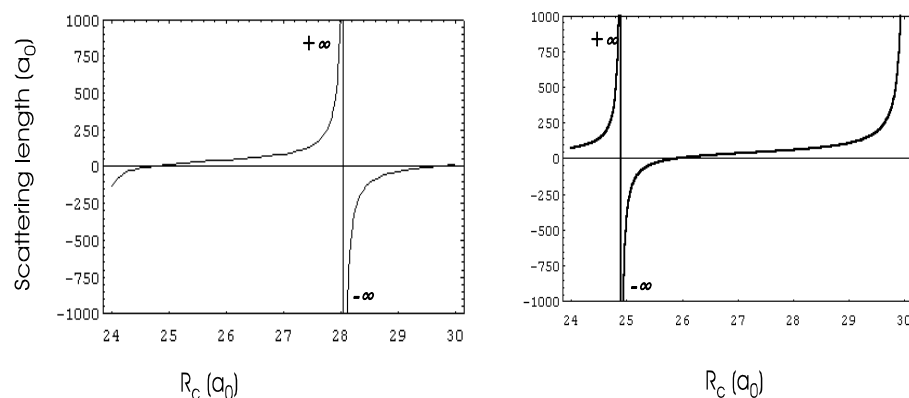
Fig. 2.29: The scattering length as a function of R_c. The C_n, D_e are cited from Left: Stwally and Right: Vidal

scattering length is due to the zero energy resonance which means the potential is nearly able to bind an s-state [Joa 75]. The scattering length is positive when an s-wave bound state exists otherwise it is negative. Recently, Arndt. et al. have reported the observation of such a zero-energy resonance in spin-polarized Cs-Cs collision [Arn 97].

For a bound state with small binding energy $E_b = \hbar^2 v^2/2\mu$ the scattering length is related to the effective range r_e by [Joa 75]

$$\frac{-1}{a} = -v + \frac{1}{2}r_e v^2 \qquad (2.54)$$

45

where r_e is defined by

$$r_e = 2 \int_0^\infty (v_0^0(R)^2 - u_0^0(R)^2)\,dR \qquad (2.55)$$

Here $v_0^0(R) = 1 - R/a$ and $u_0^0(R)$ is the solution of eq. 2.42 for the s-wave at zero energy (k=0) normalized such that at large R, $u_0^0(R) = v_0^0(R)$. It is clear that the scattering length is sensitive to the binding energy of the least-bound state. Such a binding energy can be directivly measured using two-photoassociation spectroscopy with cold atoms [Abr 95].

The scattering length calculated from Stwally's parameter has a very large positive value. This indicates that the highest bound state is very close to the dissociation limit. Also, because of the uncertainty of the parameters of the potential, there are possibilities for negative a ($-125a_0 > a > -2323a_0$) with the parameters of Stwally. However, the scattering length calculated from Vidals parameter gives $40a_0 < a < 161a_0$ within the uncertainty of the parameters. Since the scattering length is sensitive to the position of the last bound state, the uncertainty of the potential can easily change the last bound state to an unbound state and hence from positive a to negative a. Gribakin and Flambaum have also shown that the number of bound states is given by

$$n_b = \left[\frac{\Phi}{\pi} - \frac{n-1}{2(n-2)}\right] + 1 \qquad (2.56)$$

where [ ] denotes the integer part of the expression. From the calculated possible Φ it shows that there will be 19 or 20 bound states for $^{24}Mg_2$ ground state with the parameters of Stwally or Vidal, respectively. Because there are still large discrepancies between the potential parameters the position of the last bound state is still uncertain. The above estimated values should still be checked when a more precise molecular potential is available. The photoassociative spectroscopy of cold atoms mentioned above should help to solve this problem.

2.5 Dynamics of the pulsed trap and optimization for the spectroscopy

The main purpose of our trap is high resolution Ramsey-Bordé interferometry. For this experiment the trap will be operated in pulsed mode to eliminate some disturbing effects as described in chap. 4. In the pulsed mode the trapping laser beams are turned on and off alternatively. This is done by controlling the AOM as shown in Fig. 2.10. Since this AOM also regulates the intensity stabilization the transient response of the intensity controller

Fig. 2.30: Transient response of the trap fluorescence and error signal of the intensity controller.

has to be considered. Any intensity disturbance of the trapping beam is directly reflected in the fluorescence of the trap and increases noises. A good signal-to-noise ratio is important for the RBI experiment. To measure the transient response of the intensity controller and the trap fluorescence the trapping beam is therefore turned on and off at a rate of 50 Hz with turn off time of 1 ms. The measured error signal of the controller and the trap fluorescence are shown in Fig. 2.30. The over-shooting of intensity after turning on the trapping laser beam is also seen in the fluorescence of the trap. After turning off the trapping beam the atom cloud expands freely. When the trapping beam is turned on again the fluorescence is only 39% of the stationary value. This is due to the quadruple magnetic field which shifts more atom in the expanded cloud out of resonance. This effect also reduces the influence of the intensity over-shooting on the trap fluorescence. Furthermore, the width of the over-shooting is only 200 μs, so the signal-to-noise ratio of the trap fluorescence is only weakly deteriorated. Fig. 2.31 shows the measured noise of the
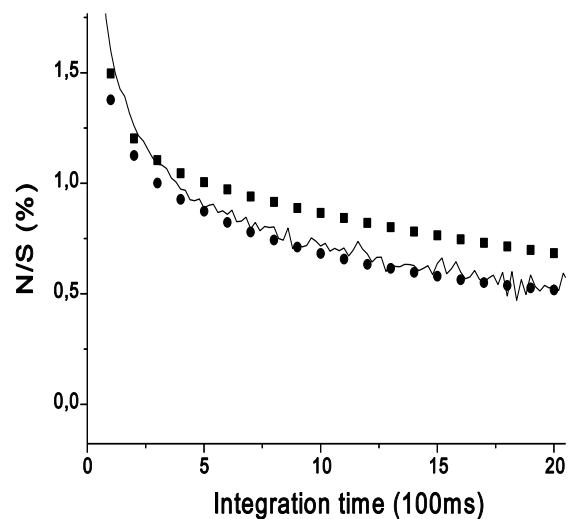
Fig. 2.31: Noise of the trap fluorescence and the trapping laser intensity as a function of the integration time. Square: Pulsed trap, Circle: cw trap, Line: trapping laser intensity

47

trap fluorescence as a function of the integration time for a cw trap and a pulsed trap. For an integration time of 1s the noise can be as low as 0.7 % for a cw trap and 0.9% for a pulsed trap. The solid line shown in Fig. 2.31 shows the fluctuation of the trapping intensity. It is seen that the noise of the trap fluorescence is mainly due to the fluctuation of the trapping intensity. This noise is also sensitive to the alignment of the trapping beam. Since the center of quadrupole magnetic coil is not at the center of the trapping chamber, the trapping beam is close to the wall of the chamber. Careful alignment is necessary to avoid background scattering from the chamber. After the over-shooting there is still a rise time of 350 µs in the fluorescence signal. This is the time require to damp the expanded atomic cloud to the stationary form described in section 2.1. During the turn off time t_{off} atoms with velocity $v > R_{tr}/t_{off}$ (R_{tr} is the trap region) will expand to a region larger than the trap region. After turning on the trapping laser beam these atoms are lost. The loss probability due to this effusive effect is the part of atoms with velocity larger than R_{tr}/t_{off} and is given by

$$
\begin{aligned}
\alpha_E \;=\; 2\int_{v_t}^{\infty} n(v)\,dv \;&=\; \sqrt{\frac{2}{\pi}}\,\sigma_v \int_{v_t}^{\infty} e^{-\frac{v^2}{2\sigma_v^2}}\,dv \\
&=\; 1 - Erf\!\left(\frac{R_{tr}}{\sqrt{2}\,\sigma_v t_{off}}\right)
\end{aligned}
\tag{2.57}
$$

where σ_v is the width of the velocity distribution. This is an error function dependent on R_{tr}, t_{off} and σ_v. The effusive loss as a function of the trapping laser off-time is shown in Fig. 2.32 with σ_v equal to the velocity of the Doppler cooling limit. For the RBI experiment this kind of loss should be as small as possible such that more atoms can contribute to the spectroscopy.
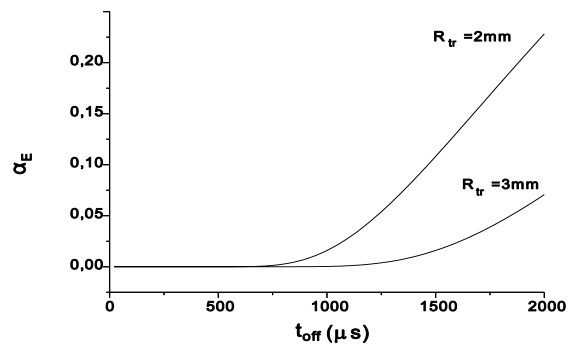
This effusive loss will result in a smaller number of trapped atoms than in the cw trap. For a pulsed trap with trapping laser off and

Fig. 2.32 The dependence of the effusive lost on the trapping laser off-time for different trap region R_{tr}.

on time of t_{off} and t_{on}, respectively, the number of trapped atoms before the next cycle is equal

to

$$N(t_{i+1}) \;=\; N_{cw} - [N_{cw} - (N(t_i) - \alpha_E N(t_i))]e^{-\frac{t_{on}}{\tau_{tr}}} \qquad (2.58)$$

where τ_{tr} is the life time of the trap and α_E is the effusive loss described by eq. 2.57.
In stationary state this leads to a new equilibrium state and the number of trapped atoms at the new equilibrium can be written as [Sen 93]

$$N_p = \frac{N_{cw}}{1 + \alpha_E \dfrac{e^{-\frac{t_{on}}{\tau_{tr}}}}{1 - e^{-\frac{t_{on}}{\tau_{tr}}}}} \qquad (2.59)$$

The measured N_p as a function of t_{off} is shown in Fig. 2.33. The solid line is a fit curve to eq. 2.59 with R_{tr} , σ_v , and τ_{tr} as the fitting parameter. It is seen that the behavior of the pulsed trap can be well predicted by eq. 2.59. This fitted lifetime τ_{tr}=0.9 s is the same as that derived from the decay curve of the trap fluorescence. The fitted velocity σ_v=0.94 m/s is consistent with the theoretically predicted value (0.87 m/s) within 10%.

Since the trap position can be varied by the compensation magnetic field, a proper compensation field can be tuned such that the trap is at the center of the cross of the trapping laser beam. It is observed that the trap fluorescence is not sensitive to the
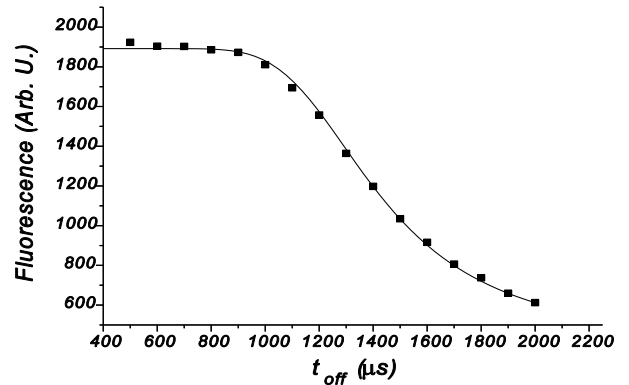
Fig. 2.33 The fluorescence of the pulsed trap as a function of the trapping laser off time. The solid line is theoretical fitted line with parameter R_{tr}=3 mm, σ_v =.94 m/s, τ_{tr} =0.9 s

change of the compensation field when the trap is operated in cw mode. However, it is sensitive when the trap is operated in pulsed mode. When the trap is not at the center position this results in higher effusive loss in the pulsed trap. In this situation the trap fluorescence changes

49

dramatically when the trap is changed from the cw mode to pulsed mode. Also the fluorescence drops very quickly in the pulsed trap when the trapping laser off-time is varied. This behavior can not be described by eq. 2.59 as shown in Fig. 2.34. The compensation field should be adjusted such that there is no significant change in fluorescence when the trap is changed from cw mode to pulsed mode. This confirms that the trap is at the center
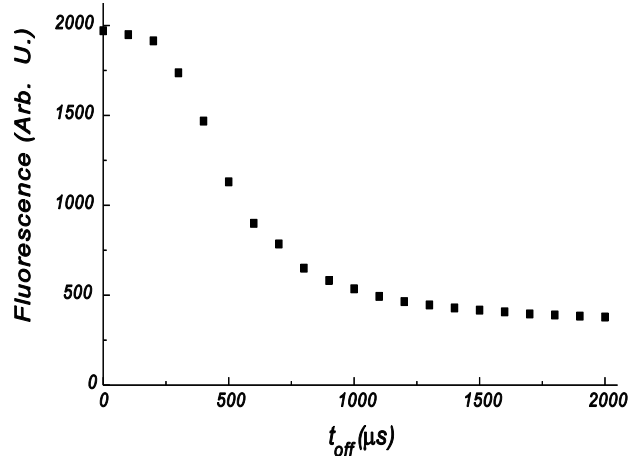
Fig. 2.34: Trap fluorescence as a function of the trapping laser off time when the trap is not at the center of cross of the trapping laser beam.

of the cross of the trapping laser beam. This is important for the RBI experiment with the trap, since for high resolution RBI the trapping lasers will be turned off longer than 1ms. A high contrast of fringes can only be obtained when the effusive loss is small. The RBI experiment with the trap will be described in detail in chap. 4.

Chapter 3

Ramsey-Bordé Interferometry (RBI)

Heisenbergs uncertainty principle limits the resolution of the spectral linewidth $\Delta\upsilon$ by the atom-field interaction time τ through $\Delta\upsilon\cdot\tau > 1$. To overcome this interaction time broadening N.F. Ramsey developed a two separated zone coherent spectroscopy in the microwave region [Ram 50]. The atomic coherence established in the first interaction zone precesses freely when the atom is in the dark region. At the second interaction zone the phase difference between the atomic coherence and the radiation field determines the final excitation probability. This method bas shown a spectral resolution of $\Delta\upsilon\cdot T = 0.65$. The time scale is now determined by the atomic coherence precession period T which is usually much larger than the atom-field interaction time τ. As a consequence precision increases by T/τ as compared to conventional spectroscopy.

In the microwave regime considered by Ramsey the wave length of the microwave field is much larger than the dimension of the interaction zone and the atomic beam spread. The spatial variation of the acquired phase in each interaction zone can thus be neglected. This is different for optical frequencies. The optical wave length is so small that atoms which cross the second zone will experience spatial dependent phase shifts of even more than π. This washes out the fringes when different trajectories are averaged. Baklanov et al. (1976) have used three equally spaced interaction zones with standing waves to recover the Ramsey fringes [Bak 76]. Later, Bordé has introduced a geometry with two pairs of counterpropagating traveling waves. Bordé showed theoretically that the fringes have more contrast [Bor 84]. Such a configuration has been interpreted as a Mach-Zehnder type interferometer [Bor 89]. Each laser beam can be viewed as a beam splitter. In the interaction zone the absorption and emission of a resonant photon will split the atomic wave into a coherent superposition of ground and excited state. As long as the excited state life time is long enough the two partial waves will recombine at the fourth interaction zone and cause interference at the two output ports. The final excitation probability i.e. the probability to appear in one of the output ports depends on the phase difference of the partial waves acquired during the interaction zone and the free propagation. In the following section the properties of traveling wave beam splitter will be described. The theoretical treatment of atomic interferometer signal will be given in section 3.2. Section 3.3 describes the influence of

additional potentials.

3.1 Light field as a beam splitter based on photon recoil

Consider an atomic beam crossing two pairs of counterpropagating laser beams. Each laser beam functions as a beam splitter. Therefore, the detailed Ramsey-Bordé geometry consists of 16 possible trajectories as shown in Fig. 3.1.
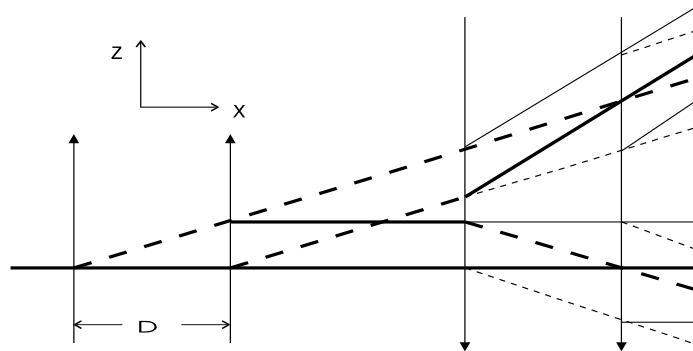
Fig. 3.1: Four zone Ramsey-Bordé interferometer. The two closed path which form two interferometers are shown as thick lines.

Only two trajectories which form closed paths lead to interference. The effect of a traveling wave acting as a beam splitter can be simply understood by using the mechanical interpretation [Ste 92a].

Atoms in the ground state with momentum $\mathbf{p}$ absorb a photon with energy $\hbar\omega_L$. Energy and momentum conservation is given by

$$\frac{p^2}{2M} + \hbar\omega_L = \frac{(p + \hbar k)^2}{2M} + \hbar\omega_0 \;,\; |k| = \frac{\omega_L}{c} \tag{3.1}$$

where ω_0 is the atomic eigenfrequency, M is the atomic mass and $\mathbf{k}$ is the propagation wave vector of the laser beam. Equation 3.1 can be simplified to

$$\frac{k \cdot p}{M} = \Delta - \delta \tag{3.2}$$

where $\Delta=\omega_0-\omega_L$ is the laser detuning, $\delta=\hbar k^2/2M$ is the single photon recoil shift. Equation 3.2 just shows the resonance condition for the Doppler shift compensating the detuning and the photon recoil energy. When $\Delta \neq \delta$ the excited state wave packet does not only pick up momentum in the z direction (transverse) but also along the atomic beam direction (longitudinal). The longitudinal momentum transfer follows from the Heisenberg uncertainty principle for the localized laser beam waist and the spread in **k**. This results in both transverse and longitudinal displacement of the excited state partial wave (see Fig. 3.2). The transverse displacement will be compensated after the four interaction zone. In contrast, the longitudinal displacement gives rise to a phase difference between the two partial waves after the four interaction zones :

Fig. 3.2: Traveling light wave as an atomic beam splitter.

$$d\Phi \; = \; 2\pi \; \frac{dx}{\lambda_{DB}} \tag{3.3}$$

where

$$dx \; = \; 2T \; \frac{\hbar(\Delta-\delta)}{p_x} \; , \; \lambda_{DB}=\frac{h}{p_x} \tag{3.4}$$

The time $T =D/v_x$ denotes the transit time through the first and third dark zone. The detuning dependent phase difference leads to a periodic Ramsey fringe for the excitation probability :

$$P \; \propto \; \cos(d\Phi) \; = \; \cos[2T(\Delta-\delta)] \tag{3.5}$$

A similar argument applies to atoms initially in the ground state with momentum **p**-ℏ**k**. After interacting with the four laser beams these will also form a closed path. The periodic interference fringe is of the form

$$P \; \propto \; \cos(d\Phi) \; = \; \cos[2T(\Delta+\delta)] \tag{3.6}$$

53

The above two terms correspond to the usual blue and red recoil components of the interferometer as shown in Fig. 3.1 for the bottom and upper closed path.

For atomic beams the time T depends on the longitudinal velocity of the atoms. The velocity distribution is usually very broad and only a few fringes will be observed when the total excitation probability $P = P_+ + P_-$ is integrated over the velocity distributions. From another point of view, the broad velocity distribution implies short de Broglie wave coherence length (some λ_{DB}). Since only longitudinal displacement smaller than the coherence length will contribute to the visible fringes only few fringes are visible.

In the atomic reference frame the four zone RBI geometry looks like two pairs of counterpropagating pulses. This is equivalent to a pulsed RBI in an atomic trap as shown in Fig. 3.3. The difference is that the energy conservation is no more fulfilled. The energy

Fig. 3.3: Scheme for pulsed RBI in the trap.

uncertainty of the laser pulse provides the energy difference between the laser frequency $\hbar\omega_L$ and the atomic internal energy. The four pulses will still spilt and recombine the atomic wave packet.The phase difference between the two partial waves is now better be calculated with the path integral described in section 3.3. The interference pattern has still the same form as that derived above. But now the dark interval T is only determined by the pulse separation and independent of the atomic longitudinal velocity distribution. As a consequence more fringes appear.

The above treatment does not consider the phase change of the atomic coherence in each interaction zone. This effect will be discussed in the next section in the frame work of a quantum mechanical treatment.

3.2 Quantum theory of Ramsey-Bordé interferometry

For a derivation of the Ramsey fringes, the time dependent Schrödinger equation must be solved. The atom-field interaction for a two-level atom is described in the electric dipole approximation by the Hamiltonian [All 75]

$$\hat{H} = \frac{\hat{p}^2}{2m} + \hbar\omega_0 |e\rangle\langle e| - \boldsymbol{d}\cdot\boldsymbol{E} + i\frac{\Gamma}{2} \tag{3.7}$$

54

where $\hat{p}$ denotes the momentum operator and Γ is the decay rate of the excited state. The electric dipole coupling term $H_{int}=-\mathbf{d}\cdot\mathbf{E}$ describes the interaction between the atomic dipolement $\mathbf{d}$ and the electric field $\mathbf{E}(r,t)$. The interaction of the atom with a running wave will be considered, i.e. with an electric field given by : $\mathbf{E}(r,t)=\mathbf{E}_0(r)/2\cdot\exp[i(kz-\omega_L t+\varphi)]+c.c.$. The term $e^{\pm ikz}$ in the field operator changes the atomic external state from $|\mathbf{p}>$ to $|\mathbf{p}\pm\hbar\mathbf{k}>$ which corresponds to absorption and emission of a photon with momentum $\hbar\mathbf{k}$.

The time evolution of the atomic state $|\Psi(r,t)>$ is governed by the Schrödinger equation:

$$i\hbar\frac{\partial}{\partial t}|\Psi(r,t)> \;=\; \hat{H}|\Psi(r,t)> \tag{3.8}$$

To solve this equation a suitable basis has to be chosen. Since the momentum transfer between photon and atom reaction should be considered it is convenient to use the product space from internal and the momentum states with the basis : $\{|g, \mathbf{p}+m\hbar\mathbf{k}>, |e, \mathbf{p}+(m\pm1)\hbar\mathbf{k}>\}$, where m is a integer. In the rotating wave approximation the Schrödinger equation can then be simplified to a $2\otimes2$ matrix equation [Bor 84]:

$$\frac{\partial}{\partial t}\begin{pmatrix} e_{m\pm1} \\ g_m \end{pmatrix} = \begin{pmatrix} -i\omega_0+(m\pm1)\delta-i\dfrac{\Gamma}{2} & 0 \\ 0 & -im^2\delta \end{pmatrix}$$
$$+ \begin{pmatrix} 0 & \dfrac{\Omega_0(r)}{2}e^{-i(\omega_L t\mp kz\mp kv_z t+\varphi)} \\ \dfrac{\Omega_0(r)}{2}e^{i(\omega_L t\mp kz\mp kv_z t+\varphi)} & 0 \end{pmatrix}\begin{pmatrix} e_{m\pm1} \\ g_m \end{pmatrix} \tag{3.9}$$

where $\Omega_0(r)=<e|\mathbf{d}\cdot\mathbf{E}(r)|g>/\hbar$ is the Rabi frequency.

When transformed to another basis with the unitary transformation

$$
\begin{pmatrix} \tilde{e}_{m\pm1} \\ \tilde{g}_m \end{pmatrix} = \begin{pmatrix} e^{i\frac{(\omega_0+\omega_L)t-2(m\pm1)(kz+kv_zt)}{2}} & 0 \\ 0 & e^{i\frac{(\omega_0-\omega_L)t-2m(kz+kv_zt)}{2}} \end{pmatrix} \begin{pmatrix} e_{m\pm1} \\ g_m \end{pmatrix} \tag{3.10}
$$

the Hamiltonian will be independent of space and time. The Schrödinger equation is then simplified to

$$
\frac{\partial}{\partial t}\begin{pmatrix} \tilde{e}_{m\pm1} \\ \tilde{g}_m \end{pmatrix} = \begin{pmatrix} i\dfrac{\Delta}{2}-i(m\pm1)^2\delta-i(m\pm1)kv_z-\dfrac{\Gamma}{2} & \dfrac{\Omega_0(r,t)}{2}e^{-i\varphi} \\ \dfrac{\Omega_0(r,t)}{2}e^{i\varphi} & -i\dfrac{\Delta}{2}-im^2\delta-imkv_z-\dfrac{\Gamma}{2} \end{pmatrix}\begin{pmatrix} \tilde{e}_{m\pm1} \\ \tilde{g}_m \end{pmatrix} \tag{3.11}
$$

This equation can not be solved analytical unless the Rabi frequency is constant. For constant Rabi frequency it is shown that the evolution of the atomic state can be simplified to

$$
\begin{pmatrix} \tilde{e}_{m\pm1}(t+\tau) \\ \tilde{g}_m(t+\tau) \end{pmatrix} = \exp(\frac{i}{2}\Omega_d\sigma_0(\tau))\begin{pmatrix} A & Be^{-i\varphi^\pm} \\ Ce^{i\varphi^\pm} & D \end{pmatrix}\begin{pmatrix} \tilde{e}_{m\pm1}(t) \\ \tilde{g}_m(t) \end{pmatrix} \tag{3.12}
$$

where

$$
\begin{aligned}
A &= D^* = \cos(\frac{\Omega\tau}{2})+i\frac{\Delta_{v\delta}}{\Omega}\sin(\frac{\Omega\tau}{2}) \\
B &= C = i\frac{\Omega_0}{\Omega}\sin(\frac{\Omega\tau}{2}) \\
\Delta_{v\delta} &= \Delta\mp kv_z-[(m\pm1)^2-m^2]\delta+i\frac{\Gamma}{2} \\
\Omega_d &= -[(m\pm1)^2+m^2]\delta-(2m\pm1)kv_z+i\frac{\Gamma}{2} \\
\Omega &= \sqrt{\Omega_0^2+\Delta_{v\delta}^2}
\end{aligned} \tag{3.13}
$$

The wave function of an atom starting in the ground state after interacting with a traveling wave is then given by

56

$$|\Psi> = \frac{\Omega_0}{\Omega}\sin\frac{\Omega\tau}{2}e^{\,i(\pi/2-\varphi)}|e,\ \boldsymbol{p}+\hbar\boldsymbol{k}> + \sqrt{(\cos^2\frac{\Omega\tau}{2}+\frac{\Delta_{v\delta}^2}{\Omega^2}\sin^2\frac{\Omega\tau}{2})}\ e^{\,-i\theta}|g,\ \boldsymbol{p}> \qquad (3.14)$$

where $\theta=\arctan[\Delta_{v\delta}/\Omega\cdot\tan(\Omega\tau/2)]$.

The excited state population is equal to $\Omega_0^2/\Omega^2\cdot\sin^2(\Omega\tau/2)$, which is the well-known Rabi oscillation. For a $\Omega\tau=\pi/2$ pulse, the atom will be in the excited state with 50% probability when the light field is on resonance, i.e. $\Delta_{v\delta}=0$. This corresponds to a 50% beam splitter. A mirror can then be realized with a π pulse. Not only the phase of the laser affects the phase difference at the exit port, but also an additional phase θ. This phase θ has usually been neglected in the literature, but it has important consequences for the RBI experiments and will be discussed in more detail later.

In the dark region the atoms propagate freely and the transfer matrix is

$$\begin{pmatrix} e^{\frac{i}{2}(\Omega_d+\Delta_{v\delta})T} & 0 \\[2mm] 0 & e^{\frac{i}{2}(\Omega_d-\Delta_{v\delta})T} \end{pmatrix}$$

The interaction of the atom with the four traveling waves can be treated as the product of the interaction matrix and the free propagation matrix. The final probability of atoms in the excited state $|e_{-1},-1>$ and $|e_{+1},+1>$ can thus be written as

$$
\begin{aligned}
e_{-1}e_{-1}^{*} \ = \ & e^{-\Gamma(T+2\tau)}\{[|B_1C_2B_3A_4|^2e^{-\Gamma T}+|B_1C_2D_3B_4|^2+|D_1D_2B_3A_4|^2+|D_1D_2D_3B_4|^2e^{\Gamma T} \\
& +[B_1C_2B_3A_4(D_1D_2D_3B_4)^{*}e^{\,i(\Delta-\delta)2T}e^{\,\varphi_2-\varphi_1+\varphi_4-\varphi_3}+c.c.]\} \\
& +O(e^{\pm ikv_z})
\end{aligned}
\qquad (3.15)
$$

$$
\begin{aligned}
e_{+1}e_{+1}^{*} \ = \ & e^{-\Gamma(T+T'+2\tau)}\{[|B_1A_2A_3A_4|^2e^{-\Gamma T}+|B_1A_2C_3B_4|^2+|D_1B_2A_3A_4|^2+|D_1B_2C_3B_4|^2e^{\Gamma T} \\
& +[B_1A_2A_3A_4(D_1B_2C_3B_4)^{*}e^{\,i(\Delta+\delta)2T}e^{\,\varphi_2-\varphi_1+\varphi_4-\varphi_3}+c.c.]\} \\
& +O(e^{\pm ikv_z})
\end{aligned}
\qquad (3.16)
$$

The final total excitation probability is the sum of the above two terms integrated over the velocity distribution N(v).

$$P = \int_{-\infty}^{\infty} (e_{-1} e_{-1}^* + e_{+1} e_{+1}^*) N(v) d^3 v \qquad (3.17)$$

The terms proportional to $e^{\pm ikv}$ oscillate very fast with v_z and can be neglected when integrated over v_z. The oscillating terms $\exp[2i(\Delta+\delta)T]$ and $\exp[2i(\Delta-\delta)T]$ correspond to the red and blue component of the interference fringes. The other terms contribute to the incoherent Doppler background and saturation dip.
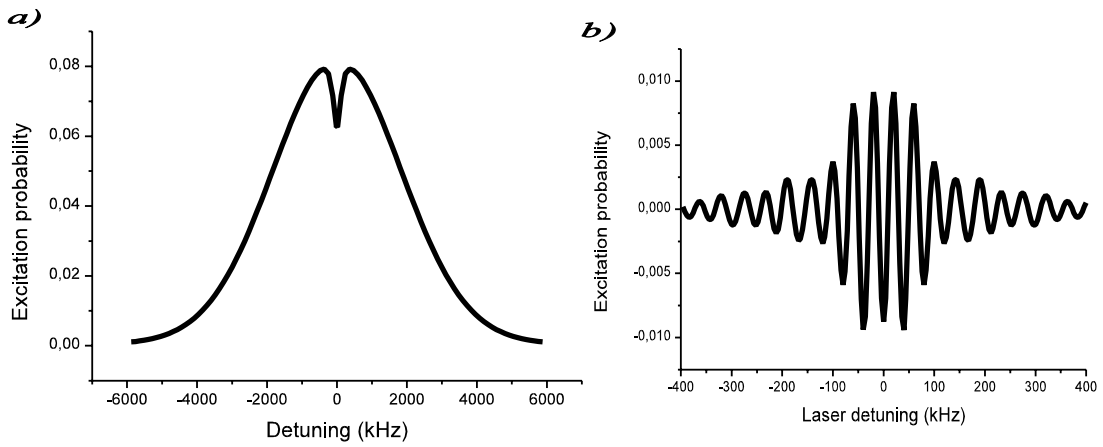
Fig. 3.4 The calculated excitation probability a.) the Doppler and Lamb dip background b.) the oscillation part of eq.3.17 for τ=4 µs, T=7.6 µs, Ω_0=87 kHz

Fig 3.4 shows the calculated excitation probability of the incoherent background and the interference terms for τ=4 µs, T=7.6 µs and Ω_0=87 kHz. The velocity distribution has been chosen as a Gaussian distribution with width equal to 0.83 m/s which is equivalent to Doppler temperature. Remarkably the period of the fringe is not 1/2T which is the period of the signal $\cos[(\Delta-\delta)2T]+\cos[(\Delta+\delta)2T]$. This is due to the phase θ mentioned before. To see its effect the coefficient of $\exp(i(\Delta\pm\delta)2T)$ must be considered. It can be shown that the coefficient $B_1 C_2 B_3 A_4 (D_1 D_2 D_3 B_4)^*$ of $\exp[2i(\Delta-\delta)T]$ can be expressed as $a_{re} \cdot \exp[2i(\theta_1+\theta_2)]$ where a_{re} is a real number and $\theta_j = \arctan[\Delta_{v\delta}/\Omega \tan(\Omega \tau/2)]$, with $\Delta_{v\delta}=\Delta\pm kv-\delta$ where + is for j=1 and - for j=2. If $\Omega \tau << 1$ then $\theta_j \approx \Delta_{v\delta} \tau/2$ and

$$\exp[2i(\theta_1+\theta_2)] \approx \exp[i(\Delta-\delta)2\tau]. \qquad (3.18)$$

58

So there is a contribution of an additional phase factor $\exp[i(\Delta-\delta)2\tau]$ during the finite interaction time. The fringe of the red component should be of the form $\exp[i((\Delta-\delta)2(T+\tau)]$ for $\Omega \tau \ll 1$. A similar argument applies for the blue component where the oscillation term has the form $\exp[i((\Delta+\delta)2(T+\tau)]$ for $\Omega \tau \ll 1$. In this case the period of the fringe is $1/2T_p$, where $T_p = T+\tau$ is defined as the effective pulse separation. Therefore the terms $B_1 C_2 B_3 A_4 (D_1 D_2 D_3 B_4)^*$ and $B_1 A_2 A_3 A_4 (D_1 B_2 C_3 B_4)^*$ do not only affect the fringe envelope but also its periodicity. They contain the phase difference of the two partial waves in the interferometer introduced by the atom-field interaction during the four interaction zones. This property has been neglected by Bordé. Its influence on the fringe periodicity has also been discussed by J. Müller [Mül 94].

Another interesting case is the $\Omega \tau = \pi/2$ pulse scheme.

If $\Delta_{v\delta}\tau \ll 1$ then $\theta_i \approx \Omega_D 2\tau/\pi$ and

$$\exp[2i(\theta_1+\theta_2)] \approx \exp[i(\Delta-\delta)2\tau\cdot 4/\pi]. \tag{3.19}$$

The corresponding fringe periodicity is $1/2T_p$ with $T_p = T+4\tau/\pi$. Here the fringe periodicity depends also on the strength of the coupling between the atom and the laser. The additional time τ in the fringe period does not affect the fringe amplitude for the atomic beam experiment since the fringes of the two recoil components after velocity averaging do not overlap. However, for pulsed RBI in a trap the two fringes will overlap as mentioned before. Since $\cos[(\Delta-\delta)2T_p]+\cos[(\Delta+\delta)2T_p]=1/2 \cos(2T_p\Delta) \cos(2T_p\delta)$, the effective pulse separation T_p will also affect the fringe amplitude. The fringe is maximum when $T_p=n\pi/2\delta$ (multiple of 6.3 µs for Mg) where n is an integer and δ is the recoil shift in terms of angular frequency. The fringes superpose constructively when the fringe periodicity is an integer fraction of the recoil separation. The correct effective pulse separation should be chosen during the experiment in order to get the maximum fringe amplitude.

When the pulse separation deviates from the maximum value it affects not only the fringe amplitude but also shifts the position of the two recoil components. For pulsed RBI in a trap the frequency pulling due to the deviation dT_p from the optimum value is

$$d\omega_{fp}=\delta\frac{dT_p}{T_p} \tag{3.20}$$

To reduce the pulling below 1 Hz, the relative error of the effective pulse separation has to be less than $2.5 \cdot 10^{-5.}$ Because of the dependence of the effective pulse separation T_p on the atom-field coupling the exact maximum T_p is not easily determined experimentally. Suppressing one of the recoil components will be necessary when the RBI is used in the application of an optical frequency standard. This can be done by turning on shortly the trapping laser between the 2nd and 3rd spectroscopic pulse. A similar method has already been realized in the thermal atomic beam interferometer [Sen 93]. There are also other methods that can suppress one of the recoil component. Detailed discussions can be found in [Bor 77, Hel 87, Din 94].

There are many other factors that will shift the position of the fringes. These will be discussed in the next section.

3.3 Influence of additional potentials

In comparison with other types of interferometers using photons, electrons or neutrons, atom interferometers give rise to interesting new investigations due to the variety of internal degrees of freedom. Any potentials that affect the internal state will influence the phase between the two arms of the interferometer and hence can be precisely measured. On the one hand this opens new ways to study atomic properties. On the other hand it requires a careful analysis of any external influence which potentially affects the interference in view of high precision spectroscopy.

The phase induced by small additional potentials in interferometer can be suitably studied by Feynman's path integral method [Fey 65]. Feynman's method treats the evolution of the state of a quantum system in terms of a quantum propagator $G(r_b,t_b;r_a,t_a)$. The knowledge of the propagator enables us to determine the time development of the wavefunction.

$$\Psi(r_b,t_b) = \int G(r_b,t_b;r_a,t_a) \ \Psi(r_b,t_b) \ dr_a \qquad (3.21)$$

This quantum propagator can be written as the sum of contributions from all possible paths connecting the initial (r_a,t_a) and final (r_b,t_b) points.

$$G(r_b,t_b;r_a,t_a) = \sum_\Gamma e^{iS_\Gamma/\hbar} \qquad (3.22)$$

Each path contributes a phase factor $S_\Gamma/\hbar$, where S_Γ is the action along the path Γ and the

modules of the contribution is path independent.

In the classical limit $S_\Gamma \gg \hbar$, the phase $S_\Gamma/\hbar$ varies very rapidly between neighboring paths Γ_i, and cause destructive interference. Only the path neighboring the classical path Γ_{cl} where the action is extremal will contribute constructively. If the Lagrangian is quadratic in position and velocity Storey et al. [Sto 94a] have shown that the phase of the final wave function can simply be determined by the action along this classical path and the phase of the initial state:

$$\Psi(r_b,t_b) \;=\; F(t_b,t_a)\; e^{\frac{i}{\hbar}S_{\Gamma_{cl}}(r_b,t_b;r_a,t_a)}\; \Psi(r_a,t_a) \tag{3.23}$$

where $F(t_b,t_a)$ is a modules independent of r_a and r_b. The action $S_{cl}(r_b,t_b;r_a,t_a)$ is the integral of the Lagrangian $L(\boldsymbol{r},\,\dot{\boldsymbol{r}})$ over the classical path Γ_{cl}

$$S_{cl}(r_b,t_b;r_a,t_b) \;=\; \int_{t_a}^{t_b} L(\boldsymbol{r}(t),\,\dot{\boldsymbol{r}}(t))\; dt \;=\; \int_{\Gamma_{cl}} \boldsymbol{p}\cdot d\boldsymbol{r} - H dt \tag{3.24}$$

where H is the classical Hamiltonian.

For small additional potentials, it can be treated as a perturbation of the normal interferometer. The phase shift introduced by the perturbation can then be obtained by integrating the perturbation along the unperturbed path Γ_0.

$$d\varphi \;=\; \frac{1}{\hbar}\int_{\Gamma_0} \boldsymbol{p}\cdot d\boldsymbol{r} - H dt \tag{3.25}$$

When the additional potential is independent of time the Hamiltonian H is just the total energy E and the momentum is $p=\sqrt{2M(E-V(r))}$. The phase shift due to such a weak potential $V \ll E$ is then

$$d\varphi \;=\; \frac{1}{\hbar}\int_{\Gamma_0} \boldsymbol{p}\cdot d\boldsymbol{r} \;\approx\; -\frac{1}{\hbar v}\int_{\Gamma_0} V(r)\cdot d\boldsymbol{r} \tag{3.26}$$

In the pulsed RBI the additional potentials are usually only time dependent and the phase shift introduced by such a time dependent potential is only the time integral of the potential along the path :

61

$$d\varphi \; = \; -\frac{1}{\hbar} \int_{\Gamma_0} V(t) \cdot dt \qquad\qquad (3.27)$$

In the past few years additional potentials acting on an atomic interferometer have been extensively studied. These include AC, DC Stark effect, pure quantum mechanical topological phases like Aharonov-Bohm effect and Aharonov-Casher effect and the inertial forces like gravitation and rotation (Sagnac effect). An overview of these measurements can be found in [Ste 97, You 97]. Some of these effects in the Mg RBI experiment will be summarized in chapter 5.3 with respect to optical frequency standards.

Chapter 4

Pulsed Ramsey-Bordé interferometry in a Mg Magneto-Optical Trap

The RBI with a thermal the Mg atomic beam has been subject of numerous studies in the group of Prof. Ertmer. The resolution of the Ramsey fringes in the atomic beam RBI is limited by the zone separation through T= D/v. This distance is currently limited by the size of the window for the four traveling beams. With a maximum of D= 30 mm the best linewidth is 5 kHz. Another crucial limit is the line shift due to the 2nd order Doppler effect. For a velocity of the atomic beam of 700 m/s the 2nd order Doppler shift is already 300 Hz. Furthermore the 2nd order Doppler effect also causes power dependent shifts and asymmetries in the Ramsey fringes [Bar 81]. Reducing the velocity of the atoms is the only way to eliminate such an effect. It can be done either by optical selection of cold atoms in a gas [Bag 91] or by actively cooling the atoms. The cooling and trapping techniques described before serve this purpose. The RBI within the Mg trap has also been studied in this group [Sen 93, Ste 93, Mül 94]. New results based on a well improved spectrometer and trapping system will be presented in this chapter.

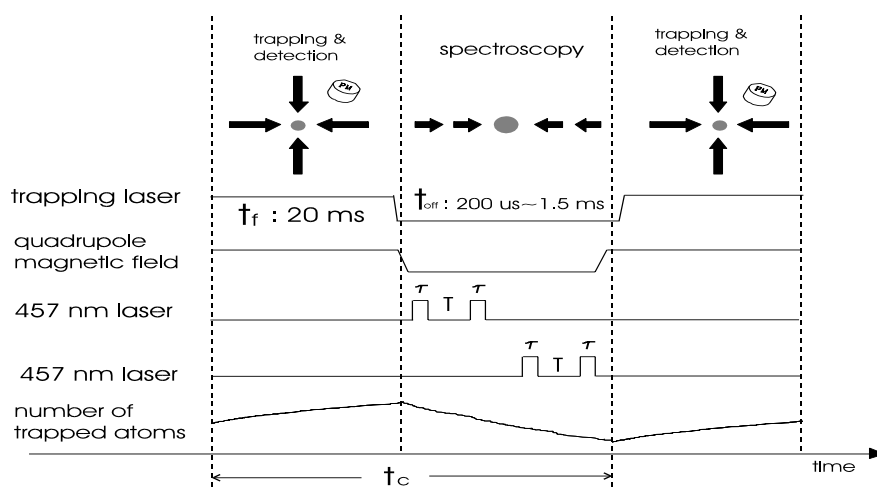## 4.1 Methods of pulsed RBI in the trap

Fig.4.1: Timing schedule for the pulsed RBI in the trap.

To realize RBI in a trap disturbances must be removed during the spectroscopy time. The trap

is operated in pulsed mode as described in section 2.5. The principle time schedule for the spectroscopy is shown in Fig. 4.1.

The trapping laser and quadrupole magnetic field will first be turned off. Three pairs of Helmholtz coils are used to compensate the stray magnetic fields such that there is only a magnetic field in the vertical direction when the quadruple magnetic field is turned off. This bias field is used to define the quantization axis and shifts the $\Delta m = \pm 1$ components out of resonance. Therefore, only the $\Delta m = 0$ component will contribute to the interaction. The duration of the trapping laser off-time t_{off} depends on spectroscopy time. In this experiment it will be smaller than 1.5 ms. After turning off the trapping laser about 50 µs later, the two pairs of Ramsey pulses are sent to the trap. The separation the each pulse pair determines the resolution of the fringes.

Since the life time of the Mg $^3P_1$ state is long, it is not very efficient to detect its fluorescence directly. For alkali earth elements the ground state is a common state of a fast transition and the metastable transition. The fluorescence of the fast transition will be interrupted when the atom is excited to the metastable state. Such quantum jumps due to electron shelving was first proposed by Dehmelt [Dem 75] for the case of 'atomic amplifier' to detect transitions between very stable states. In an ensemble of atoms the quantum jumps of single atoms will not directly be observed. However this effect can still be used to effectively detect small excitations of the metastable state. Therefore, instead of detecting the fluorescence of the metastable state the fluorescence of the trapped atoms is detected. This is done by turning on the trapping laser again for a time duration of t_f after the spectroscopy time. The fluorescence from the trap can then be detected with a photomultiplier or a photodiode . Atoms in the excited $^3P_1$ state leave the trap and do not contribute signal. This results in a reduction of the trap fluorescence. After turning on the trapping laser beam the expanded atom cloud will be recompressed to the normal trap size within a few hundred µs as mentioned in section 2.5. These recycled atoms together with the newly trapped atoms can be used for next cycle of spectroscopy. Such a repeat of spectroscopy will result an amplified trap loss due to the spectroscopy and also enhance the signal-to-noise ratio. This amplification effect will be discussed more detail in the next section. Typically 50 cycles will be repeated for each frequency point. By scanning the laser frequency and repeating the procedure the measured spectrum shows the typical Ramsey fringes.

4.2 Quantum amplification detection mechanism

The use of the electron shelving effect in the detection of RBI signals was first introduced by K. Sengstock [Sen. 93]. This method is still used in present work and will be studied in more detail. In particular the recapture of the excited $^3p_1$ state atoms will be considered since our new trap has a larger trap region than before.

Consider the time schedule of Fig. 4.1 neglecting the trapping laser off-time. Let t_i be the time just before the ith spectroscopy cycle. Then the number of trapped atoms at any time t between t_i and t_{i+1} should be described by the equation

$$N(t)=N_s+[N(t_i)\ (1-\alpha_e-\alpha(\Delta))-N_s]e^{-t/\tau_{tr}}+N(t_i)\alpha(\Delta)(1-e^{-t/\tau_{3P1}})p_r \qquad (4.1)$$

The first two terms on the right hand side are similar to eq. 2.19 but with an additional initial loss $\alpha(\Delta)$ resulting from the spectroscopy. The third term comes from the recapture of the atoms which decayed from the excited state after the spectroscopy. It is equal to the product of the initially excited atoms $N(t_i)\ \alpha(\Delta)$, the recapture probability p_r and the decay probability $1-\exp[t/\tau_{3P1}]$. The time evolution of the number of trapped atoms according to eq. 4.1 is shown in Fig. 4.2 for various recapture probabilities.

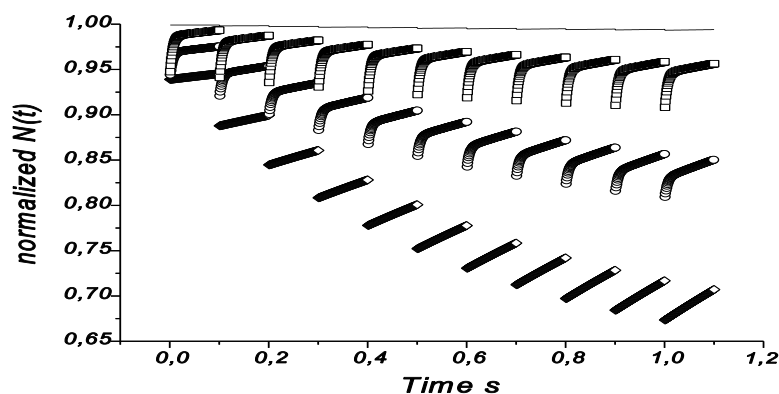Fig. 4.2: Time development of the number of trapped atoms for various of recapture probability p_r . Solid line: pure pulsed trap, Square: p_r =80%,Circle: p_r= 50%, Diamond: p_r= 0

The trap has an effective trap region of R_{tr} =3 mm and a lifetime of τ_{tr}=0.9 s. For a trapping laser off-time of 1 ms the effusive loss rate is α_e=0.001. The solid line shows the evolution of

the pulsed trap without spectroscopic excitation. The evaluation of the pulsed trap with additional spectroscopic excitation probability α(Δ)=0.06 and various recapture probabilities is also shown. It is obvious that the recapture probability has a significant influence on the additional spectroscopy loss..

A simple model will help to estimate the recapture probability. It is assumed that the trap depth is much larger than the trap itself. This is approximately true for our experiment. For longer off-time the trap expands to a larger size and the recapture rate is expected to be smaller. The atoms are recaptured when they decay to the ground state within the trap region R_{tr} . The time t for atoms in the $^3P_1$ excited state with velocity v to travel from the trap center to R_{tr} is t= R_{tr}/v. The probability γ that the excited atoms decay to the ground state just obeys the exponential decay law γ= 1- exp[-t/τ$_{3p1}$] where τ$_{3p1}$ is the natural lifetime of the excited $^3P_1$ state. We will consider the recapture probability of each class of atoms with longitudinal velocity v_z (along the laser pulse direction) which can be excited by a laser with detuning Δ. The decay probability of such a class of atoms can be expressed as

$$\gamma(v_z) \;=\; 1-e^{-t/\tau_{3PI}} \;=\; 1-e^{-\dfrac{R_{tr}}{\sqrt{v_t^2+v_z^2}\,\tau_{3PI}}} \tag{4.2}$$

where v_t is the transverse velocity component perpendicular to v_z .

The recapture probability for atoms with velocity v_z is then equal to the integration of the product of the velocity distribution of atoms in the transverse direction v_t and the decay probability over v_t , i.e.

$$p_r(v_z) \;=\; \frac{1}{2\pi v_d^2}\int_0^\infty e^{-\dfrac{v_t^2}{2v_d^2}}\left(1-e^{-\dfrac{R_{tr}}{\sqrt{v_r^2+v_z^2}\,\tau_{3PI}}}\right)\,2\pi v_t\,dv_t \tag{4.3}$$

Fig. 4.3 shows the calculated recapture probability p$_r$(v$_z$) as a function of v_z for a trap with the same parameter as the one in Fig. 2.33. The velocity range which contributes to the Ramsey fringes is very narrow and is usually within the Lamb dip width. For a Lamb dip width of 400 kHz the corresponding velocity range of v_z is just 0.2 m/s. The recapture probability for this

velocity range regime is about 47% as shown in Fig. 4.3. This recapture probability can be changed by modifying the trap region R_{tr}. A smaller trap region can reduce the recapture probability but this will increase the effusive loss. For the pulsed RBI the best condition is that both the recapture probability and the effusive loss are small. So there is a
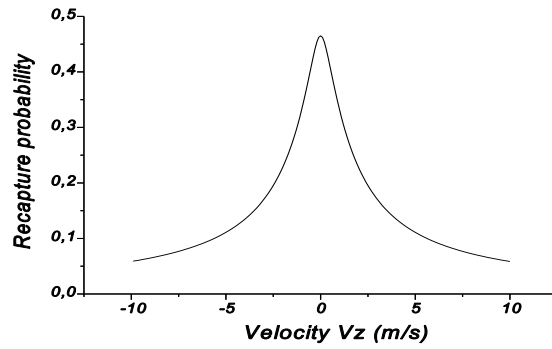
Fig. 4.3. Calculated recapture probability of the excited $^3P_1$ state for a trap with trap region of 3 mm and velocity $\sigma_v=0.95$ m/s

trade off between these two. For a trapping laser off-time of 1 ms the optimum trap region is about 3mm which is the case in this experiment. This will be discussed in more detail in section 4.5.

Equation 4.1 has the similar form as eq. 2.58. There will be a new stationary state for the number of trapped atoms similar to eq. 2.59, i.e.

$$N_{sp} = \frac{N_s}{1 + (\alpha_E + \alpha(\Delta)\, p_L)\, \dfrac{e^{-\frac{t_f}{\tau_{tr}}}}{1 - e^{-\frac{t_f}{\tau_{tr}}}}} \tag{4.4}$$

where p_L is defined as the effective lost probability and is equal to

$$p_L = 1 - p_r(1 - e^{-\frac{t_f}{\tau_{3p1}}})e^{\frac{t_f}{\tau_{tr}}} \tag{4.5}$$

If the trap lifetime τ_{tr} is much larger than t_f eq. 4.4 can be simplified to

$$N_{sp} = \frac{N_s}{1 + (\alpha_e + \alpha_L(\Delta))\, \dfrac{\tau_{tr}}{t_f}} \tag{4.6}$$

where $\alpha_L(\Delta)=\alpha(\Delta) p_L$ is defined as the single cycle spectroscopic loss. The trap loss due to the spectroscopy is then

$$N_p - N_{sp} = \frac{\alpha_L(\Delta) \; \frac{tr}{t_f} \; N_p}{1 + (\alpha_e + \alpha_L(\Delta))\frac{\tau_{tr}}{\cdot}} \qquad (4.7)$$

The lifetime of our trap is 1 to 3 s depending on the intensity of the trapping laser and the trapping time t_f is about 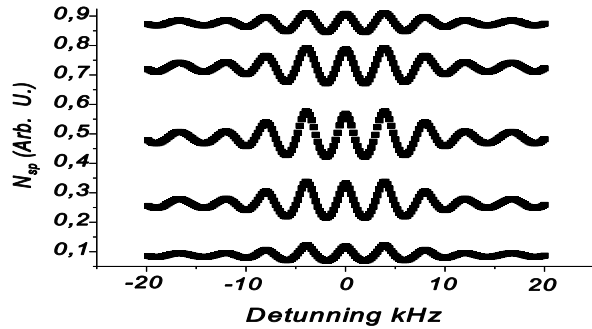20 ms. Under these experimental conditions eq. 4.5 can be approximated as $p_L \approx 1-p_r$. The excitation probability $\alpha(\Delta)$ for one cycle is about 1 to 5%. The trap loss due to spectroscopy can then be 20% to 70% for a trap region of 3 mm. This shows clearly the amplification of the trap loss with such a spectroscopic scheme. Since within the lifetime we perform τ_{tr}/t_f cycles the accumulated trap loss shows such amplification mechanisms. But this does not imply that larger numbers of cycles will result in more amplification of Ramsey fringe amplitude. Substituting the calculated excitation probability shown in Fig. 3.4 into eq. 4.4 we can estimate the pulsed RBI in the trap. Fig. 4.4 shows the calculated N_{sp} as a

Fig. 4.4 Calculated pulsed RBI signal in the trap for various cycling times. The parameter for the pulsed trap is the same as Fig. 2.33. From upper to bottom the cycling time is 0.2, 0.08, 0.03, 0.012 and 0.004 s, respectively. The Lamb dip has been eliminated.

function of the laser detuning for various cycling times t_c. The Lamb dip background has been eliminated. It is seen that the maximum Ramsey fringe amplitude occurs when the averaged number of trapped atoms is half of that of the cw trap. Higher spectroscopic rates cause more trap loss and reduced the fringe amplitude. This behavior can be qualitatively understand with the help of eq. 4.7 which shows that the detected loss is not linear to $1/t_f$. It will saturate at a high rate of spectroscopic cycles. Such a nonlinearity makes the fringe amplitude smaller when spectroscopic rate is large. Quantitatively the fringe amplitude can be determined as follows. For $\tau_{tr} \gg t_f$ the fringe amplitude can be calculated according to eq. 4.6 by

$$N_{sp}(\alpha(\Delta_1)) - N_{sp}(\alpha(\Delta_2)) \ = \ \frac{(\alpha_L(\Delta_1) - \alpha_L(\Delta_2))\dfrac{\tau_{tr}}{t_f} N_s}{(1 + (\alpha_e + \alpha_L(\Delta_1))\dfrac{\tau_{tr}}{t_f}) \ (1 + (\alpha_e + \alpha_L(\Delta_2))\dfrac{\tau_{tr}}{t_f})} \tag{4.8}$$

where $\alpha(\Delta_1)$ and $\alpha(\Delta_2)$ correspond to the maximum and minimum excitation probability for the Ramsey fringe near the center of the Lamb dip.

Fig. 4.5 shows the calculated fringe amplitude as a function of the cycling time according to eq. 4.8 for a trapping laser off-time of 1 ms for different trap lifetime and trap region. As can be inferred from Fig. 4.5 for longer trap lifetime or smaller trap region the optimum cycling time is larger. For cycling times shorter than the optimum value the fringe amplitude will drop rapidly. Experimentally, this region should be avoided.
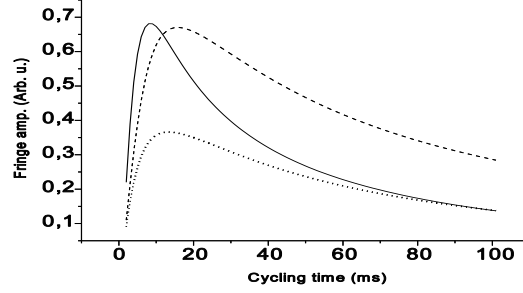
Fig. 4.5 The dependence of Ramsey fringe on cycling time for various parameters. Solid: τ_{tr}=0.9 s, R_{tr}=3 mm, Dash: τ_{tr}=2 s, R_{tr}=3 mm, Dot: τ_{tr}=3 s, R_{tr}=2.5 mm

In principle eq. 4.4 is stationary after an infinite number of spectroscopy cycles. Of course there is just a number of cycles in the experiment. The number of cycles n required for the signal to deviate ξ from the stationary state can be calculate from the criterion $N_{sp} - N_{sp}(t_n) \geq \xi \, N_{sp}$. This leads to

$$n \geq \frac{\ln[\dfrac{\xi}{\alpha_E + \alpha_L(\Delta)}(e^{\frac{t_f}{\tau_{tr}}} - 1)]}{\ln[(1 - \alpha_E - \alpha_L(\Delta))e^{-\frac{t_f}{\tau_{tr}}}]} \tag{4.9}$$

There should be enough cycles for each frequency point to be scanned. Otherwise the fringe amplitude is reduced. The dependence of number of cycles on the deviation from stationary state and the cycling time for a trapping laser off-time of 1 ms is shown in Fig. 4.6. For a typical

experimental cycling time t_c= 20 ms the number of trapped atoms can reach 90 % of the stationary state after 50 cycles already.

The discussion in this section has shown that with the detection scheme described above even small excitation rates of the $^3P_1$ state can efficiently be detected. Therefore, high resolution spectroscopy

Fig. 4.6: The number of cycles as a function of ξ and t_c according to eq. 4.9.

can be implemented with this method. The application of this method in the experiment and the results will be described in the successive sections.
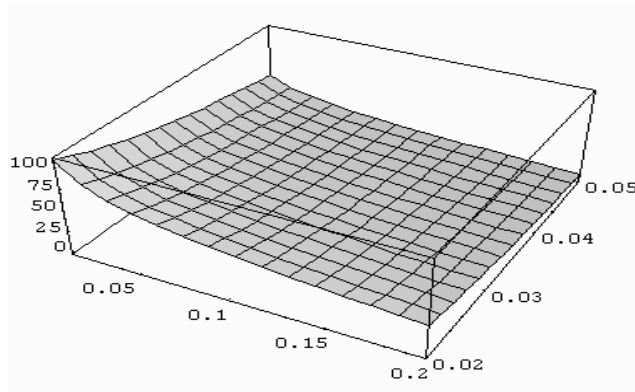
4.3 Experimental setup for RBI in a Mg magneto-optical trap

The laser spectrometer

High stability and a narrow band tuneable laser are essential for high precision Ramsey-Bordé interferometry. The current laser system has been described in detail in the thesis of U. Sterr [Ste. 93] and modified by V. Rieger [Rie 96]. It will briefly be summarized here.
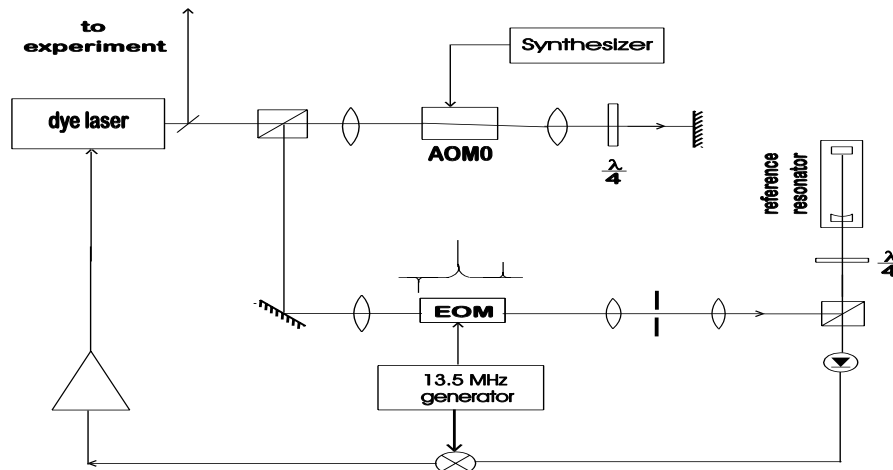
Fig. 4.7 Schematic setup of the 457nm dye laser spectrometer. The laser frequency can be varied by controlling the modulation frequency of AOM0.

The spectrometer consists of a home built ring dye laser frequency stabilized to a high finesse reference resonator by the Pound-Drever-Hall (PDH) method [Pou 83] as shown in Fig. 4.7. The resonator is made of Zerodur ($\Delta l/l = 5 \ 10^{-8}$/K) and has a free spectral range of 289 MHz. With two high reflective mirrors (R=99.9%) the resonator has a finesse of F=42000. This gives a linewidth of the resonator of 7kHz. The resonator is suspended inside an evacuated cavity which is temperature stabilized. In order to tune the laser frequency part of the laser beam double passes an AOM. This beam frequency modulated at 13.5 MHz with an EOM produces the necessary side band for the servo loop. The reflected signal from the resonator is frequency demodulated to get the dispersive servo signal of the PDH method. The low frequency part of the signal drives the PZT of the laser cavity and the high frequency part is fed to the EOM inside the laser cavity. The line width of the stabilized laser can be derived from the error signal of the regular signal which has been determined to be 40 mHz. The residual drift of the stabilized laser due to the thermal drift of the reference cavity is determined to be 30 Hz/(s·mK).

71

Long term stabilization of the spectrometer

For short term the laser will be frequency stabilized to the reference resonator. As mentioned above there is still thermal drift of the reference resonator, so for long term the laser will be frequency stabilized on one of the recoil components of the four zone RBI in the thermal atomic beam. At the same time the pulsed RBI will be performed in the trap. This can be done with 3 tunable AOMs. The complete setup is shown Fig. 4.8.
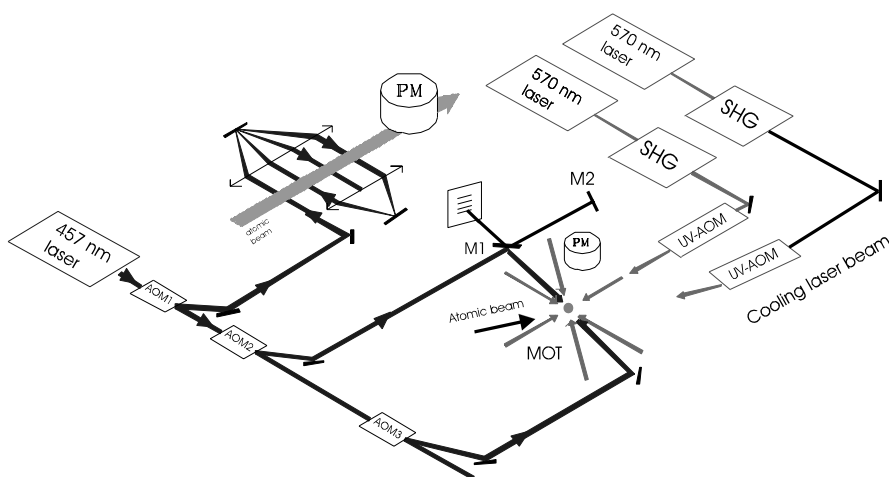
Fig. 4.8: Schematic setup for the pulsed Ramsey-Bordé Interferometry

The frequency stabilized laser beam first passes the AOM1. The -1st order of the laser beam is sent to the atomic beam apparatus for the four zone RBI. Two cat eyes collimate the four parallel laser beams. After interacting with the four traveling light wave the atomic beam fluorescence of the excited state is detected with a PMT. To stabilize the laser frequency one of the recoil component of the Ramsey fringes is chosen. The fringe has a linewidth of 20 kHz as shown in Fig. 4.9. The laser is frequency stabilized to the fringe minimum with the following method.
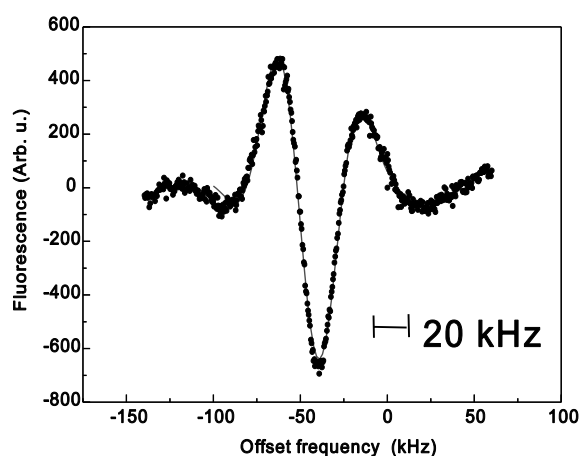
Fig. 4.9: One recoil component of the Ramsey fringes for thermal atomic beam.

First the modulation frequency of AOM1 is fixed at f_m= 80MHz and AOM0 (shown in

72

Fig. 4.7) is frequency modulated such that the signal of the Ramsey fringe is at the minimum of the red recoil component. Now the laser frequency is at the frequency corresponding to the minimum of the red recoil component. Then the laser frequency evolution is determined from the Ramsey signal at two symmetric points on both sides of the minimum. They are $\pm \Delta f_m$ Hz away from the minimum. The signal difference at these two frequency points is used as an error signal to control the modulation frequency of AOM0. If $Sig(f_m+\Delta f_m)-Sig(f_m-\Delta f_m)$ is positive the modulation frequency of AOM0 will be reduced with a step frequency f_{step} and vice verse. This procedure stabilizes the laser frequency to the minimum of the red recoil component. During the experiment Δf_m is fixed to be 8 kHz and the step frequency is kept at 30 Hz. The integration time for each frequency point is 0.5 second. The optimum parameter for f_{step}, Δf_m and other stabilization schemes like using signals at three frequency point to fit to the minimum can be found in [Sch 97].

RBI in the Trap:

The zeroth order of AOM1 is used for the RBI experiment in the trap. The pulsed RBI in the trap is realized by injecting two pairs of counterpropagating laser pulses into the trap. The separation between the first and second pulse and that of the third and fourth pulse is the same. AOM2 and AOM3 produce the required Ramsey pulse pair for forward and backward direction. These two AOMs are placed in the focus of two telescopes respectively, such that there is no laser beam misalignment in the trap when the modulation frequency is varied. The alignment of the forward and backward laser beam is done with the help of an interferometer as shown in Fig. 4.8. The M1 mirror is used as a deflection mirror for the trapping laser beam and also as a beam splitter for the optical interferometer which consists of AOM2, AOM3, M1, M2 and mirrors in-between. The backward laser beam is first adjusted to pass through the trap which can be easily done when the frequency is on resonance with the atomic transition. The transmitted backward laser beam through M1 will then be retroreflected by adjusting M2. This is done by letting the laser beam pass through a small aperture after transmitting M1. Mirror M2 is adjusted such that the retroreflected beam passes the aperture again. Then the forward laser beam is adjusted such that clear interference fringes appears at the output of the optical interferometer. Only when the two laser beams overlap coaxially clear interference appears and confirms the alignment of the two laser beams.

The spectroscopy in the trap will be fulfilled with the procedure described by in section 4.1. The

scanning of the laser frequency is done by modifying the modulation frequency of AOM2 and AOM3. The modulation frequency for these two AOMs are from the same synthesizer to ensure the same frequency for the two pairs of Ramsey pulses. The measured results will be shown in the following section.

4.4 Experimental Results

As mentioned in the last section after turning off the quadrupole magnetic field there is a bias field in the vertical direction to define the quantization axis. The laser polarization is adjusted to be parallel to the magnetic field by monitoring the trap loss. For parallel laser polarization and magnetic field the $\Delta m=0$ transition can be optimally excited and the largest trap loss is the result. The results of a saturation spectroscopy performed with two counterpropagating pulses of width 2.4 μs is shown in Fig. 4.10. The asymmetry of the Lamb dip is
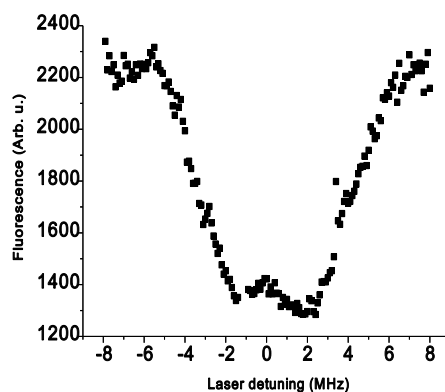
Fig 4.10 Saturation spectroscopy in the trap with pulse width of 2.4 μs.

mainly caused by the laser beam shift when the modulation frequency of AOM is varied remarkably. For the high resolution RBI experiment the frequency variation is only some kHz. In this case the beam displacement is smaller than 1μm and can be neglected. The Doppler profile has a FWHM of 7.8 MHz. From this value the velocity of the trapped atoms is determined to be 1.1 m/s. This value is very close to that derived in section 2.5.

The pulsed RBI in the trap is performed according the method described in section 4.1. For each frequency point the spectroscopy rate is typically 50 Hz and the integration time is 1 s. Fig 4.11 shows such a spectrum of 20 kHz periodicity within the Lamb dip.
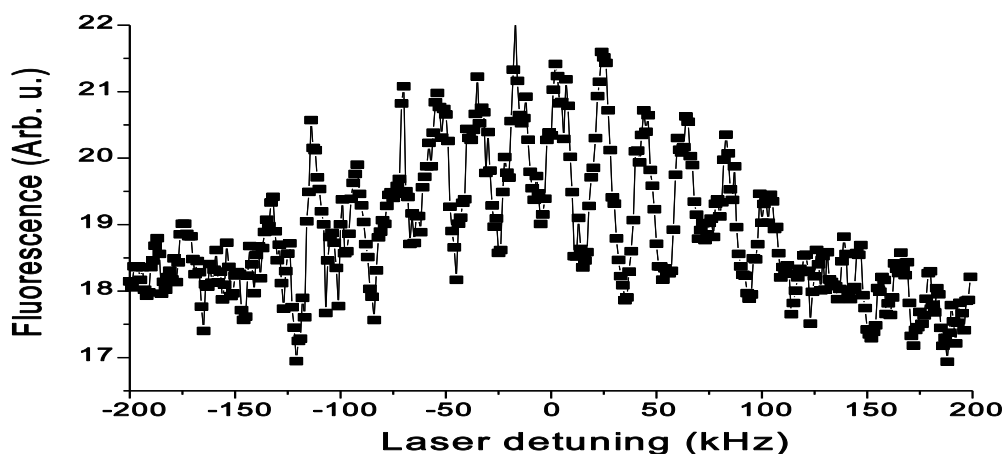
Fig. 4.11 Pulsed RBI in the trap with a 20 kHz period of fringes.

To obtain the optimum Ramsey fringe amplitude the width of the Ramsey pulse is optimized. Fig. 4.12 shows the measured Ramsey fringe amplitude as a function of the pulse width for an intensity of 6.8 mW/mm^2. The optimum fringe amplitude occurs at a pulse width of 4 µs which corresponds to a 0.7π pulse. This deviates from the expected $\pi/2$ pulse. Such a larger value has also been
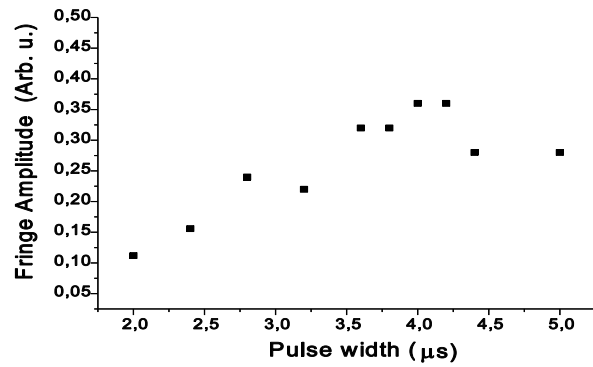
Fig. 4.12 Ramsey fringe amplitude vs. the pulse width.

mentioned by Bordé [Bod 84]. It results from the spatial dependence of the Rabi frequency Ω_0 which is due to the Gaussian profile of the spectroscopic laser beam.

To check the validity of the recapture model, we have measured the Ramsey fringe amplitude as function of the trapping laser off-time as shown in Fig. 4.13. The solid line is the theoretically predicted curve according to eq. 4.8. with the excitation probability calculated from eq. 3.17 but mutiplied with one free fitting parameters to match the experimentally measured trap loss due to spectroscopy. The fringe
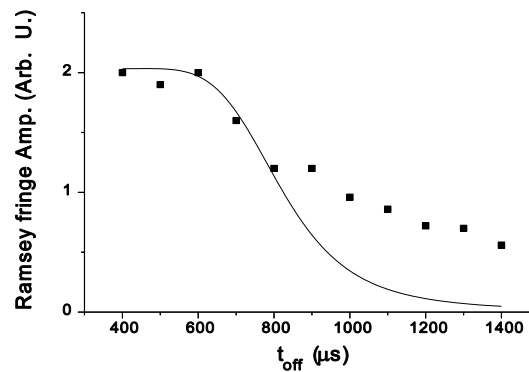
Fig. 4.13: Ramsey fringe amplitude vs. the trapping laser off-time t_{off}. The solid line is theoretically expected value .

amplitude does not drop down so fast as expected. The possible reason is that for larger t_{off} the recapture probability is not so large as expected since the trap has expanded to a large region where the small trap assumption is not valid any more.

High resolution Ramsey fringes

By variation of the pulse separation of forward and backward Ramsey pulse pairs different fringe resolution is obtained. Some examples are shown in Fig. 4.14 for an integration time of 1 s. Also shown are the signal-to-noise ratio (S/N) and the linewidth of the fringes, where the
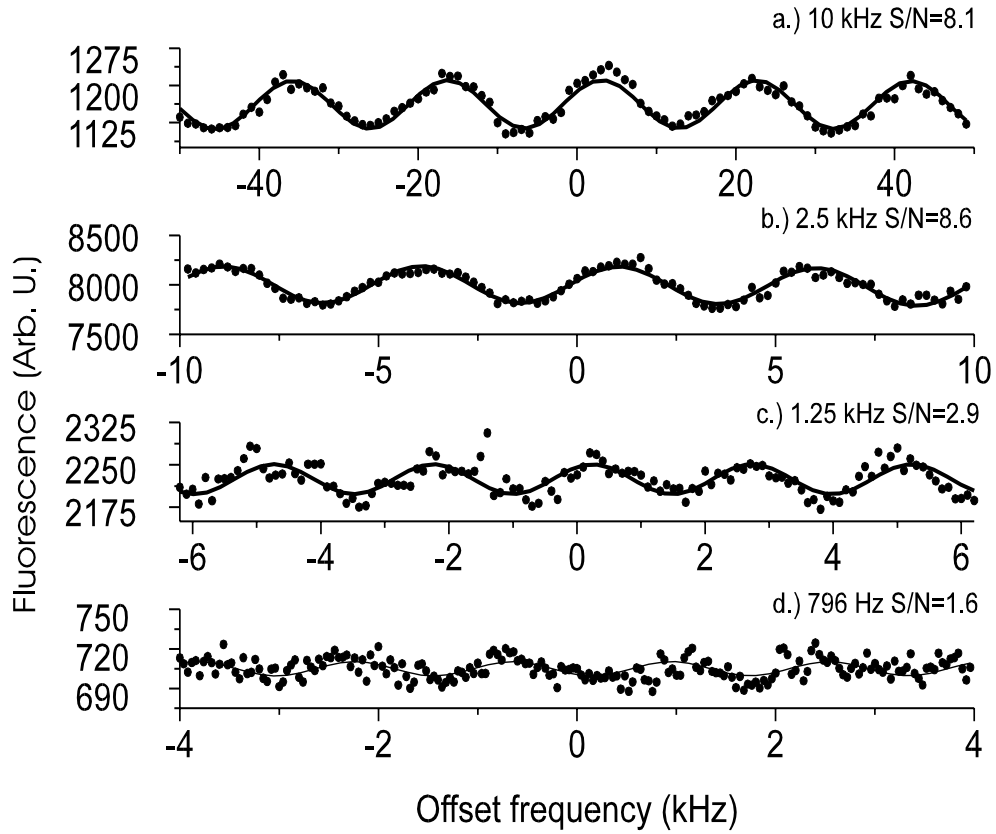
Fig. 4.14: Ramsey fringes in the trap for different resolutions. The line-width which is defined as half the period of the fringes and signal-to-noise ratio are shown in the right side.

linewidth is defined as half the period of the fringes. According to section 3.2 the period of the fringes should be $1/2T_p$ where T_p is the effective pulse separation. The value of effective pulse separation T_p can be derived from the Fourier transformation of the fringes. The periodic fringe is presented as a function of the frequency so the Fourier transformation of the fringes will be a spectrum peaked at $2T_p$. Fig. 4.15 shows such a Fourier spectrum of the fringe from Fig. 4.14 b). The measured T_p should be larger than experimentally assigned value $T+\tau$ as discussed in section 3.2 since the value of $\Omega\tau$ is larger than 1 in the experiment.
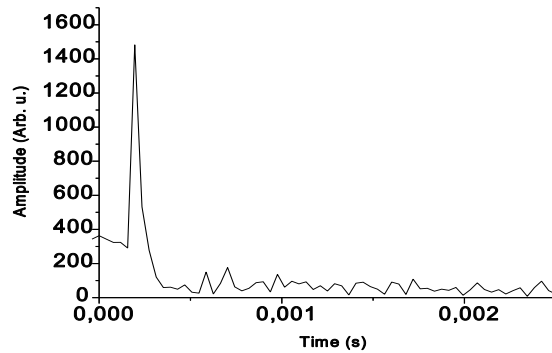
Fig. 4.15: Fourier spectrum of the Ramsey fringe shown in Fig.4.14 b).

77

Fig. 4.16 shows the measured T_p from the Fourier spectrum as a function of $T+\tau$. The solid line is given by $T_p = T+\tau$. The error bar of each point is defined as the FWHM of the peak at $2T_p$ shown in Fig. 4.15. The measured effective pulse separation within the measurement error is predicted as in section 3.2. The error bar is larger for higher resolution Ramsey fringes due to a smaller signal-to-noise ratio. For example the S/N drops down to 1.6 for 796 Hz linewidth as shown in Fig. 4.14.
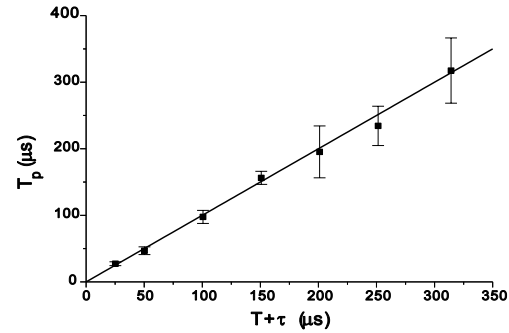
Fig. 4.16: The measured effective pulse separation vs. experimentally assigned $T+\tau$

The linewidth of 796 Hz corresponds to a Q factor of $8\cdot10^{11}$, where Q is the resonance frequency devided by the linewidth. The stability of a laser oscillator stabilized to a resonance transition can be described by [Ita 91]

$$\sigma_y(\tau) \; = \; \frac{K}{Q\,S/N} \; \propto \; \frac{1}{\sqrt{\tau}}$$

where K is a dimensionless constant and S/N is the signal-to-noise ratio of a measurement time τ. It is the product of Q and S/N that affects the stability. High Q does not necessarily imply high stability because the signal-to-noise ratio S/N must also be considered. Fig. 4.14 shows that the best stability is achieved for the fringe with 2.5 kHz linewidth. For this fringe the Allan variance was studied in more detail as discussed in chap. 5.

The resolution limit

The fringe contrast is usually defined as the ratio of the fringe amplitude to the Doppler depth. It is 16, 14, 9 and 5% for fringes from a to d, respectively in Fig. 4.14. The contrast drops down for a higher resolution. This loss in contrast can be due to the variation in excitation probability which is resulted from the Gaussian intensity profile of the spectroscopy laser beams, laser frequency fluctuation and the signal-to-noise ratio. First we considered the effect of laser frequency fluctuation and signal-to-noise ratio.

The minimum detectable fringe is usually determined by S/N=1. Assume that there is x% of noise for the trap signal. Then S/N=1 implies

$I_{max} - I_{min} = x\% \cdot I_{max} + x\% \cdot I_{min}$

where I_{max} and I_{min} is the maximum and minimum fluorescence of the fringe. This leads to a minimum detectable visibility

$$Visibility = \frac{I_{max} - I_{min}}{I_{max} + I_{min}} = x\%$$

Here we will define the fringe visibility as $(I_{max} - I_{min})/(I_{max} + I_{min})$ to distinguish it from contrast as defined above. Note that often visibility is a synonym for contrast. Instead of contrast the visibility will be used for the discussion of the resolution limit of the fringes since it is directly related to the S/N. Fig. 4.17 shows the measured fringe visibility as a function of the fringe periodicity for a constant trapping laser off-time. The dashed line shows the limit of detectable visibility which is equal to the noise of the detected
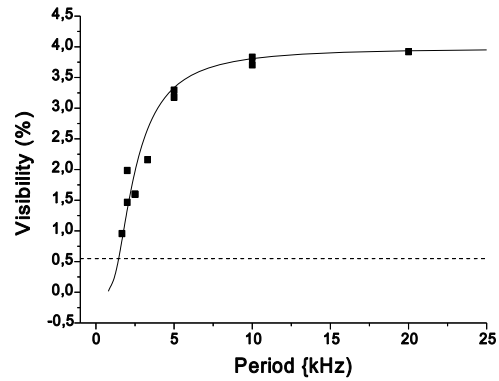
Fig. 4.17: Visibility of the fringe vs. the fringe period. The solid curve is calculated curve with the consideration of laser frequency fluctuation. The dash line is the minimum detectable visibility.

fluorescence in the corresponding measurement. The solid line is the theoretically predicted curve with consideration of the spectrometer frequency fluctuation as described below.

The fringe signal is proportional to $\cos[(\Delta-\delta)2T_p] + \cos[(\Delta+\delta)2T_p]$ under the assumption of monochromatic light field. In reality the laser is never monochromatic and there are always fluctuations which affect the phase or the frequency. So the laser has a finite frequency linewidth and frequency stability. We will treat both properties as frequency fluctuations of an ideal monochromatic laser. The Ramsey fringes should then be the time averaged value of $\langle\cos[(\Delta+f(t)-\delta))2T] + \cos[(\Delta+f(t)+\delta)2T]\rangle$ where $f(t)$ is the frequency fluctuation from ideal monochromaticity. This time averaging can be more easily treated as an ensemble average $\langle\cos[((\Delta+f_n)-\delta)2T] + \cos[((\Delta+f_n)+\delta)2T]\rangle$. The frequency fluctuation f_n is assumed to have a Gaussian distribution:

79

$$p(f_n) \ = \ \frac{1}{\sqrt{2\pi} \ \sigma_f} \ e^{-\frac{f_n^2}{2\sigma_f^2}}$$

To calculate the fringe amplitude 1000 samples of frequency fluctuations are used for various periods of fringes. The average height of the fringes $(I_{max}+I_{min})/2$ has been set such that it has the same value as the experimentally measured height of the 20 kHz period fringe. The calculated visibility is shown as solid line in Fig. 4.17. The best fit to the measured visibility has a frequency fluctuation $2\sigma_f$ of 920 Hz. The behavior of the measured fringe visibility is in good agreement with the expected curve. We conclude that the reduction of the visibility when varying the fringe period is mainly due to the frequency fluctuation of the spectrometer. An analysis of the contrast as a function of the pulse separation which shows an exponential decay curve [Sen 94] also confirms this conclusion [Rus 98].

The frequency fluctuation can be traced back to the laser line width and its stability. Since the measured stability of the spectrometer is $5 \cdot 10^{-13}$ (see section 5.2) this contributes 320 Hz fluctuation. The residual fluctuation resulting from the laser line width is determined to be $\sqrt{920^2 - 320^2}$ =860 Hz。 The dashed line shows the minimum detectable visibility which is equal to the noise (0.6% at integration time of 1.0 s) of this measurement. The minimum period is 1.5
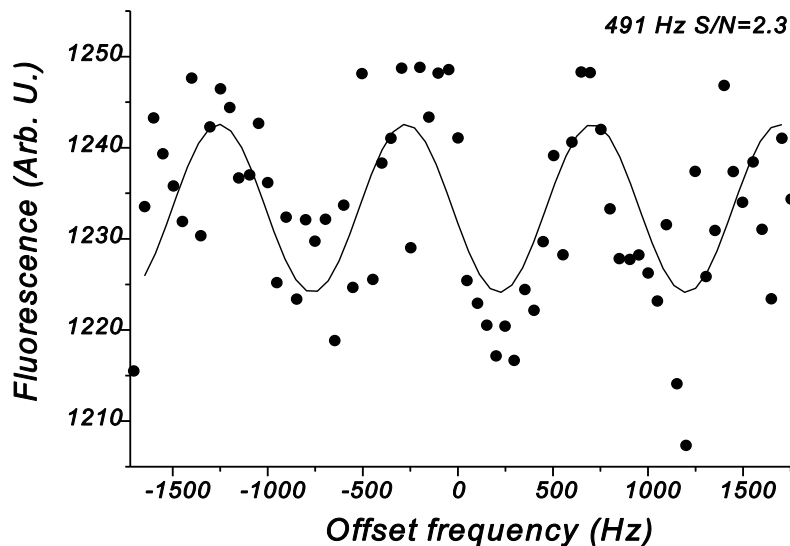
Fig. 4.18: High resolution Ramsey Fringes with linewidth of 491 Hz.

kHz which is also consistent with that measurement.

The other effect which reduces the visibility is due to the smaller excitation probability for higher resolution. In this case the pulse separation will be larger. The atoms will expand more after the first pulse and experience smaller intensity in the far wing of the Gaussian profile. Therefore, the excitation probability from the second pulse is smaller. Such an effect contributes about 6 % in reduction of visibility for T=300 µs. This amount has been checked by enlarging the spectroscopic laser beam radius from 1.7 to 2.2 mm. The linewidth of the fringes has been improved towards 491 Hz (see Fig 4.18). This is smaller than the lower limit mentioned above. Such a large improvement can not be explained with the larger size of the laser beam. We assumed that it is due to an occasional frequency stability improvement of the spectrometer. Further frequency stabilization of the spectrometer is discussed in the next section.

4.5 Some possible improvements

Reducing the spectrometer line width

The present resolution is mainly limited by the linewidth of the spectrometer. Although the stabilization of the laser to the reference resonator can reach sub-Hz regime the distance between the spectrometer and the trap is still some meter long. Any disturbance in-between such as vibrations of the mirrors give rise to phase and frequency fluctuation. It is therefore important that the frequency stabilization is just located near to the trap. This can be done either by building a new trap on the spectrometer table or a new frequency discriminator next to the trap. The later is now in progress.

Reducing the recapture probability

The other improvement is to reduce the recapture probability. The recapture probability of the present experiment as mentioned in section 4.2 is about 47%. Reducing this recapture probability can increase the visibility. The trap region is the main factor that affects this probability.
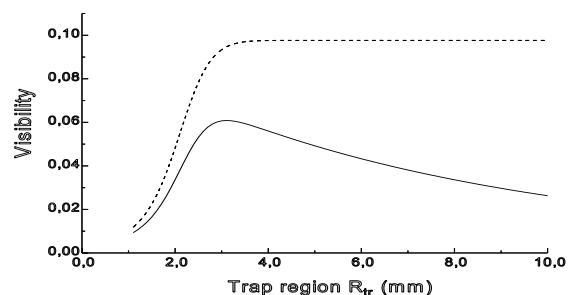
Fig. 4.19. The dependence of the visibility on the trap region with consideration of recapture (solid line) and no recapture (dashed line) for a trapping laser off-time of 1 ms.

81

Fig. 4.19. shows the calculated visibility as a function of the trap region for trapping laser off-time of 1 ms. The maximum visibility occurs at a trap region of 3mm. This maximum value is a compromise between recapture probability and the effusive loss. Also shown is the visibility for no recapture. It is clear that the visibility is better since the atoms excited in spectroscopy will all be lost and enhance the signal.

Reducing the recapture probability is necessary for approaching the limit of the resolution which is the natural linewidth of the $^3P_1$ state. To reach this limit, the trapping laser beams should be turned off at least as long as the life time of the $^3P_1$ state. This means that during a spectroscopic cycle the trapping laser must be turned off at least for 10 ms. In this case the trap expands to a radius of about 10 mm at the usual MOT temperature. The trap depth should also be much larger than this value in order to avoid large
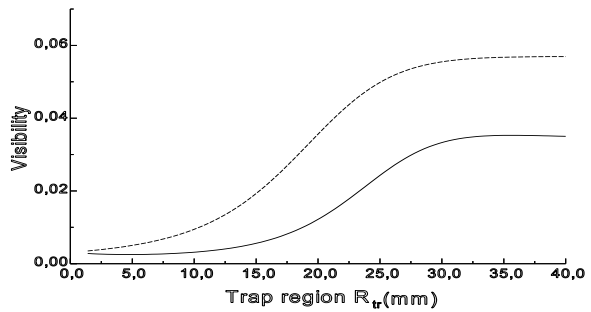
Fig. 4.20 The dependence of the visibility on the trap region R_{tr} with the consideration of recapture (solid line) and no recapture (dashed line) for a trapping laser off time of 10 ms.

effusive loss rates. For such a large trap radius the recapture rate is also high (~86% for R_{tr}=10mm). Fig. 4.20 shows the Ramsey fringe visibility as a function of the trap region for a trapping laser off-time of 10 ms. This recapture probability can be decreased by pumping the $^3P_1$ state to other states such as $^3P_2$ or $^3P_0$ via $^3D_2$ (3s5d). The trap region can then be made as large as possible as long as the trapping power is available. The $^3D_2$ has a lifetime of 34 ns. For a pumping intensity I>I_{sat} =2.6 mW/mm^2 the atoms will be pumped away after 15 cycles which corresponds to a pumping time of about 1 µs only. This is much shorter than the life time of the $^3P_1$ state which means that effective optical pumping can be reached without atoms decaying back to the ground state. The transition $^3P_1$-$^3D_2$ has a wavelength of 284.9 nm. This can be obtained from the present second harmonic generation where the power is also enough for the effective optical pumping.

Chapter 5
Frequency standards

Since the first atomic beam apparatus used as a frequency standard [Ess 55], atomic frequency standards have developed rapidly in the microwave region [Aud 76]. In the optical frequency regime many candidates have been suggested [Hall 89]. The performance of a frequency standard is usually characterized by two quantities: accuracy and stability. Accuracy refers to the deviation from the ideal transition frequency of free atoms at rest. The evaluation of the accuracy of a frequency standard includes all errors derived from independent measurements and the theoretical predictions of the system. Stability refers to the variation of the average frequency from one interval time to the next. The characterization of a frequency stability has been extensively discussed in [IEEE 66]. In the subsection some basic concepts of frequency stability will be first described. The measurement of the stability of the present Mg frequency standards and a comparison to other standards will be given in section 5.2. The accuracy will be summarized in section 5.3.

5.1 Frequency stability

The output of an ideal noise-free nondrifting oscillator would be a pure sine wave, but any real oscillator is perturbed by random noise and other factors which affect the frequency stability. A simple model that was widely used to describe a real oscillator is

$$V(t) \; = \; (V_0 + \epsilon(t)) \; \sin[2\pi\nu_0 t + \phi(t)] \tag{5.1}$$

where $\epsilon(t)$ is the amplitude fluctuation and $\phi(t)$ characterizes the phase noise.
Usually, for high-quality frequency sources the amplitude fluctuation $\epsilon(t)$ is very small and can be neglected. We will only consider the frequency instability resulting from phase fluctuations. The instantaneous frequency of such a signal is

$$\nu(t) \; = \frac{1}{2\pi}\frac{1}{dt}[2\pi\nu_0 t + \phi(t)] = \nu_0 + \frac{1}{2\pi}\frac{d\phi(t)}{dt} \tag{5.2}$$

The frequency noise is then the random process defined by

$$\Delta v(t) \ = \ \frac{1}{2\pi}\frac{d\phi(t)}{dt} \tag{5.3}$$

Usually the normalized dimensionless fractional frequency fluctuation is introduced:

$$y(t) = \frac{\Delta v(t)}{v_0} \tag{5.4}$$

The characterization of y(t) of a frequency source can be described in the frequency domain [Cul 66] or time domain [Bar 66, All 66].

Frequency domain

In the frequency domain the fluctuations of the frequency are characterized by the one-side spectral density $S_y(f)$ of the fractional frequency fluctuation y(t), where f is a Fourier frequency component. It has been shown that the spectral density of the frequency fluctuation for usual frequency generators can be represented as a superposition of independent noise processes by [Bar 71]

$$S_y(f) \ = \ \sum_{\alpha=-2}^{2} h_\alpha \, f^\alpha \tag{5.5}$$

where h_α are constants.

The various terms corresponding to α represent different types of noise sources. Typical noise found in the usual frequency standards are listed in Table II. A detailed discussion of these noises can be found in [Les 79, How 81].

The power spectral density of the fractional frequency fluctuation of a

α	denomination of the type of noise
-2	Random walk frequency noise
-1	Flicker frequency noise
0	White frequency noise
1	Flicker phase noise
2	White phase noise

Table II. Typical noise in usual frequency standards.

slaved laser oscillator locked to an atomic reference as shown in Fig. 5.1 can then be described

84

by the following expression [Cut 66]

$$[S_y(f)]_{L,l} \;=\; \frac{1}{|1+G(f)|^2}\,[S_y(f)]_{L,f}\;+\;\left|\frac{G(f)}{1+G(f)}\right|^2 [S_y(f)]_{at} \qquad (5.6)$$

where the subscripts at, L, l, f indicate atomic reference, laser, locked and free (unlocked to atomic reference), respectively. G(f) represents the servo loop gain $K_rK_og(f)$ and it can be described in terms of a low pass filter in the stabilization scheme described in section 4.3. Equation 5.6 can then be rewritten as [Aud 80]
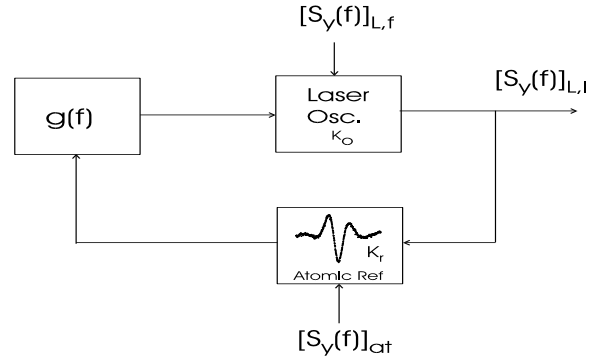
Fig. 5.1: Block diagram of the passive atomic frequency standard.

$$[S_y(f)]_{L,l} \;=\; \frac{(2\pi fT)^2}{1+(2\pi fT)^2}\,[S_y(f)]_{L,f}\;+\;\frac{1}{1+(2\pi fT)^2}\,[S_y(f)]_{at} \qquad (5.7)$$

where T is the time constant of the servo-loop. In the stabilization scheme described in section 4.3, the time constant is mainly determined by the total PMT integration time for the 1st harmonic technique which is 1 s. It is seen from eq. 5.7 that the fast frequency fluctuation of the laser is not affected by the servo-loop and the slow ones are determined by the atomic reference. Consequently, for long term the frequency stability is determined by the atomic reference.

Time domain:

Time and frequency counting techniques are well known. They are more precise than frequency power spectrum measurements for signals having a low frequency which is the usual case for high stable frequency standards. Since the instantaneous frequency can not be measured it always takes some time τ to measure the frequency fluctuations. Therefore, the measured frequency fluctuation is the averaged value over integration time τ.

$$\bar{y}_k(\tau)=\int_{t_k}^{t_k+\tau}\frac{\Delta\nu(t')}{\nu_0}\,dt' \qquad (5.6)$$

85

The time domain frequency stability is usually defined by the Allan variance [All 66] or two sample variance which is equal to the variance of two adjacent measurements.

$$\sigma_y^2(\tau) = \frac{1}{2} \langle (\bar{y}_{k+1} - \bar{y}_k)^2 \rangle \qquad (5.7)$$

where <> means infinite time average.

In practice, only a finite number of measurements can be realized. Given a set of measured fractional frequency fluctuation $y_i^{\tau 0}$ where τ_0 is the integration time of each data point, a new set of data y_i^{τ} can be obtained by averaging n adjacent values of $y_i^{\tau 0}$ with $\tau = n\tau_0$. For a set of m data points $y_i^{\tau 0}$ the Allan variance for general $\tau = n\tau_0$ becomes [All 87]

$$\sigma_y^2(\tau) = \frac{1}{2(m-2n+1)} \sum_{k=1}^{m-2n+1} (\bar{y}_{k+n}^{\tau} - \bar{y}_k^{\tau})^2 \qquad (5.8)$$

where

$$\bar{y}_k^{\tau} = \frac{1}{n} \sum_{i=k}^{k+n-1} \bar{y}_i^{\tau 0} \qquad (5.9)$$

The time domain $\sigma_y(\tau)$ and frequency domain $S_y(\tau)$ stability can be related by the following equation [Bar 71]

$$\sigma_y^2(\tau) = 2 \int_0^{f_h} S_y(f) \frac{\sin^4(\pi f \tau)}{(\pi f \tau)^2} \, df \qquad (5.10)$$

where it is assumed that a low pass filter shows a sharp cut-off frequency f_h since there always exist low pass filter exist in the measuring system or in the frequency generator. For the type of noise mentioned above the corresponding time domain Allan variance has the form

$$\sigma_y^2(\tau) = K_u \tau^u \qquad (5.11)$$

for $2\pi f_h \tau \gg 1$. The corresponding values of u are:

α	2	1	0	-1	-2
u	-2	-2	-1	0	1

Besides the above mentioned random noise there is another possible contribution to the Allan variance which comes from the drift of the frequency. It can be shown that for a linear frequency drift y(t)= kt (k is constant) the Allan variance is

$$\sigma_y(\tau) \ = \ \frac{k}{\sqrt{2}} \ \tau \qquad\qquad (5.12)$$

It is possible to determine the particular noise which perturbs the frequency stability by measuring $\sigma_y(\tau)$ and by plotting its variations in log-log coordinates. The slope of $\sigma_y(\tau)$ then depends on the noise process which is involved, except for α=1 and 2. In that case one can distinguish the two kinds of noise by different kinds of techniques [Aud 80].

In the next section the stability of the present spectrometer will be characterized in the time domain. Comparison with other frequency standards will be described.

5.2 Measurement of the Allan variance

The dye-laser spectrometer as described in section 4.3 has an excellent short term stability. For long term it is stabilized to the low frequency component of the Ramsey fringe of the thermal atomic beam. The Ramsey fringes obtained with the thermal atomic beam have a line Q of $3.3 \cdot 10^{10}$ and signal to noise ratio (S/N) of 73. When this signal was used for frequency stabilization a fractional frequency stability of $2.3 \cdot 10^{-13}$ could be obtained [Rie 96]. In order to measure this frequency stability independent from the predicted value we have compared the frequency of the laser spectrometer with the eigenfrequency of atoms in the trap. The frequency evolution of the spectrometer is derived from the phase shift of the Ramsey fringes in the trap. To determine the phase shift we model the fringes by
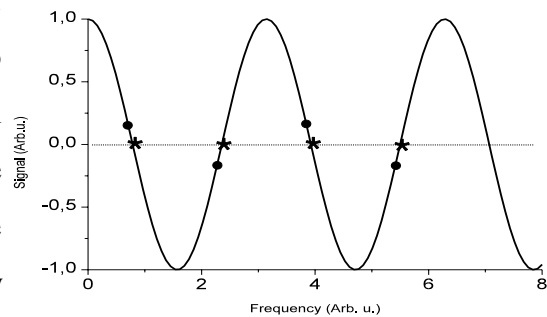
Fig. 5.2: The Ramsey signals for four fixed AOM modulation frequencies. The measured values shift when the laser frequency changes .

the equation

$$a \cos[2T_p(\Delta+\phi)]+b+c (x-d)^2 \qquad (5.13)$$

where a and ϕ describe the fringe amplitude and phase, respectively. The last two terms describe the Lamb dip background. The parameters a, b, c, d and ϕ can be first determined from fitting to the fringe of a complete scan as in Fig. 4.14. Later, the phase can be determined by four measured points near the zero of the fringe as shown in Fig. 5.2, where zero refers to the net signal when the Lamb dip background is subtracted. The measurement procedure is described below. After the laser has been stabilized at the thermal atomic Ramsey fringe minimum some cycles of Ramsey fringes around the central of Lamb dip in the trap are measured by scanning the modulation frequency of AOM2 and AOM3 (see Fig. 4.8). From this fringe the initial parameters a, b, c, d and ϕ can be determined. In the consecutive time the fringe signal is continuously measured only at four fixed frequency points which correspond to the zeros of the initial fringes. From the four-point fringe signal the phase ϕ_i can be determined from eq. 5.10 by fixing the amplitude parameter a. The laser frequency change $\Delta\nu_i$ compared to the initial scan is then equal to $\phi_i/2T_p$. For this measurement a 5 kHz Ramsey fringe is measured since it has a better stability according to section 4.4. The sampling time of each frequency point is 1 s. From the set of measured fractional frequencies $y_i^{\tau 0} =\Delta\nu_i/\nu_0$ with $\tau_0=4s$ the Allan variance can be calculated according to eq. 5.8. The measured Allan variance is shown in Fig. 5.3 for three consecutive measurements. For short sampling time the

Fig. 5.3: Allan standard deviation of the spectrometer stabilized on the Ramsey fringe minimum and measured relatively to the atomic eigenfrequency in the trap. Three consecutive measurements are shown.

Allan standard deviation is described by $\sigma_y(\tau) =2.7\cdot10^{-13}/\sqrt{\tau}$. This behavior is dominated by the shot noise (white frequency noise) which result from the statistics of counting transitions in a quantum system. For long term ($\tau>70s$) the three consecutive measurements show larger differences since the available data set is smaller and the error of the measurement increases.
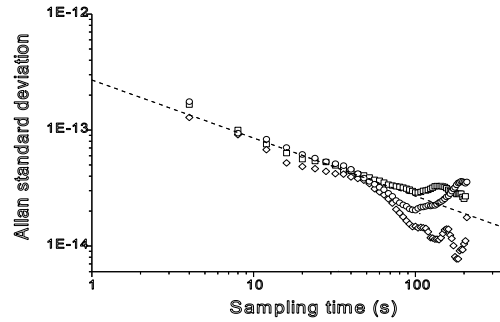
The measurement also shows possible drifts of the spectrometer at long-term. With still longer measurements (sampling time up to 600 s) the drift has been confirmed and we get a larger Allan standard deviation of $\sigma_y(\tau) = 5 \cdot 10^{-13}/\sqrt{\tau}$. This stability fluctuation depends strongly on the behavior of the dye laser. The flicker floor is not seen in this range of sampling times. The stability is possible below 10^{-14} for long-term according to Fig. 5.3. The potential of the stability is still to be explored when the stabilization of the spectrometer is improved. The drift is assumed to result from the drift of spectrometer power while it results in an asymmetry of the fringe through the 2nd order Doppler effect. This will influence the stabilization scheme used at present and result in a frequency drift. Further intensity stabilization should resolve this problem.

The stability at a sampling time of 1s which is derived by extrapolating the curve to 1s in Fig.5.3 is $(2.7 \pm 0.3) \cdot 10^{-13}$. Although this stability is the relative stability measured between the thermal atomic beam and the trap, we believe that it is limited by the stabilization of the spectrometer on the Ramsey fringe in the thermal atomic beam. The stability is expected to improve when the spectrometer is stabilized on the Ramsey fringe in the trap. Further evidence can be found by comparing the stability measured with a second Mg trap. The construction of such a new trap is in progress in the SFB project in this group.

Comparison with other frequency standards

In recent years many groups have been engaged in improving the conventional Cs frequency standard or investigating new optical frequency standards [EFTF 95]. Fig. 5.4 shows the stability of some classical frequency standards and new investigations. At 1s sampling time the stability of the present spectrometer stabilized on the thermal Mg atomic Ramsey fringes is already better than the conventional Cs frequency standard
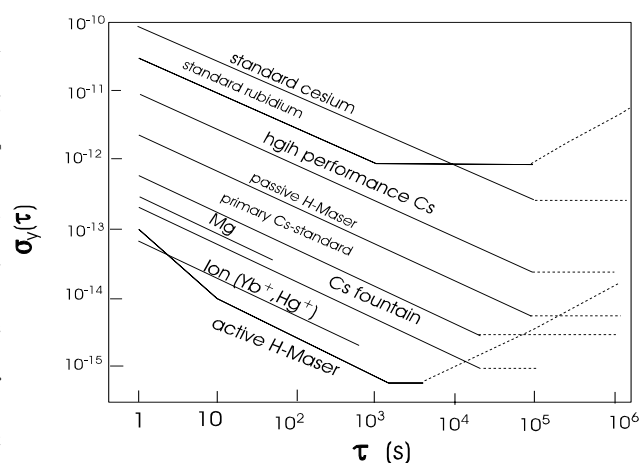
Fig. 5.4: Allan standard deviation of some frequency standards. Source [Lew 91, Ghe 95, Mal 95]

89

and comparable to new Cs fountains. Since both Q and S/N can still be improved for the RBI in the trap, a further improvement of the stability of Mg frequency standard is expected.

5.3 Frequency accuracy

The evaluation of the frequency accuracy of a spectrometer locked to one of the Ramsey fringes involves all the effects that shift the position of the fringe. These effects have been intensively studied [Sen 94, Bet 96]. Some significant effect will be summarized in the following table.

Effect	thermal beam RBI	Pulsed RBI
residue 1st order Doppler shift	~300 Hz	~ 1 Hz
2nd order Doppler shift	~300 Hz	~ 10 mHz
phase uncertainty	~ 300 Hz	< 1 mHz
quadr. Zeeman-effect ($\sim 1.64 Hz/G^2$)	<< 1 Hz (for B<1mG)	<< 1Hz
Stark shift (0.3 Hz $(V/cm)^{-2}$	<< 1 Hz	<< 1 Hz
earth rotation	<< 1 Hz	<< 1 Hz
gravitational effect	~ 10 Hz	~ 1 Hz

More attention should be directed towards the 2nd order Zeeman effect. Since no large efforts has been done to reduce the stray magnetic field from the Zeeman magnet, there is still a 14 G bias magnetic field during the spectroscopy in this work. This results in a frequency shift of about 400 Hz ($1.64Hz/G^2$). With a more carful shielding or other trap configuration (chirp cooling or the trap configuration developed by PTB) the stray magnetic should not be a problem. The other effect which was underestimated before, is the frequency pulling due to the neighbor recoil component. As mentioned in section 3.2 it is not easy to experimentally get the optimum effective pulse separation T_p since it also depends on the Rabi frequency and the pulse width. T_p can vary from $T+ \tau$ to $T+4\tau/\pi$ for $\Omega \tau$ changing from $\Omega \tau <<1$ to $\Omega \tau = \pi/2$. The adjustment of T and τ according to the Ramsey fringe amplitude to reach the optimum value of T_p will not be more exact than 0.1 µs since the fringe amplitude is not so sensitive to such a change. This already results in a frequency shift of 8 Hz for T=500 µs. Suppression of one of the recoil

component is the only way to reach higher accuracy. This is easy to realize as mentioned in section 3.2. Based on pulsed RBI in the trap with one recoil component suppressed an accuracy of $2 \cdot 10^{-15}$ can be obtained.

Chapter 6

Conclusion and Outlook

By the systematic studies, the improvements and measurements discussed in this work the potential for an optical frequency standard based on the Ramsey-Bordé interferometer with magnesium atoms could be clearly demonstrate. High resolution Ramsey fringes and a high stability for measurements on trapped atoms are achieved.

The present resolution is mainly limited by the 457 nm laser spectrometer. Many improvements are possible at this setup and currently investigated. To be accepted by Bureau International des Poids et Mesures (BIPM) as an optical frequency standard a simple and long term stable laser source is an important factor. The present dye laser system for 457 nm can be replaced by a frequency doubled solid state laser. The 457 nm laser can be generated from frequency doubling the Ti:Saphire laser with a $KNbO_3$ crystal kept at temperature of $138\,^\circ C$. The pumping laser for the Ti:Saphire laser can be a compact commercial frequency doubled Nd:YAG laser which is pumped by a diode laser. Since $KnbO_3$ has a large nonlinear coefficient of $d_{32}=20$ pm/V. High efficient SHG can be achieved. In ideal case a conversion coefficient η has a value of $2.7 \cdot 10^{-2}$ 1/W for a crystal length of 1 cm. The real power from SHG will be limited by the thermal effect, the damage threshold of the crystal and the blue light induced absorption. Further study will be needed to evaluate the SHG efficiency. Another possible SHG setup is to use the quasi-phase matching method with $LiNbO_3$. A high conversion efficiency is also expected. Based on such systems a high stable portable Mg frequency standard can be realized since all the components can be built very compact. For an optical frequency standard it is important that the frequency can be compared with the present Cs frequency standard. Such a frequency chain can be realized by phase-locking different laser systems by means of nonlinear processes. Schantz et al. have compared the Ca stabilized laser and the Cs clock with the frequency chain developed at the PTB [Sch 96a]. T.W. Hänsch has also developed a method for the frequency chain through phase locking of harmonic and sum frequencies [Tel 90].

The present work has developed methods according to which the interferometer in the trap can be easily operated. This can enhance the realization of further experiments on the trap. The Zeeman 2nd order effect can be precisely measured by varying the magnetic field strength of the bias magnetic field at the spectroscopy time. The influence of collisions between trapped

atoms can also be studied by varying the density of the trapped atoms or by proper selection of the spectroscopic starting time after turning off the trapping laser since different densities can be reached during the expansion of the atomic cloud. From the observed fringe contrast and the phase difference of the signals the collision properties like the real and imaginary part of the scattering amplitude can be deduced.

It is also easy to realize gedanken experiments like the Heisenberg microscope using the time domain Ramsey-Bordé interferometer in the trap. Between the 2nd and 3rd Ramsey pulse both paths of the interferometer are in the ground states. By radiating a resonant 285 nm laser pulse during this time interval the variation of the fringe contrast due to single photon scattering can be detected. The dependence of the fringe contrast on the distance between the two paths of the interferometer can be measured by changing the pulse separation between 1st (3rd) and 2nd (4th) Ramsey pulse. The pulse width and power of the 285 nm laser can be properly chosen such that the atom scatters in most cases only a single photon. Other influences like the polarization of the radiating photons is also an interesting effect. The realization of these experiments, which can be seen in near future [Hin 98] should open more opportunities to study fundamental quantum mechanical issues like EPR paradox [Ein 35] and GHZ states [Gre 90]. Until now the interference phenomena studied are only one atom interferences since the density is still much too low that there is only one atom at a time within a single coherence length. The uncertainty of which way the atom passes the interferometer will result in a quantum limit to the particle-number fluctuations at the outports of the interferometer. This quantum-noise limit will limit the sensitivity of the matter-wave interferometer. At high phase densities the coherences between atoms will influence the quantum-noise limit. The statistical dependent contribution of the coherences are different for the different atoms and the use of fermionic atoms will tend to lower the quantum-noise limit [Scu 93]. Magnesium has both fermionic (^{25}Mg) and bosonic (^{24}Mg, ^{26}Mg) isotopes. The extension of the present work towards high phase space density for the varies Mg isotope is an extremely interesting field to exploit these quantum-noise limits. To enhance the phase space density the Mg atoms should be further cooled. Besides the cooling methods suggested in [Rus 98] here another possible cooling method for Mg or other alkali earth atoms is suggested. It is based on forced evaporative cooling in a far-off resonance trap (FORT). By appropriate selecting the FORT laser it is possible to build an attractive potential for the ground $^1S_0$ state and a repulsive potential for the excited $^3P_1$ state. For Mg this case can

be achieved using the Ar-ion laser 514 nm line as a FORT laser. By focusing a laser beam with power of 5 W to a waist of 5 µm the trap potential for the ground state is U_g=5 mK and the maximum repulsive potential for the excited state is U_e=72 mK. The repulsive potential can produce an acceleration larger than $1 \cdot 10^6$ m/s^2 for r<5 µm, where r is the distance away from the FORT center. Once the atoms are excited they will never be trapped since the life time of the excited state is long enough for the atoms to be pushed away from the trap. When the laser linewidth is narrow enough only a small velocity range of atoms can be excited due to the narrow intercombination transition. Similar to the RF-induced evaporative cooling in the realization of BEC, a forced evaporative cooling can be realized in the FORT when the hot atoms are selectively excited. The scale of s-wave scattering length plays an important role in the evaporative cooling. Both using external magnetic field [Moe 95] and near resonant light fields [Fed 96] have been suggested to modify the scattering length. For Mg the near resonant light field method can be used to modify the scattering length. Using the two photon associative spectroscopy to detect the position of the last bound state [Abr 95] can be used to on line monitor the effect of the external light field since the scattering length is sensitive to the position of the last bound state.

Besides the cooling effect the heating effect coming from the FORT laser should also be considered. With the above mentioned parameter the photon scattering rate resulting from the off resonant scattering of the FORT laser is 31 photons/s. This will deteriorate the cooling effect. A method to avoid this is to integrate the above method with a FORT built with the Nd:YAG laser which is also planned for the Mg project. The Ar$^+$ laser intensity can be a factor of 10 smaller and the potential for the excited state is still repulsive ($U_e \approx$ 2mK). The photon scattering rate can be strongly reduced and the forced evaporative cooling still works. A high phase density of cold ensembles can be expected.

References

[Abr95]   E.R.I. Abraham, W.I. McAlexander, J.M. Gerton, and R.G. Hulet, Phys. Rev. Lett. 74, 1315 (1995)

[Abr96]   E.R.I. Abraham, W.I. McAlexander, J.M. Gerton, and R.G. Hulet, Phys. Rev. A53, R3713 (1996)

[Ada94]   C.S. Adams, M. Sigel, and J. Mlynek, Phys. Rep. 240, 143 (1994)

[All66]   D.W. Allan, Proc. IEEE, vol. 54, 221(1966)

[All75]   L. Allen and J.H. Eberly, Optical resonance and two level atoms, Wiley, New York, (1975)

[All87]   D.W. Allan, IEEE Transactions on ultrasonics, ferroelectrics and frequency control, vol. UFFC-34, 647 (1987)

[And95]   M.H. Anderson, J.R. Ensher, M.R. Matthews, C. E. Wieman, Science, 269, 198 (1995)

[Ari92]   Laser manipulation of atoms and ions, Proc. Of Int. School of Phys. "Enrico Fermi" Course CXVIII, ed. by E. Arimondo and W.D. Phillips, North Holland, Amsterdam (1992)

[Arn97]   M. Arndt, M. Ben Dahan, D. Guéry-Odelin, M.W. Reynolds, and J. Dalibard, Phys. Rev. Lett. 79,625 (1997)

[Ask83]   A. Ashkin and J.P. Gordon, Opt. Lett, 8, 511 (1983).

[Asp88]   A. Aspect, E Arimondo, R. Kaiser, N. Vansteenkiste, and C. Cohen-Tannoudji, Phys. Rev. Lett. 61, 826 (1988)

[Aud76]   C. Audoin and J. Vanier, J. Phys. E9, 697 (1976)

[Aud80]   C. Audoin, in "Metrology and Fundamental Constants" (Proc. Int. Fermi School of Physics), ed. by F. Milone, P. Giacomo, S leschiutta,169, North-Holland,Amsterdam (1980)

[Bab81]   M. Baba and K. Shimoda, Appl. Phys. 24, 11 (1981)

[Bad88]   conference proceedings, Matter wave interferometry, ed. by G. Badurek, H. Rauch, and A. Zeilinger Physica B151 (1988)

[Bag91]   S.N. Bagayev, V.P. Chebotayev, A.K. Dmitriyev, A.E. Om, Yu. V. Nekrasov, and B.N. Skvortsov, Appl. Phys. B52, 63 (1991)

[Bak76]   Ye.V. Baklanov, B. Ya. Dubetsky, and V.P. Chebotayev, Appl. Phys. 9, 171 (1976)

[Bal69]   W.J. Balfour and A.E. Douglas, Can. J. Phys. 48, 901 (1969)

[Bal72]   W.J. Balfour and R.F. Whitlock, Can. J. Phys. 50, 1648 (1972)

[Bar66]   J.A. Barnes, Proc. IEEE 54, 207 (1966)

[Bar71]   J.A. Barnes et. al., IEEE Trans. Instrum. Meas., IM-20(2), 105 (1971)

[Bar79]   R.L. Barger, J.C. Bergquist, T.C. English, D.J. Glaze, Appl. Phys. Lett. 34, 850 (1979)

[Bar81]   Barger R L, Opt. Lett. 6, 145 (1981).

[Bak76]   Y.V. Baklanov, B.Y. Dubetsky, V.P. Chebotayev, Appl. Phys. 9, 171 (1976)

[Ber77]   J.C. Berquist, S.A. Lee, and J.L. Hall, in "Laser spectroscopy III" ed. by Hall and Carlsten, Springer Verlag, Berlin,142 (1977)

[Ber97]   Atom Interferometry, ed. by P.R. Berman, Academic Press, (1997)

[Bet95]   D. Bettermann, thesis, (Bonn, 1995), not published

[Bet96]   D. Bettermann, J. Müller, J.L. Peng, V. Rieger, F. Ruschewitz, K. Sengstock, and W. Ertmer, in "Proceedings of the Workshop on Frequency Standards Based on Laser-Manipulated Atoms and Ions", ed. by J. Helmcke and S. Penselin, PTB-Opt-51, 1 (1996)

[Boe96]   H.M.J.M. Boesten, A.J. Moerdijk, and B.J. Verhaar, Phys. Rev. A54, R29 (1996)

[Bor69]   M. Born and E. Wolf, Principles of Optics, Pergamon, London (1969)

[Bor77]   C.J. Bordé, "New sub-Doppler interaction techniques", in "Laser spectroscopy III" ed. by Hall and Carlsten, Springer Verlag Berlin,121 (1977)

[Bor82]   C.J. Bordé, S. Avrillier, A. Van Lerberghe, Ch. Salomon, Ch. Breant, D. Bassi, and G. Scoles, Appl. Phys., B28, 82 (1982)

[Bor84]   C.J. Bordé, C. Salomon, S Avrillier, A.V. Lerberghe, C. Breant, D. Bassi and G. Scoles, Phy. Rev. A30, 183 (1984)

[Bor89]   C.J. Bordé , Phy. Lett. A140, 10 (1989)

[Boy68]   G.D. Boyd, and D.A. Kleinman, Phys. Rev. 39, 3597 (1968)

[Bra95]   C.C. Bradley, C.A. Sackett, J.J. Tolett, and R.G. Hulet, Phys. Rev. Lett. 75, 1687 (1995)

[Bur97]   E.A. Burt, R.W. Ghrist, C.J. Myatt, M.J. Holland, E.A. Cornell, and C.E. Wieman, Phys. Rev. Lett., 79, 337 (1997)

[Car91]   O. Carnal an J. Mlynek, Phys. Rev. Lett. 66, 2693 (1991)

[Che85]   V.P. Chebotayev, B. Ya. Dubetsky, A.P. Kasantsev, V.P. Yakovlev, J. Opt. Soc. Am. B2 1791 (1985)

[Chu85]   S. Chu, L. Hollberg, J Bjorkholm, A. Cable, and A. Ashkin, Phys. Rev. Lett. 55, 48 (1985)

[Cla94]   J.F. Clauser and S. Li, Phys. Rev. A50, 2430 (1994)

[Coh77]   C. Cohen-Tannoudji, B. Diu, and F. Laloë, Quantum mechanics, (1977)

[Côt95]   R.Côté, A. Dalgarno, Y. Sun, and R.G. Hulet, Phys. Rev. Lett. 74, 3581 (1995)

[Cul66]   Culter L S and Searle C L 1966, Proc. IEEE 54, 136 (1966)

[Dal89]   J. Dalibard and C. Cohen-Tannoudji, J. Opt. Soc. Am. B6, 2023 (1989)

[Dal90]   Fundamental Systems in Quantum optics, Les Houches, Session LII, 1990, ed. by J. Dalibard, J.M. Raimond and J. Zinn-Justin, Elsevier Science, Amsterdam, (1992)

[Dan92]   K. Danzmann et al.,"The GEO project: A long-baseline laser interferometer for the detection of gravitational waves, in J. Ehlers and G. Schäfer:Relativistic Gravity Research, 185, Spring-Verlag, Berlin (1992)

[Dav27]   C. Davisson and L.H. Germer, Phys. Rev. 30, 705 (1927)

[Dav95]   K.B. Davis, M.O. Mewes, M.R. Andrews, N.J. van Druten, D.S. Durfee, D.M. Kurn, and W. Ketterle, Phys. Rev. Lett. 75, 3969 (1995)

[Deg96]   R. Degner, diploma thesis, (Hannover 1996), not publoished

[Dem75]   H. Dehmelt, Bull. Am. Phys. Soc. 20, 60 (1975)

[Dmi91]   D.G. Dmitriev, G.G. Gurzadyan, and D.N. Nikogosyan,"Handbook of nonlinear optical crystals", Spring-Verlag, Berlin (1991)

[Din92]   T.P. Dinneen, C.D. Wallace, K.N. Tan, and P.L. Gould, Opt. Lett. 17, 1706 (1992)

[Din94]   F.E. Dingler, V. Rieger, K. Sengstock, U. Sterr, and W. Ertmer, Opt. Comm. 110, 99 (1994)

[EFTF95] Proceedings of the 9th European Frequency and Time Forum, Besançon, France (1995)

[Ein35]   A. Einstein, B. Podolsky, N. Rosen, Phys. Rev. 47, 777 (1935)

[Ert85]   W. Ertmer, R. Blatt, J.L. Hall, and M. Zhu, Phys. Rev. Lett. 54, 996 (1985)

[Ess55]   L.Essen and J, Parry, Nature 176, 280 (1955)

[Est30]   J. Estermann and O. Sterr, Z. Phys. 61, 95 (1930)

[Fed96]   P.O. Fedichev,Y. Kagan, G.V. Shlyapnikov, and J.T.M. Walraven, Phys. Rev. Lett. 77, 2913 (1997)

[Fey65]   R.P. Feynman and A.R. Hibbs, Quantum mechanics and path integrals, McGraw-Hill, New York (1965)

[Gal89]   A. Gallagher, D.E. Pritchard, Phys. Rev. Lett. 63, 957 (1989)

[Gau88]   U. Gaubatz, P. Rudecker, M. Becker, S. Schiemann, M. Külz, and K. Bergmann, Chem. Phys. Lett. 149, 463 (1988)

[Ghe 95] S. Ghezali, P.laurent, S. Lea, G. Santarelli, M. Bahoura, K. Szymaniec, and A. Clairon, Proc. 9th EFTF, Besançon, France , 101 (1995)

[Gib93]   K. Gibble and S Chu, Phys. Rev. Lett. 70, 1771 (1993)

[Gil95]   D.M. Giltner, R.W. McGowan, and S.A. Lee, Phys. Rev. Lett 75, 2638 (1995)

[God92]   A. Godone and C. Novero, Phys. Rev. A45, 1717 (1992)

[Gol86]   P.L. Gould, G. A. Ruff, and D. E. Pritchard, Phys. Rev. Lett. 56, 827 (1986)

[Gol88]   P.L. Gold, P.D. Lett, P.S. Juliennne, W.D. Phillips, H.R. Thorsheim and J. Weiner, Phys. Rev. Lett.60, 788 (1988)

[Gol94]   L. Goldner, C. Grez, R. Spreeuw, S. Rolston, C. Westbrook, W. Phillips, P. Marte, and P. Zoller, Phys. Rev. Lett. 72, 997 (1994)

[Gre90]   D.M. Greenberger, M.A. Horne, A. Shimony and A. Zeilinger, Am. J. Phys. 58, 1131 (1990)

[Gri93]   G.F. Gribakin and V.V. Flambaum, Phys. Rev A48, 546 (1993)

[Gri94]   R. Grimm, J. Söding, and Yu. B. Ovchinnikov, Opt. Lett. 19, 658 (1994)

[Hal89]   J.L. Hall, M. Zhu, and P. Buch, J. Opt. Soc. Am. B6, 2194 (1989)

[Ham93]   Hamamazu Technique Note, Mar. (1993)

[Hän80] T.W. Hänsch and B. Couillaud, Opt. Comm. 35, 441 (1980)

[Hän75] T.W. Hänsch and A. Schawlow, Opt. Comm. 13, 68 (1975)

[Hän80] T.Hänsch and B. Couillaud, Opt. Comm. 35, 441 (1980)

[Hel82] J Helmcke, D Zevgolis, and B. Ü. Yen, Appl. Phys 28, 83 (1982)

[Hel87] J Helmcke, J.J. Snyder, A. Morinaga, F. Mensing, and M. Gläser, Appl. Phys. B43, 85 (1987)

[Hen92] G. Hennig, theais, (Bonn, 1992), not published

[Hin97] H. Hinderthür, A. Pautz, V. Rieger, F. Ruschewitz, J.L. Peng, K. Sengstock, and W. Ertmer, Phys. Rev A56, 2085 (1997)

[Hin98] H. Hinderthür, thesis, (Hannover, 1998), in preparation

[Hof96] D. Hoffmann, S. Bali, and T. Walker,Phys. Rev. A54, R1030 (1996)

[Hol94] M.J. Holland, K.A. Suominen, and K. Burnett, Phys. Rev. A 50, 1513 (1994)

[How81] D.A. Howe, D.W. Allan and J.A. Barnes, Proc. 35th Ann. Symp. Frequency control (SFC), 669 (1981)

[IEEE 66] Special Iissue on Frequency Stability, Proc. IEEE 54 (1966)

[Ita91] W.M. Itano, Proc. IEEE, 79, 936 (1991)

[Joh75] C.J. Joachain, Quantum collision Theory, North-Holland, Amsterdam (1975)

[Joh95] K.S. Johnson, A.P. Chu, T.W. Lynn, K.K. Berggren, M.S. Shahriar, and M. Prentiss, Opt. Lett. 20, 1310 (1995)

[Joh96] K.S. Johnson, A.P. Chu, K.K. Berggren, and M. Prentiss, Opt. Comm.126, 326 (1996)

[Jon96] K.M. Jones, S. Maleki, S. Bize, P.D. Lett, C.J. Willians, H. Richling, H. Knöckel, E. Tiemann, H. Wang, P.L. Gold and W.C. Stwalley, Phys. Rev. A54, R1006 (1996)

[Jos62] B.D. Josephson, Phys. Lett., 1, 251 (1962)

[JOSA89] Special issue on Laser Cooling and Trapping of Atoms, J. Opt. Soc. Am. B6 (1989)

[Jul91] P.S. Julienne and J. Vigué, Phys. Rev. A44, 4464 (1991)

[Jul93] P.S. Julienne, A. Smith, and K. Burnett, in Advances in Atomic, Molecular, and Optical Physics (D.R. Bates and B. Bederson, eds.) Vol. 30, p.141, Academic Press, San Diego (1993)

[Kap33] P.L. Kapitza and P.A.M. Dirac, Proc. Cambridge Philos. Soc. 29, 297 (1933)

[Kas92a] M. Kasevich and S. Chu, Appl. Phys. B54, 321 (1992)

[Kas92b] M. Kasevich and S. Chu, Phys. Rev. Lett. 69, 1741 (1992)

[Kei91] D.W. Keith, C.R. Ekstrom, Q.A.Turchstte and D.E. Pritchard, Phys. Rev. Lett. 67, 181 (1991)

[Kin39] G.W. King and J.H. Van Vleck, Phys. Rev. 55, 1165 (1939)

[Ket93] W. Ketterle, K.B. Davis, M.A. Joffe, A. Martin, and D.E. Pritchard, Phys. Rev. Lett. 70, 2253 (1993)

[Kuk89] J.R. Kuklinski, U. Gaubatz, F.T. Hioe, and K. Bergmann, Phys. Rev. A40, 6741

(1989)

[Lan77] L.D. Landau and E.M. Lifshitz, Quantum Mechanics: non-relativistic theory, Pergamon Press Inc. (1977)

[Law94] J. Lawall, and Prentiss, Phys. Rev. Lett. 72, 993 (1994).

[LeR70] R.J. LeRoy and R.B. Bernstein, J. Chem. Phys. 52, 3869 (1970)

[Les79] P. Lesage and C. Audoin, Radio Sci. 14, 521 (1979)

[Let89] P.D. Lett, W.D. Phillips, S.L. Rolston, C.E. Tanner, R.N. Watts, and C.I. Westbrook, J. Opt. Soc. Am. B6, 2084 (1989)

[Let93] P.D. Lett, K. Helmerson, W.D. Phillips, L.P. Ratliff, S.L. Rolston, and M.E. Wagshul, Phys. Rev. Lett. 71, 2200 (1993)

[Let95] P.D. Lett, P.S. Julienne, and W.D. Phillips, Annu. Rev. Phys. Chem. 46, 423 (1995)

[Lew91] L. L. Lewis, Proc. IEEE 79, 927 (1991)

[Li 73] K.C. Li and W.C. Stwalley, J. Chem. Phys. 59, 4423 (1973)

[Lin96] C.Linton, F. Martin, I. Russier, A.J. Ross, P. Crozet, S Churassy and R. Basis, J. Mol. Spec.175, 340 (1996)

[Loc92] I. Lochmann, diploma thesis, (Bonn,1992), not published

[Lou83] R. Loudon, The Quantum Theory of Light, Oxford (1983)

[Mai62] H. Maier-Leibnitz and J. Springer, Z. Phys. 167, 386 (1962)

[Mal95] L. Maleti, Proc. 9th EFTF, Besançon, France, 1 (1995)

[Mar52] L. Marton, Phys. Rev. 85, 1057 (1952)

[Mar89] Frequency standards and metrology, ed. by A. De Marchi, Springer-Verlag, Berlin (1989)

[Mar91] P. Marte, P. Zoller, and J.L. Hall, Phys. Rev. A44, R4118 (1991)

[Men87] C. Mendoza and C.J. Zeippen, Astron. Astrophys. 179, 346 (1987)

[Mil93] J.D. Miller, R.A. Cline, and D.J. Heinzen, Phys. Rev. Lett. 71, 2204 (1993)

[Moe95] A.J. Moerdijk, B.J. Verhaar and A. Axelsson, Phys. Rev. A51, 4852 (1995)

[Møl93] K. Mølmer Y. Castin, and J. Dalibard, J. Opt. Soc. Am. B10, 542 (1993)

[Mor92] A. Morinaga, Phys. Rev. A45, 8019 (1992)

[Mor95] A. Morinaga and Y. Ohuchi, Phys. Rev. A51, R1746 (1995)

[Mor96] A. Morinaga and M. Nakamura, Phys. Rev. A54, R21 (1996)

[Mos83] P.E. Moskowitz, P.L. Gould, S. R. Atlas, and D.E. Pritchard, Phys. Rev. Lett. 51, 370 (1983)

[Mül94] J.H. Müller, thesis, (Bonn, 1994), not published

[Mül95] J.H. Müller, D. Bettermann, V. Rieger, K. Sengstock, U. Sterr, and W. Ertmer, Appl. Phys. B60, 199 (1995)

[Nap94] R. Napolitano, J weiner, C. J. Willians, and P.S. Julienne, Phys. Rev. Lett.73, 1352 (1994)

[Pfa93] T. Pfau, Ch. Kurtsiefer, C.S. Adams, M. Sigel, and J. Mlynek, Phys. Rev. Lett. 71,

3427 (1993)

[Pou83]   R.W.P. Drener, J.L. Hall, F.V. Kowalsky, J. Hough, G.M. Ford, H. Munly, and H. Ward, Appl. Phys. B31, 97 (1983)

[Pfa94]   T. Pfau, S. Spälter, Ch. Kurtsiefer, C.R. Ekstrom, and J. Mlynek, Phys. Rev. Lett. 73, 1223 (1994)

[Pro85]   J. Prodan, A. Migdall, W. Phillips, I. So, H. Metcalf, and J. Dalibard, Phys. Rev. Lett. 54, 992 (1985)

[Qui92]   T.J. Quinn, Metrologia, 30, 523 (1992)

[Raa87]   E.L. Raab, M Prentiss, A. Cable, S. Chu, and D.E. Pritchard, Phys. Rev. Lett. 59, 2631 (1987)

[Ram50]   N.F. Ramsey, Phys. Rev. 78, 695 (1950)

[Ram56]   N.F. Ramsey, Molecular beams, Clarendon, Oxford (1956)

[Ras95]   E.M. Rasel, M.K. Oberthaler, H. Batelaan, J. Schiedmayer, and A. Zeilinger, Phys. Rev. Lett. 75, 2633 (1995)

[Rie88]   F. Riehle, J. Ishikawa, and J. Helmke, Phys. Rev. Lett. 61, 2092 (1988)

[Rie91]   F. Riehle, Th. Kisters, A. Witte, and J. Helmke, Phys. Rev. Lett. 67, 177 (1991)

[Rie92]   F. Riehle, A. Witte, Th. Kisters, and J. Helmke, Appl. Phys. B54, 333 (1992)

[Rie93]   V. Rieger, K. Sengstock, U. Sterr, J.H. Müller, and W. Ertmer, Opt. Comm. 99, 172 (1993)

[Rie96]   V. Rieger, thesis, (Hannover 1996), not published

[Rit94]   N.W.M. Ritchie, E.R.I. Abraham, and R.G. Hulet, Laser Physics. 4, 1066 (1994)

[Rus98]   F. Ruschewitz, thesis, (Hannover, 1998), in preparation

[Sch96a] H. Schnatz, B. Lipphardt, J. Helmcke, F. Riehle, and G. Zinner, Phys. Rev. Lett. 76, 18 (1996)

[Sch96b] D. Scheller, diploma thesis, (Hannover, 1996), not published

[Sch97]   J. Schmiedmayer et al., In Atom Interferometry, ed. by P.R. Berman, Academic Press. Inc., 1 (1997) and references therein.

[Sch97]   N. Schaffrath, diploma thesis, (Hannover 1997), not published

[Scu 93] M.O. Scully and J.P. Dowling, Phys. Rev. A48, 3186 (1993)

[Sen93]   K. Sengstock , thesis, (Bonn, 1993), not published

[Sen94]   K. Sengstock, U. Sterr, J.H. Muller, V. Rieger, D. Bettermann and W. Ertmer, Appl. Phys. B59, 99 (1994)

[Ses91]   D.W. Sesko, T.G. Walker, and C.E. Wieman, J. Opt. Soc. Am. B8, 946 (1991)

[She84]   Y.R. Shen, The Principles of Nonlinear Optics, John Wiley & Sons Inc., (1984)

[Sie71]   A.E. Siegman, An Introduction to Lasers and Masers, McGraw-Hill Book Co., New York (1971)

[Smi54]   Smithsonian Physical Tables (9th ed.), Smithsonian Institution, Washington DC, 363 (1954)

[Ste86]   S. Stenholm, Rev. Mod. Phys. 58, 699 (1986)

[Ste87]   U. Sterr, diploma thesis,(Bonn, 1987), not published

[Ste92a]   U. Sterr, K. Sengstock, J.H. Müller, D. Bettermann, and W. Ertmer, Appl. Phys. B54, 341 (1992)

[Ste97]   U. Sterr, K Sengstock, W. Ertmer, F. Riehle, J. Helmke, in Atom Interferometry,ed. by P.R. Berman, Academic Press, 1997

[Ste92]   A.M. Steane, M. Chowdhury, and C.J. Foot, J. Opt. Soc. Am B9, 2142 (1992)

[Ste93]   U. Sterr, thesis, (Bonn, 1993), not published

[Sto94a]   P. Storey and C. Cohen-Tannoudji, J. Phys. II France 4, 1999 (1994)

[Sto94b]   H.T.C. Stoof, Phys. Rev. A49, 3824 (1994)

[Str94]   R. Strichirsch, thesis, (Bonn, 1994), not published

[Stw71]   W.C. Stwalley, J. Chem. Phys. 54, 4517 (1971)

[Tel90]   H.R. Telle, D. Meschede, and T.W. Hänsch, Opt. Lett. 15, 532 (1990)

[Tho87]   H.R. Thorsheim, J. Weiner, P.S. Julienne, Phys. Rev. Lett. 58,4317 (1987)

[Tow95]   C.G. Townsend, N.H. Edwards, C.J. Cooper, K.P. Zetie, and C.J. Foot, Phys. Rev. A52, 1423 (1995)

[Ung89]   P.J. Ungar, D.S. Weiss, E. Riis, and S. Chu, J. Opt. Soc. Am. B6, 2058 (1989)

[Vid77]   C.R. Vidal and H. Scheingraberg, J. Mol. Spec. 65, 46 (1977)

[Wal90]   T. Walker, D. Sesko, and C. Wienman, Phys. Rev. Lett. 64, 408 (1990)

[Wal94]   T. Walker and P. Feng, in Advances in Atomic, Molecular, and Optical Physics, ed. by B.Bederson and H. Walther, Vol 34, p.125,Academic Press, San Diego (1994)

[Wei 89]   D.S. Weiss, E. Riis, Y. Shevy, P.J. Ungar, S. Chu, J. Opt. Soc. Am. B6, 2072 (1989)

[Wei94a]   D.S. Weiss, B.C. Young, and S. Chu, Appl. Phys. B59, 217 (1994)

[Wei94b]   M. Weitz, B.C. Young, and S. Chu, Phys. Rev. A50, 2438 (1994)

[Wei95]   J. Weiner, in Advances in Atomic, Molecular, and Optical Physics, (B. Bederson and H. Walther eds.) Vol 35, p.45,Academic Press, San Diego (1995)

[Wei96]   M. Weitz, T. Heupel, and T.W. Hänsch, Phys. Rev. Lett. 77, 2356 (1996)

[You97]   B. Young, M. Kasevich, and S. Chu, in Atom Interferometry, ed. by P.R. Berman, Academic Press (1997)

[Zel93]   K. Zelgert, diploma thesis, (Bonn,1993), not published

[Zei95]   K. Zeiske, G Zinner, F. Riehle, and J. Helmcke, Appl. Phys. B60, 205 (1995)

Acknowledgment

I would like to take this opportunity to thank the people who helped me during my studies in Germany.

First I would like to thank my thesis advisor Prof. Dr. W. Ertmer for the many stimulating ideas and discussions and for the support during the final stage of this work. I would also like to thank Prof. Dr. K. Danzmann for his acceptance of being my second referee.

I am grateful to mention my colleagues Dipl. Phys. F. Ruschewitz and Dipl. Phys. H. Hinderthür for their cooperation to finish this work. I would like to thank Dipl. Phys. D. Scheller , R. Degner, A. Pautz and N. Schaffrath who have contributed to the experiments in numerous ways.

In my first year in this group I would like to thank Dr. D. Bettermann, Dr. V. Rieger and Dr. J.H. Müller who were very helpful and taught me a lot of the experimental techniques in this group. I would like to thank Dr. U. Sterr and Dr. R. Deutschmann for their helps to solve problems during my study here. Dr. M. Schiffer and Dipl. Phys. M. Rauner and other colleagues in this group have in one way or another helped me to solve many problems of my life in Germany. I am very appreciated for their kindness. I would also like to thank Dipl. Phys. G. Wokurka and W. Schikowski for the possibility to loan a power supply for the experiment.

I would like to thank Mr. Heidekrüger and all the colleagues in the mechanical department for their help to finish the necessary components for this experiment and the secretariat for the administrative help. I would also like to thank Mrs. Krämer, Dr. R. Gaul and Dr. G.Birkl for their kind concern of my work.

My special thanks goes to Dr. K. Sengstock who helped me a lot and encouraged me various time during my studies in this institute. I would also like to thank him and my good friend Dipl. Phys. M. Rauner for their careful reading of the manuscript.

I would like to acknowledge the financial support form DAAD during the first four years of my thesis and from my thesis advisor during the last four months .

I would like to thank my landlady Mrs. Dr. Stinner for her encouragement and that I felt in her home like at home. Although it is far away from home I got many supports and encouragement from my mother and my siblings. I thank them with all my heart.

Curriculum vitae

26.08.1965   born in Taoyuan, Taiwan, R.O.C.

Education

1971-1977 Fu-Gang elementary school, Taoyuan

1977-1980 Fu-Gang junior high school, Taoyuan

1980-1983 Chien-Kuo senior high school, Taipei

1983-1987 B.S. degree in physics, Tung-Hai university, Taichung

1987-1989 M.S. degree in physics, Tsing-Hua university, Hsinchu

         thesis: Measurement of Al Concentration and Depth Distribution in $Ga_{1-x}Al_xAs$

         by the Resonant Nuclear $^{27}Al(p,\alpha)$ Reaction

Experiences

7/89-5/91   Military service

8/91-5/93   Associate researcher at Industrial Technology Research Institute, department:

         Center for Measurement Standards, Hsinchu

Ph.D. education in Germany

6/93-9/93   DAAD fellow, Goethe-Institut, Freiburg

10/93-1/95   DAAD fellow, Institute of applied physics, Bonn university, Ph.D. student at the

         group of Prof. Dr. W. Ertmer

2/95-1/98   DAAD fellow, Institute of quantumoptics, Hannover university, Ph.D. student at

         the group of Prof. Dr. W. Ertmer